AD

AD-E400 509

CONTRACTOR REPORT ARSCD-CR-80017

RAPID ULTRASONIC INSPECTION OF ARTILLERY PROJECTILES

ROBERT E. LEE
LEN T. SPRAGINS
FRANK BARR
ROCKWELL INTERNATIONAL SCIENCE CENTER

JOSEPH H. MULHERIN
ARRADCOM

NOVEMBER 1980

US ARMY ARMAMENT RESEARCH AND DEVELOPMENT COMMAND
FIRE CONTROL AND SMALL CALIBER
WEAPON SYSTEMS LABORATORY
DOVER, NEW JERSEY

The views, opinions, and/or findings contained in this report are those of the author(s) and should not be construed as an official Department of the Army position, policy or decision, unless so designated by other documentation.

Destroy this report when no longer needed. Do not return it to the originator.

The citation in this report of the names of commercial firms or commercially available products or services does not constitute official endorsement or approval of such commercial firms, products, or services by the United States Government.

REPORT DOCUMENTATION PAGE

READ INSTRUCTIONS BEFORE COMPLETING FORM

1. REPORT NUMBER: Contractor Report ARSCD-CR-80017
2. GOVT ACCESSION NO.:
3. RECIPIENT'S CATALOG NUMBER:

4. TITLE (and Subtitle): RAPID ULTRASONIC INSPECTION OF ARTILLERY PROJECTILES

5. TYPE OF REPORT & PERIOD COVERED: Final Report 12/21/78 through 3/28/80

6. PERFORMING ORG. REPORT NUMBER: SC5186FR

7. AUTHOR(s): Robert E. Lee, Len T. Spragins, and Frank Barr- Rockwell International Science Center
Joseph H. Mulherin, Project Engineer - ARRADCOM

8. CONTRACT OR GRANT NUMBER(s): DAAK10-78-C-0409

9. PERFORMING ORGANIZATION NAME AND ADDRESS: Rockwell International Science Center
1049 Camino Dos Rios
Thousand Oaks, California 91360

10. PROGRAM ELEMENT, PROJECT, TASK AREA & WORK UNIT NUMBERS: MMT5786654

11. CONTROLLING OFFICE NAME AND ADDRESS: ARRADCOM, TSD
STINFO (DRDAR-TSS)
Dover, NJ 07801

12. REPORT DATE: November 1980

13. NUMBER OF PAGES: 172

14. MONITORING AGENCY NAME & ADDRESS (if different from Controlling Office): ARRADCOM, FC&SCWSL
Materials and Manufacturing Technology Division (DRDAR-SCM-P)
Dover, NJ 07801

15. SECURITY CLASS. (of this report): UNCLASSIFIED

15a. DECLASSIFICATION/DOWNGRADING SCHEDULE:

16. DISTRIBUTION STATEMENT (of this Report)

Approved for public release; distribution unlimited.

17. DISTRIBUTION STATEMENT (of the abstract entered in Block 20, if different from Report)

18. SUPPLEMENTARY NOTES

This project was accomplished as part of the US Army Manufacturing Technology Program. The primary objective of this program is to develop on a timely basis, manufacturing processes, techniques, and equipment for use in production of Army materiel.

19. KEY WORDS (Continue on reverse side if necessary and identify by block number)

Nondestructive testing
Electromagnetic acoustic transducers
Automatic transducers
Automatic inspection system
Ultrasonics
Artillery projectiles
Projectile inspection
Microprocessor control and data analysis
M&MT-ammunition

20. ABSTRACT (Continue on reverse side if necessary and identify by block number)

This report describes the development of an automated ultrasonic inspection system for nondestructive evaluation of M549 (RAP) artillery projectiles using electromagnetic acoustic transducers (EMATs). The technical effort culminated in the successful demonstration of the inspection system to an engineering team from ARRADCOM and the subsequent delivery of the unit to the ARRADCOM facility in Dover, New Jersey.

DD FORM 1 JAN 73 1473 EDITION OF 1 NOV 65 IS OBSOLETE

20. ABSTRACT (continued)
During the course of this equipment development program, several unique subsystems were produced in order to construct the tatal EMAT NDE system. State-of-the-art implementations of high power solid state transmitters (above 1 KW) and low noise receivers were achieved as well as a unique high flux electromagnet design to magnetize the projectile. In addition, a microprocessor unit that was capable of sequencing the inspection operation, gathering, analyzing and displaying the results in tabular form on a hardcopy output was also developed. The EMAT unit readily detected flaw standards of 0.020 inch deep by 1.00 inch long placed both in the inside and outside of a test projectile's ogive and bourrelet region.

The results achieved during this program clearly establish the following points: (1) EMAT technology is a viable method for projectile inspection, (2) the EMAT system can inspect projectile at production line rates (over one per minute), and (3) a high degree of automation can be incorporated into EMAT systems. The unit demonstrated good sensitivities to flaws in the standard projectile and correctly distinguished between flawed and unflawed projectiles in simulated tests. The equipment functioned effectively and without error in both its automatic and manual mode of operation. EMATs thus appear to be viable candidates for the next generation of automatic projectile inspection equipment.

TABLE OF CONTENTS

LIST OF FIGURES

LIST OF FIGURES (continued)

LIST OF FIGURES (continued)

LIST OF FIGURES (continued)

LIST OF FIGURES (continued)

I. SUMMARY

This report describes the development of an automated ultrasonic inspection system for the nondestructive evaluation of M549 (RAP) artillery projectiles using electromagnetic acoustic transducers (EMATs). The technical effort culminated in the successful demonstration of the automated system to a team of ARRADCOM engineers and the delivery of the unit to the ARRADCOM facility in Dover, NJ.

The results achieved during this program clearly established several points: a) it validated EMAT technology as being applicable to the inspection of artillery projectiles, b) it demonstrated that high inspection speed (meeting the targeted goals specified in the contract) are feasible using EMATs and c) it showed that a high degree of automation could be implemented with an EMAT system to reduce the amount of "human" judgement or interpretation in product evaluation. It is conjectured that the EMAT system fabricated possesses flaw detection sensitivities comparable to that of "optimally coupled" conventional ultrasonic systems (used in the same mode). This is because the flaw signal-to-noise ratio was determined by acoustic clutter signals arising from projectile surface imperfections and was not set by signal level or dynamic range limitation of the EMATs or associated electronics.

The key elements of the EMAT projectile inspection system including the EMAT coils, electromagnet and pole pieces, analog and digital electronics were designed, fabricated and tested at the Albuquerque Development Laboratory, a department of the Rockwell International Science Center. The large

part handling apparatus and hydraulic system was designed and constructed under subcontract by K. J. Law Engineers to Rockwell specifications. The system demonstrated the ability to operate, through its inspection sequence, either manually (step-by-step) or by using a single command, to perform a complete inspection operation and light a red (flaw) or green (no flaw) indicator describing the quality of the projectile under inspection. The system was also capable of mapping the amplitude and location of ultrasonic reflections (flaws) and printing these on a hard copy output. EMAT system calibration was accomplished by setting threshold levels determined by inspecting an ultrasonic test "standard" that had specific flaws cut into its interior and exterior surfaces. The standard was made in accordance with specifications established by ARRADCOM and certified by an independent government agency.

The system performed satisfactorily in all major respects. Once calibrated, the EMAT unit could reject (detect), map and/or display flaws in a) the standard projectile (having multiple flaws), or b) a projectile having only one flaw and would pass, as unflawed, a previously conventionally inspected projectile that had no imperfections. All critical flaws were found in the ogive and bourrelet sidewall of the longitudinal standard projectile by the system. The majority of the flaws in the base were found by a hand operated EMAT that was <u>not</u> part of the final delivered system but which could be retrofitted at a future date. There were a few flaws located in the curved interior region of the standards base that were undetectable using EMATs. The problem was not due to the EMAT transducer or method but due to the ultrasonic energy being dispersed by the curved surface. It is believed that any ultra-

sonic detection method might be plagued by this inspection geometry. Further work is needed on the EMAT technique to overcome this type of inspection geometry.

The conclusion achieved by this effort is that EMATs are applicable to the ultrasonic inspection of artillery projectiles for flaws located anywhere within their sidewall volume. EMATs have the major advantages of being rapid, noncontacting, and amenable to reproducible calibration and automation.

II. OBJECTIVE OF PROGRAM

This program consisted of two phases which were to be performed in series. The purpose of the first phase was to investigate the EMAT ultrasonic signal launching phenomenon in M549 (RAP) projectiles produced by Norris Industries. This phase was necessary because previous experiments showed a substantial decrease in signal transduction efficiency when EMATs launched acoustic waves in a tangentially magnetized projectile. This phase was successful in identifying that (1) a surface condition (about 0.007 inches deep) caused the poor coupling, and (2) that by going to vertical magnetization of the projectile surface, large acoustic signal transduction could be reestablished. The final report on this phase was issued August 1979. (Report SC5186.24FR).

The second phase of this program was to construct and evaluate the necessary hardware and computer software to demonstrate an automated EMAT

ultrasonic inspection station for M549 (RAP) projectiles. The detailed objectives are as follows:

(1) Determine the actual levels of defect detectability in various locations in the warhead and demonstrate that noncontact EMAT ultrasonic transducers can function effectively.

(2) Demonstrate the quality of inspection equal to or superior to that of conventional ultrasonic inspection, and

(3) Demonstrate that the system can perform ultrasonic inspection of the 155 mm M549 (RAP) warheads at actual production rates (suggested to be about 14,000 per month or 44.6 sec per shell based on one 8 hr work shift per day).

A final subsidiary objective was to develop an inspection apparatus that can be reproducibly calibrated so that automated measurement techniques can be employed to make the inspection process (Accept/Reject Decision) as repeatable as possible.

The EMAT ultrasonic system that was developed addressed all of the above objectives and was predominantly successful in validating both the speed and quality of inspection concept with a prototype system. It is anticipated that ARRADCOM will gain further insight into EMAT projectile inspection by using this equipment.

In order to acquaint the reader more fully with the merits of EMAT technology, Appendix A gives a comparison of EMAT to conventional ultrasonic

inspection techniques as applied to the inspection of artillery projectiles. Objectives to be accomplished were set forth by the Product Assurance Directorate (PAD) at ARRADCOM.

III. FUNDAMENTALS OF EMAT OPERATION

This section gives a brief review of the fundamentals of EMAT operation. The purpose is to highlight the important operating characteristics of this type of transducer and give insight into the performance tradeoff which occur under different operating conditions.

Figure 1 illustrates the principle of EMAT coupling to an electrical conductor for ultrasonic noncontact transduction. Acoustic waves are launched in a magnetized metal part when a wire carrying a time varying electrical current is brought into close proximity to the metal's surface. The eddy currents which are induced interact with the magnetic B-field and give rise to body forces which cause the acoustic generation. The converse effect also occurs where sound waves in the metal cut lines of flux thus producing eddy currents which are sensed by induction by the wire. If the magnetic field is normal to the surface, the dynamic body forces are predominantly due to Lorentz $(\vec{J} \times \vec{B})$ interactions of the free electrons with the lattice. The force vectors lie parallel to the part surface and readily generate vertically polarized shear waves (as will be shown later). The normal magnetic field bias, effective in all conductors, yields a linear relationship between bias field B and ultrasonic wave amplitude and generally requires quite large

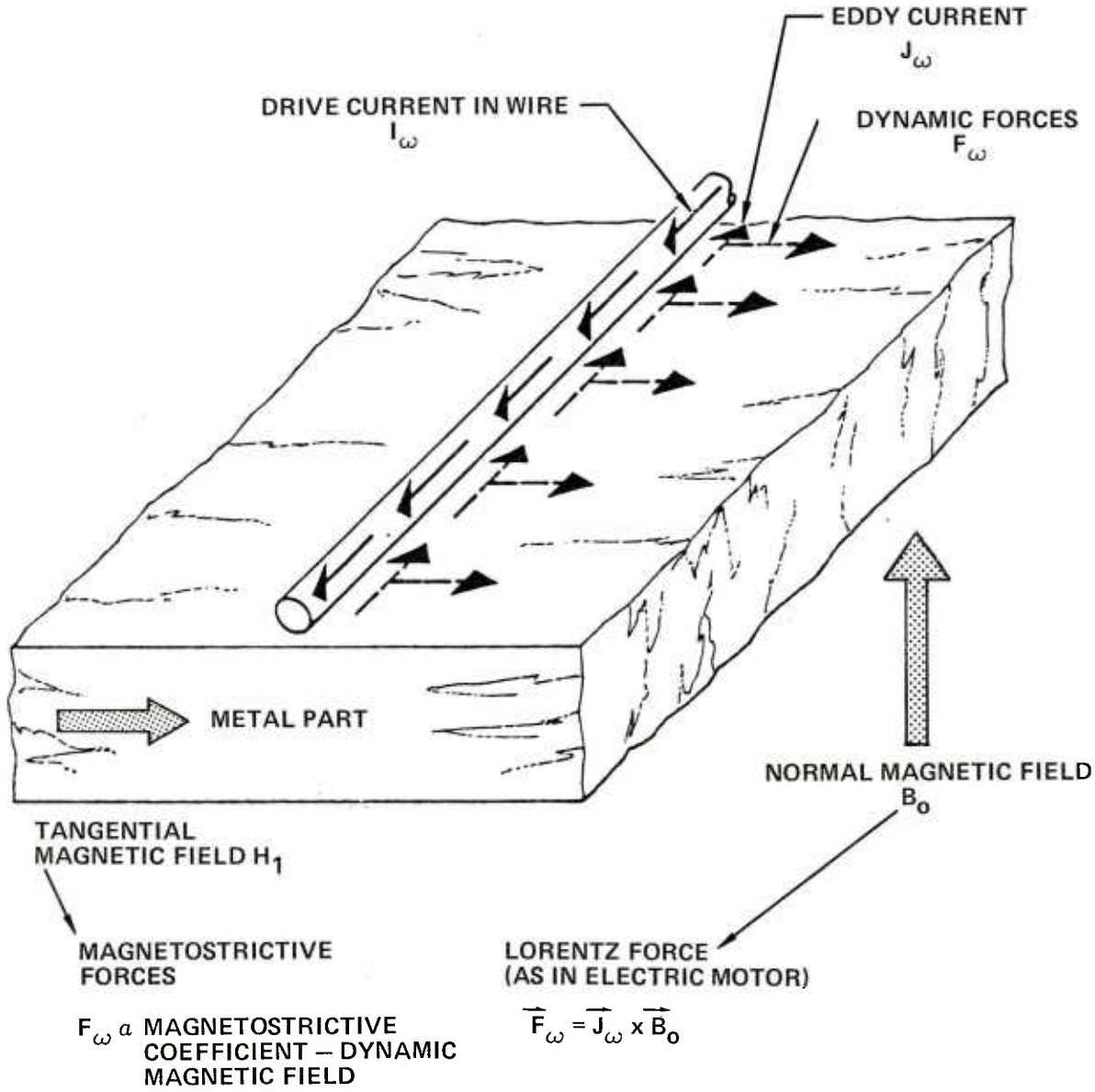

Fig. 1 Distribution of currents and forces on the lattice of a metal part contributing to generation of ultrasonic signals under normal field bias.

B-fields to achieve substantial coupling. A tangential magnetization scheme is possible in ferromagnetic materials. This mechanism is based on the coupling that occurs between the induced dynamic magnetic fields which accompany the eddy currents and the non-zero magnetostrictive effect (see Reference 1) present in some polycrystalline metals. This type of excitation is nonlinear in B, having a peak coupling at quite low fields (see Fig. 2 for a schematic of the interaction). It is tempting to base most inspection processes on this low B-field magnetostrictive coupling since it reduces the size, weight and cost of the magnet required. However, it was determined in Phase A (Ref. 2) of this work that a) not all projectiles inspected possessed strong magnetostrictive coupling, and b) the magnetostrictive coupling could be easily destroyed by heat treating the projectile (in a simulated processing step). Thus it was concluded that the magnetostrictive type interaction was too tenuous and that the normal magnetic field bias Lorentz force would be employed because of its superior reproducible coupling.

Figure 3 illustrates the isotropic radiation pattern for a line force along the y axis at the origin of an isotropic half space of a material having elastic properties like steel and compares the shear waves that are generated when the force vectors are in the x (Fx), y(Fy), and z(Fz) directions. The physical situation produced by the normal bias of an EMAT produces forces along the surface (x) direction so that the far-field acoustic radiation pattern expected for the projectile inspection would be the curve labeled Fx-SV waves. One observes that the maximum generation efficiency occurs at about 30° to either side of the normal (i.e., the transducer is bidirec-

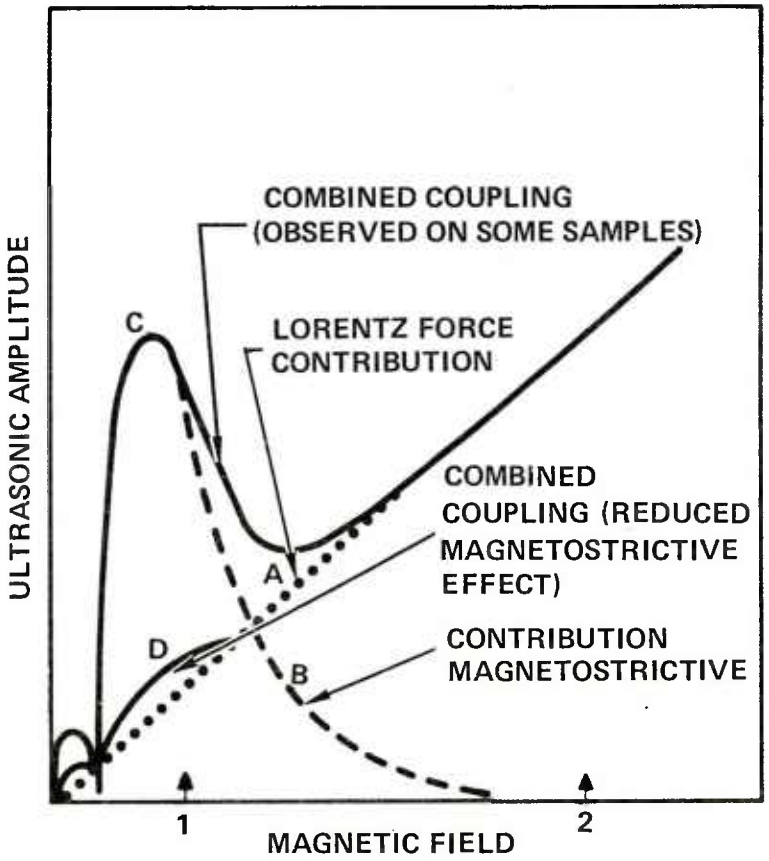

Fig. 2 Types of ultrasonic generation observed for (A) Lorentz type coupling, (B) magnetostatic type coupling, (C) combined type coupling observed on some samples, (D) combined coupling with diminished magnetostrictive contribution. Problems arise if the projectile is biased at a magnetic field level (1) and the unit does not possess the full magnetostatic contribution. Biasing to magnetic field level of (2) insures large ultrasonic amplitude generation independent of material properties.

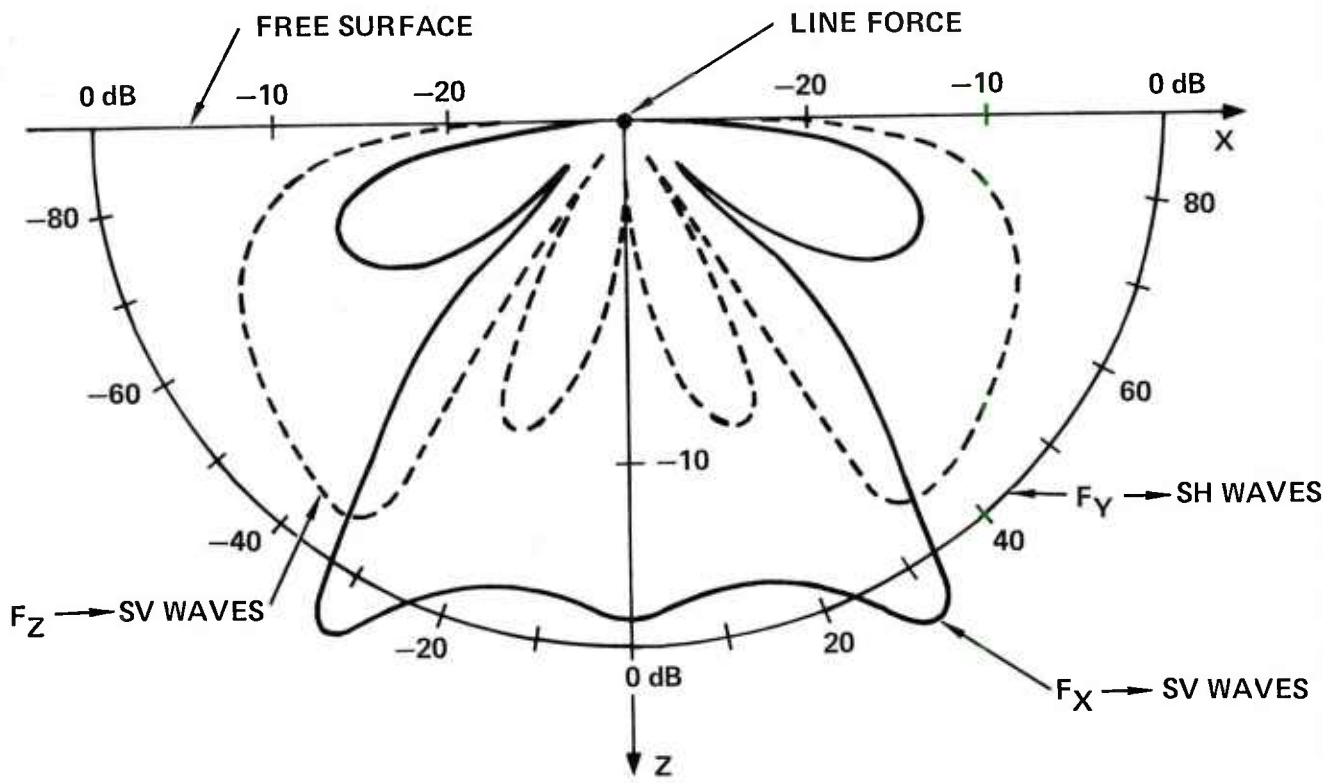

Fig. 3 Green's function, radiation pattern, for shear waves, SV and SH, in a isotropic steel material for a line excitation force. F_X, SV waves are generated by the EMAT shown in Fig. 1.

tional), that there is substantial coupling in the z direction and that the other side lobes of the single wire acoustic antenna are suppressed about 20dB. These facts are important to discriminate against spurious reflections when applied to flaw inspection geometries. More detail on this result is given in Reference 3. Since EMAT coupling is generally quite weak, a common method of improving the generation efficiency is to construct a multiple turn transducer (meander coil) and to drive current through the coil with a sinusoidal modulation. Figure 4 shows the typical form of the meander coil whose period is D which is driven by a current at frequency $f = \omega/2\pi$. This transducer is capable of generating surface (Rayleigh) waves (Fig. 4(a)) if the drive frequency f is chosen to be:

$$f = \frac{V_R}{D} \tag{1}$$

where V_R is the surface wave velocity. In this case D is equal to the surface wavelength. This mode is particularly well suited to find surface imperfections because the energy is guided by the surface and extends to a depth of about Λ_R beneath the surface.

The same transducer (Fig. 4b) is capable of generating angle shear waves when driven at a higher frequency. When $f > \frac{V_s}{D}$, where V_s is the material shear wave velocity, shear waves will be produced at an angle:

$$\phi = \sin^{-1}\left(\frac{V_s}{fD}\right) \tag{2}$$

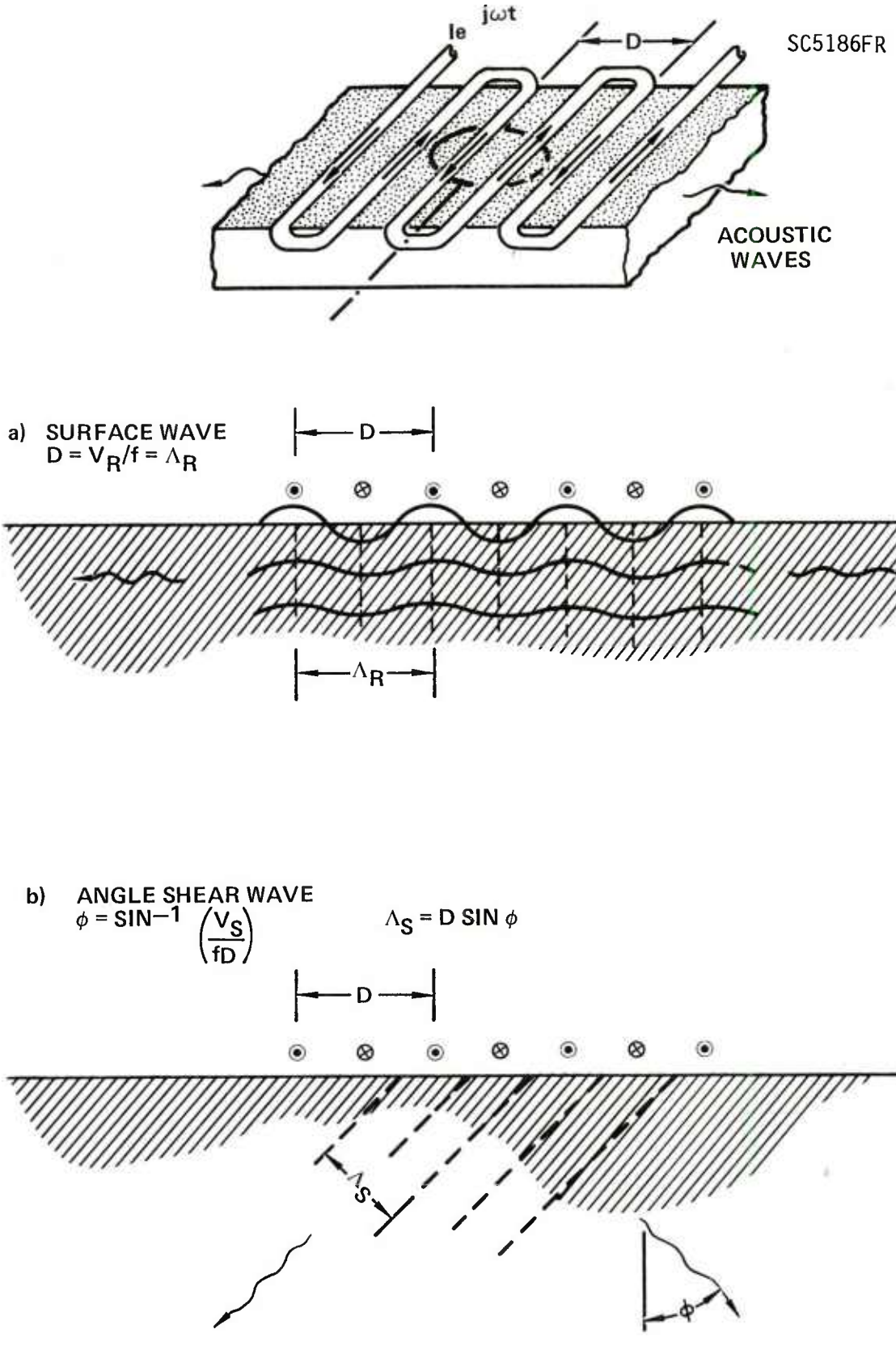

Fig. 4 Use of meander coil (top) to generate surface waves (a) and angle shear waves (b) in a material.

with respect to the surface normal and the shear wavelength Λ_s will be D sin ϕ. The transducer is symmetric so it emits and detects waves in both directions.

By creating an acoustic antenna, the antenna array factor must be multiplied by the Green's function in order to establish the overall radiation pattern to be expected from the EMAT into the solid. The most usual case is to drive the EMAT so that it excites waves at about 30° to the normal (to correspond to the maximum of the Green's function) and use a large number of periods which forms a narrow beam of sound in the metal part being investigated. The direction of SV-beam emission is variable by frequency tuning, however 30° is by far the most efficient angle and thus it was chosen for all EMAT implementations. EMAT transducers having 3, 4, 6 and 7 periods (D) were built and tested. The 4 period and 7 period coils were chosen for final implementation because they yielded good overall coupling and produced a sufficiently narrow acoustic beam to discriminate against spurious reflections.

IV. SUMMARY OF WORK COMPLETED IN PHASE A (Reference 2)

It is useful to summarize the results of Phase A of this effort to rationalize the direction efforts took in Phase B, the fabrication of the prototype inspection system. When attempts were made to inspect M549 155mm (RAP) projectiles manufactured by Norris Ind. by magnetizing the shell and inspecting it using EMATs located in the tangential field region, it was found the EMAT excitation was vastly diminished (about 27dB) compared to similar

projectiles made by other manufacturers (e.g., Feinchbaugh). The hypothesis was made that the decreased efficiency was due to a surface phenomena. This was verified, as shown in Fig. 5, by measuring the acoustic signal amplitude as various depths of material were removed from the surface. The "as-received" shells had very poor transduction efficiency. However, the loss in coupling could be nearly compensated (to within 1.5dB) by milling off 0.007 inch of material from the projectiles surface.

A second conclusion was drawn from the data in Fig. 6 which shows that heat treatment (830°C for 4 hr) reduces the signal amplitude ~ 28dB, the difference between Fig. 6(b) and (c). It was conjectured that heat treating the projectile alters the surface (to a depth of about .007 inch) which was attributed to the decrease in magnetostatic EMAT coupling.

The method chosen to overcome this material and process temperature dependent coupling was to place the EMAT coils in a normal bias field. Here Lorentz type forces, independent of magnetic surface conditions, are employed and the EMAT signals can be steadily increased by employing increasingly large magnetic fields. This is illustrated in Fig. 7 for a projectile before and after heat treatment. The data, circles and triangles, fall along the expected parabolic curve (ultrasonic signal proportional to B^2) because two EMAT transductions have taken place (input to output).

This result guided our efforts during the total of phase B to locate the EMAT coil between the projectile wall and the magnet pole piece where the B-field is normal to the shell surface. Difficulties experienced in achieving an ideal uniform normal B-field will be described in the next section.

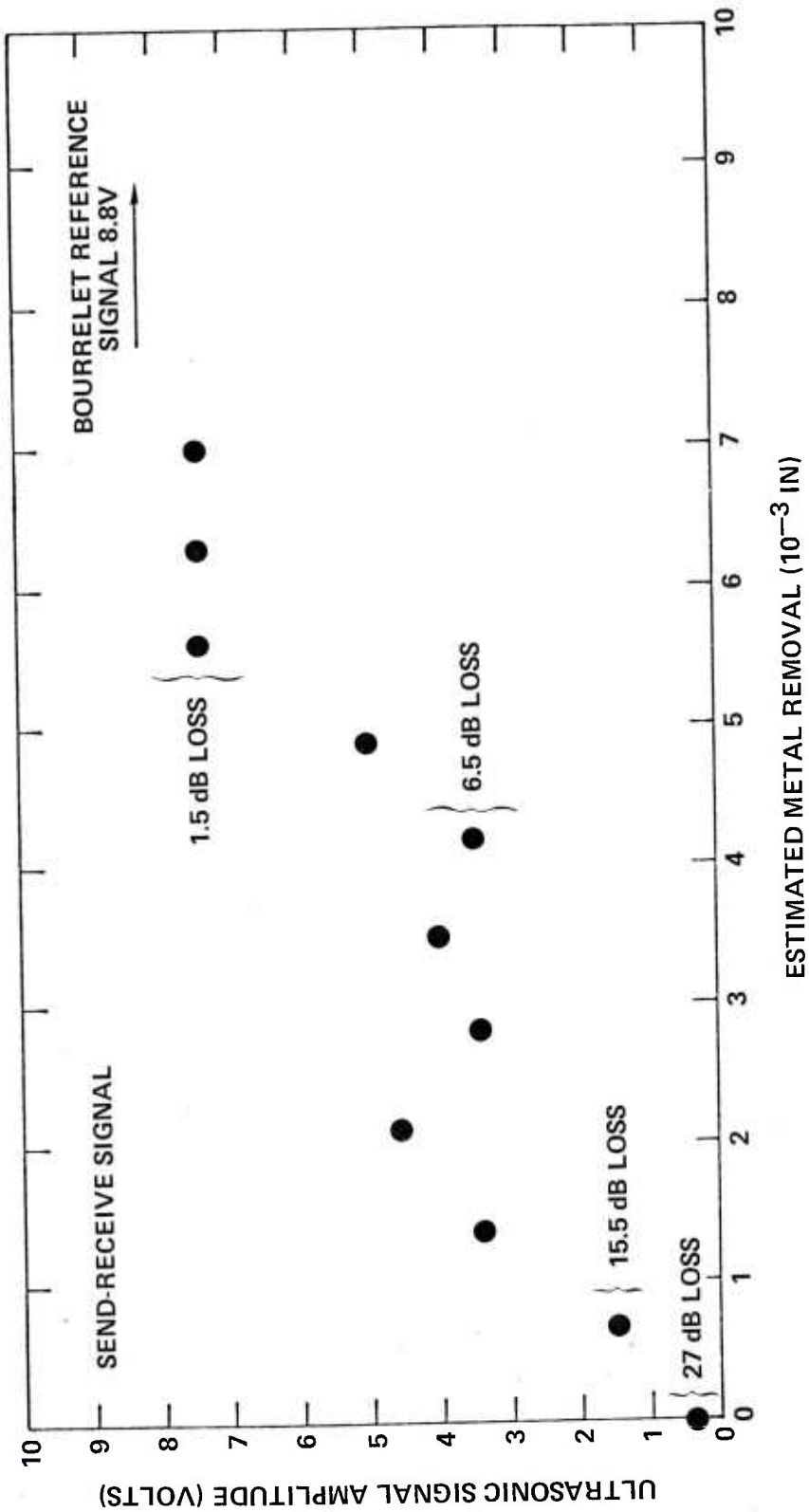

Fig. 5 EMAT transducer efficiency as a function of metal removed from the ogive of an M549 artillery projectile.

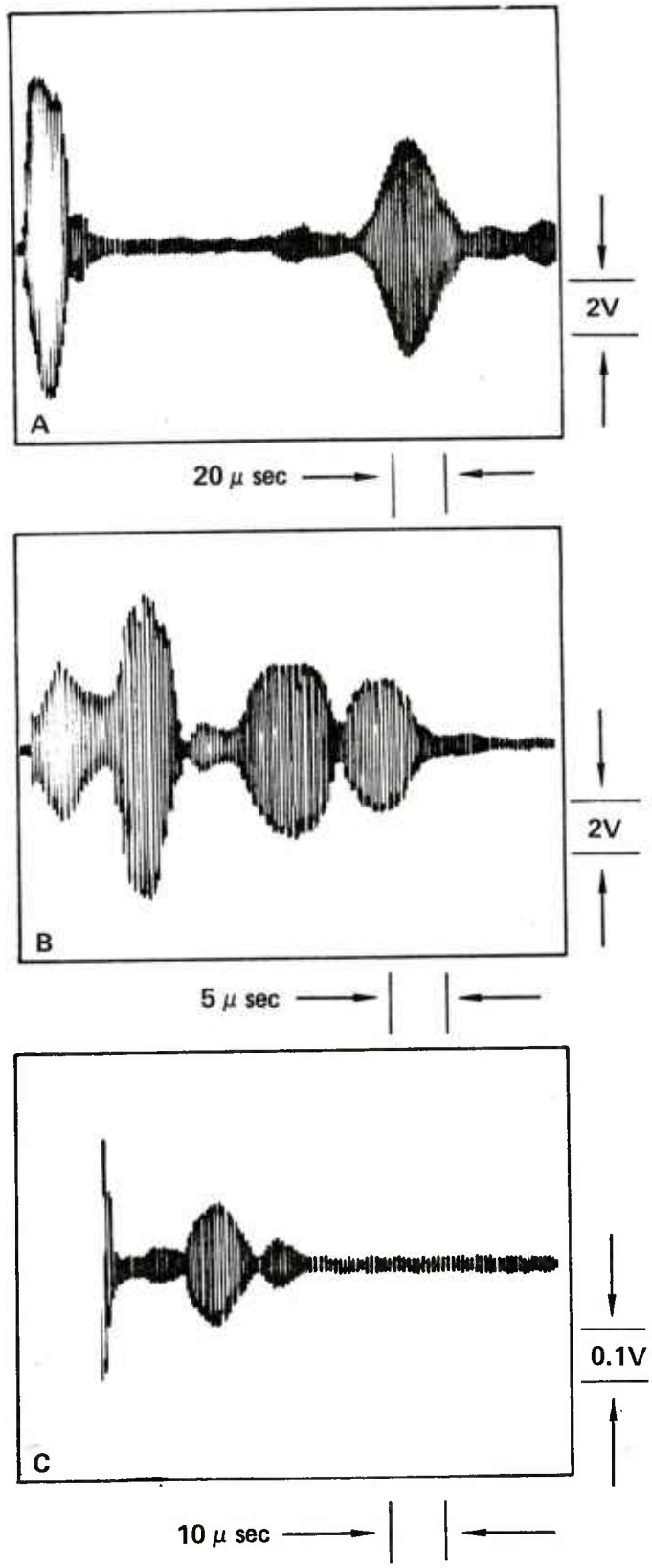

Fig. 6 EMAT ultrasonic signal efficiency for different stages of fabrication of an M549 (RAP) artillery projectile.
(a) Prior to nosing, (b) prior to heat treatment and (c) after heat treatment.

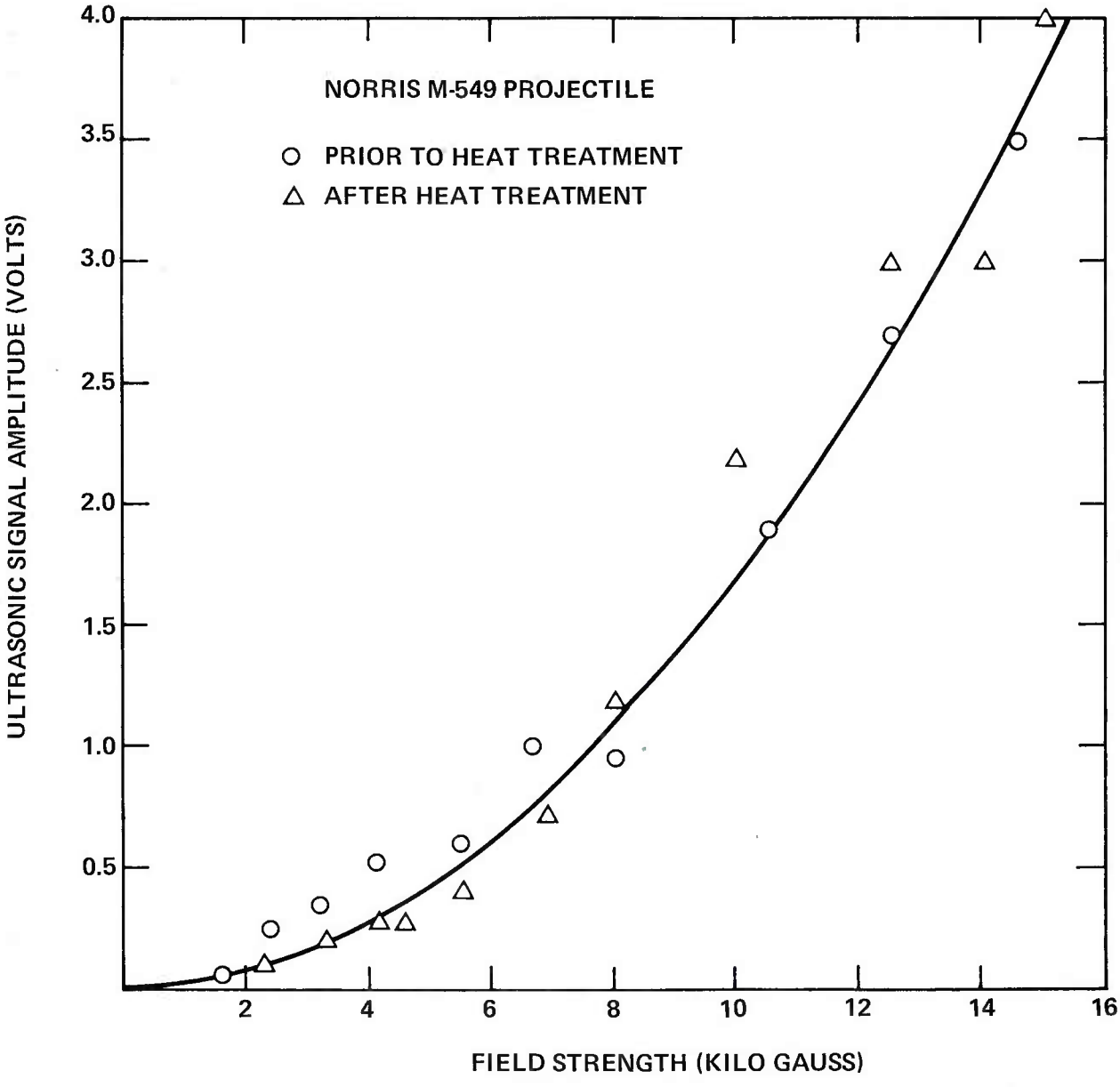

Fig. 7 EMAT ultrasonic signal amplitude of an M549 (RAP) artillery projectile in a normal magnetic field before and after heat treatment.

V. MAGNETIC FIELD ANALYSIS

It was found that one of the key elements in the successful EMAT inspection of cylindrically shaped objects, such as projectiles, is to achieve a uniform normal magnetic flux through the EMAT coil into the part. Figure 8 depicts a cross-section of a projectile being magnetized by a tapered pole piece and the relative locations of EMATs for normal and tangential field operation. Energizing the electromagnet coils cause a large magnet to be formed with the projectile in the gap. The flux flows from the north (N) pole piece through the projectile and emerges into the south (S) pole. If tangential field operation was possible then two transducers could be employed (in a pitch catch mode), however, since only one EMAT transducer can be accommodated beneath either pole-piece face, the same coil must be used as both the transmitter and receiver in a pulse echo mode.

Figure 9(a) illustrates one particular problem associated with the magnetization of the projectile, that of normal B-field uniformity and homogeneity. For an EMAT operated in the tangential field, region, the field is by definition uniform because it has entered the metal and is confined to the walls due to the high permeability (μ) of the part. However, underneath the pole-piece the flux is just entering the projectile and is then free to diverge as it enters into the cylinder. Figure 9(b) illustrates the fact that magnetic flux lines obey a relationship given by:

$$\frac{\tan \theta_1}{\tan \theta_2} = \frac{\mu \text{ air}}{\mu \text{ steel}} \quad , \tag{3}$$

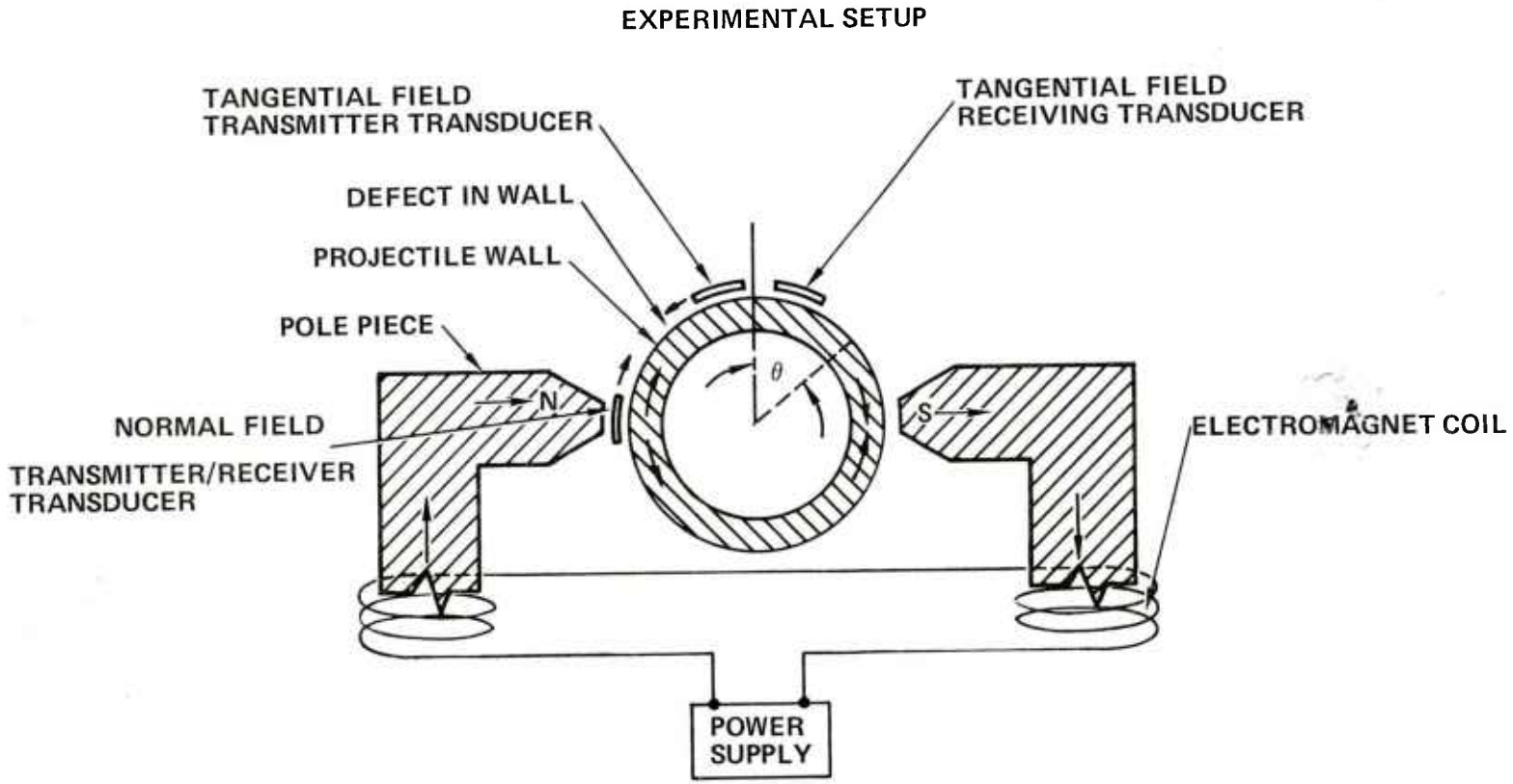

Fig. 8 Magnet configuration for EMAT inspection of the M549 projectile.

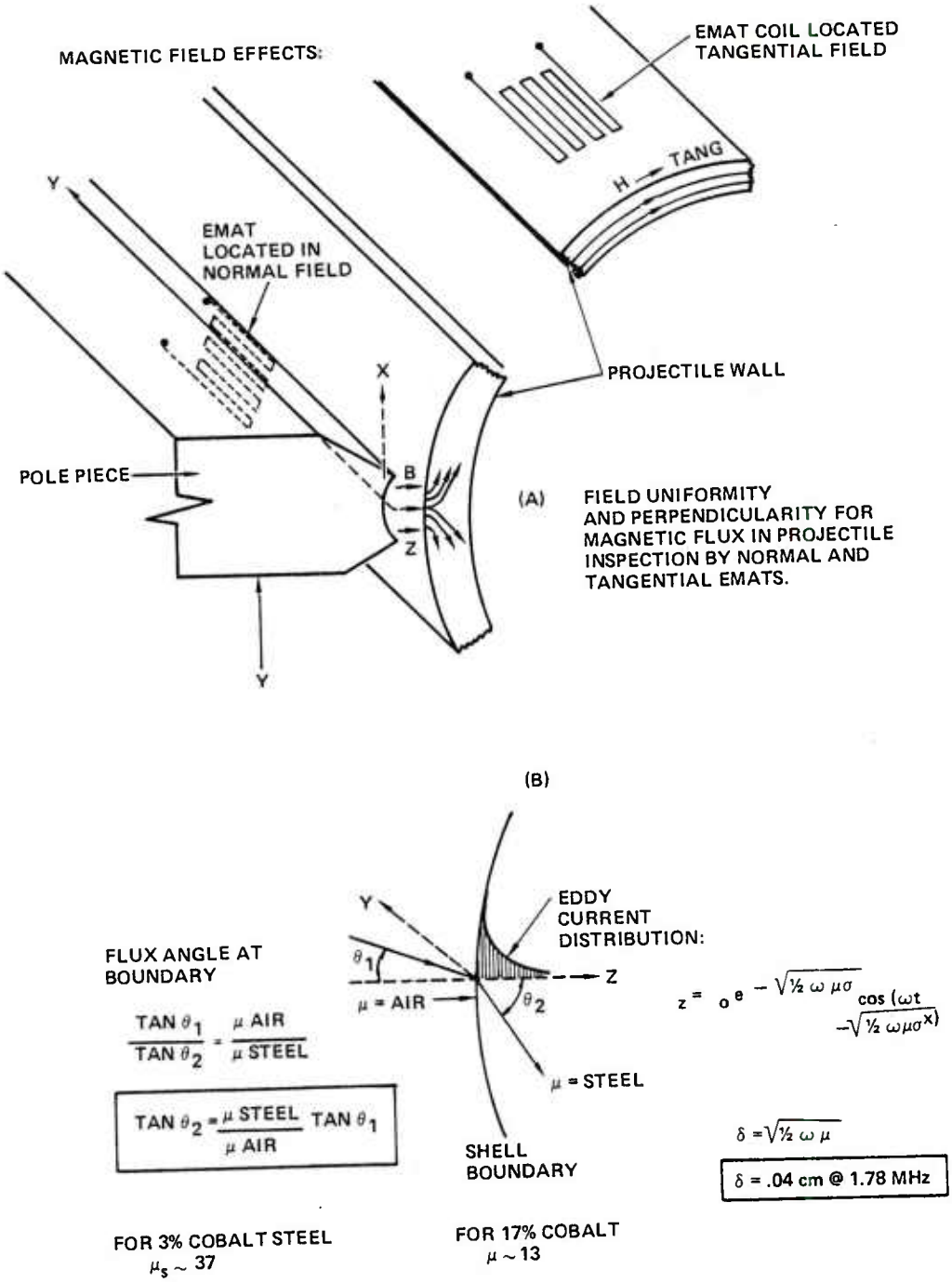

Fig. 9 Magnetic field effects.

or

$$\tan \theta_2(\text{steel}) = \frac{\mu \text{ steel}}{\mu \text{ air}} \tan \theta_1(\text{air}), \qquad (4)$$

a kind of Snell's Law for magnetic flux. Thus, any deviation from normal flux at the air-projectile interface (given by θ_1) is magnified by the ratio of μ steel to μ air, generally a large quantity. For example, Cobalt steel has a μ of about 37 at moderately high bias fields. The depth over which the flux normality is critical is approximately given by δ, the depth of eddy current penetration, because within that region the acoustic forces are generated. The eddy current distribution with depth is given by

$$iz = io\, e^{-\sqrt{1/2\ \omega\mu 6}\ z}$$

$$\text{or} \quad \delta = \sqrt{1/2\ \omega\mu 6}$$

where ω is the angular frequency and 6 is the material conductivity. For steel, at $\omega = 11.18 \times 10^6$ or f = 1.78 MHz, the eddy current depth is 0.04 cm. Hence, only the projectile surface is important in flux uniformity. An added complication is that μ is a function of magnetic B-field and, for the HF-1 projectile, behaves as shown in Fig. 10. These results were obtained by making a special permeability measuring electromagnet, associated power supply, digital voltmeter and digital flux meter. The value of μr, the relative permeability, is above 40 at B equal to 20K gauss. This means the

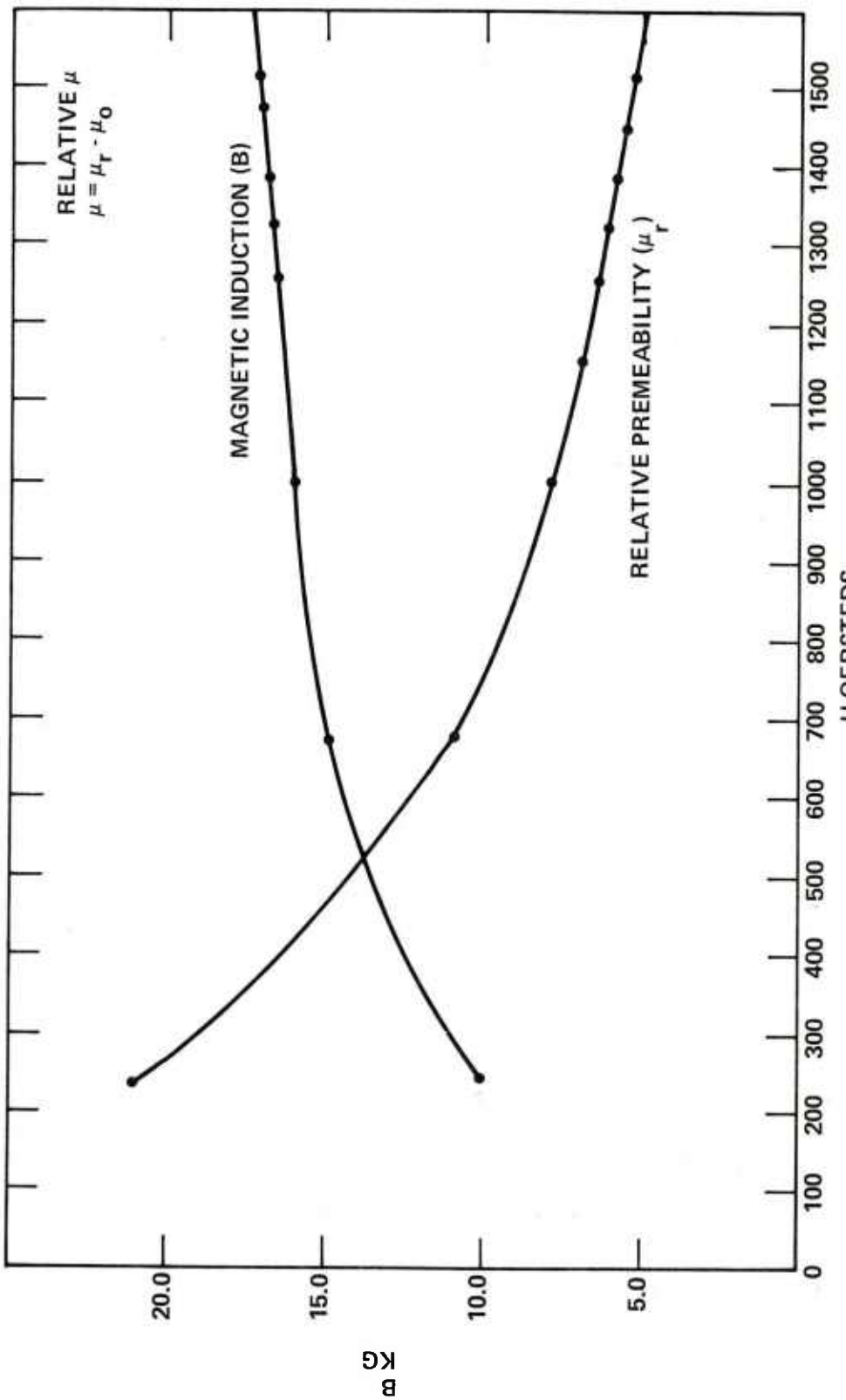

Fig. 10 Measurement of the relative permeability (μ_r) of the projectile steel HF-1 as a function of magnetic induction.

shell should act to confine the field lines but will seriously bend the flux that enters the projectile at off normal directions.

The basic design principle chosen for the pole pieces were to shape them as accurately as possible to conform to the projectile profile along all axis in order to a) maximize the field in the material, b) make it as homogeneous as possible along the length, and c) force the lines of flux to enter the projectile at normal incidence to the surface. Two parallel approaches were undertaken to try to achieve a practical magnetic circuit design as fast as possible. The first method employed the hand calculation of the flux paths reluctance of the magnetic circuit and an approximate B-field analysis. This was coupled to empirical measurements made on longitudinal sections of projectiles in order to refine and improve the approximate formulas. The second method, accomplished in parallel, was to computer model the pole-piece projectile region and do interactive Poissons solutions to the B-field space problem. A complete summary of this approach is given in Appendix B and only results will be quoted here.

Figure 11 shows the semi-empirical approach. The projectile is sectioned into 3 approximately equal pieces (the ogive, transition region and bourrelet region). A small electromagnet was made that accommodated about 6.5" long cylindrical sections of projectile. The electromagnet main section was constructed so that various "nose pieces" (see Fig. 11(a)) could be attached to measure the effect of changing pole piece dimensions. The nose piece could be interchanged by unscrewing the hold down lock screw and substituting a different noise section. Approximate field analysis was used to

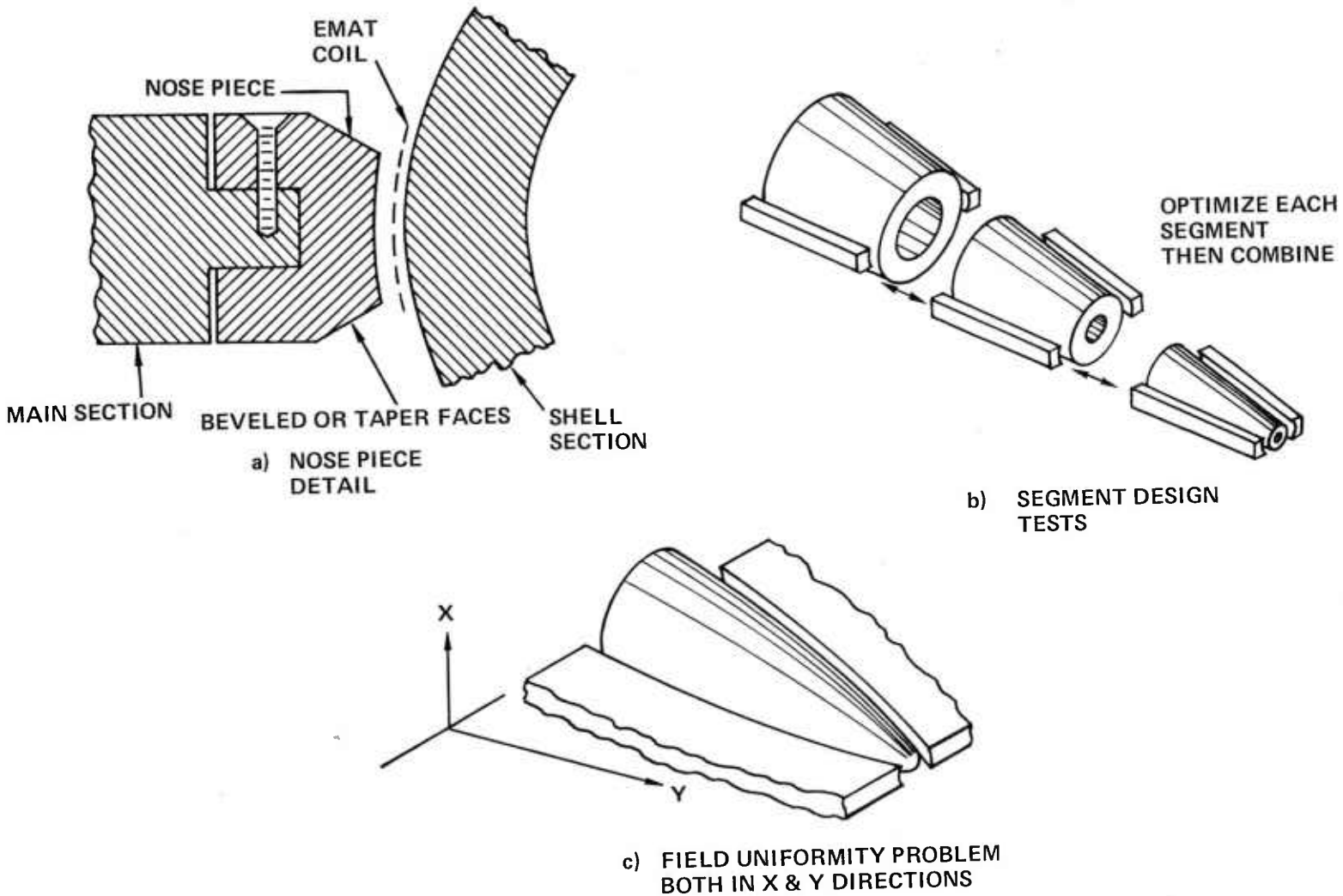

Fig. 11 Magnet design: to empirically design magnet pole pieces to yield maximum uniform normal flux into the projectile. Projectile is sectioned into 3 parts about 6-1/2"long. A series of differently shaped nose pieces are attached to the test electromagnet and field uniformity and EMAT generation efficiency tests are made. The 3 pole pieces are then used as a guide to design a final complete polepiece for the entire projectile.

guide the designs of the magnetic focusing structure. The critical nose piece parameters were: 1) the separation between projectile and pole piece face, 2) the length of the pole piece in the circumferential direction, 3) the shape-or curvature-of the pole piece face and 4) the taper angle of the focusing piece. Figure 12 illustrates a simple section through the pole-piece and projectile. Leakage flux around the shell causes premature saturation and limits the maximum B field attainable. Thus the dimension d, the separation, and W, the width of pole face should be chosen so that d/W is as small as is practical from other physical considerations. The separation d obviously can not be shrunk to zero because the EMAT coil assembly must occupy this space.

Figure 13 shows the shape of the magnetic B-field strength expected for various electromagnet coil currents at two separations (gap = d). These curves are governed by the equation:

$$B_{Gap} \simeq \frac{1}{A} \left\{ \frac{NI}{R_{Gap} + R_{shell(\mu)}} - \phi \text{ Leakage} \right\} \qquad (3)$$

By reducing d/w the leakage flux $\phi_{Leakage}$ is reduced and also the gap reluctance R_{gap} is reduced compared to R_{shell} (which is constant except for its dependence on μ).

In fact, the total magnetic circuit of the yoke, leakage, pole piece, gap and shell have been modeled to assure that the electromagnet assembly is adequate to supply sufficient flux to achieve over 20K gauss in the gap

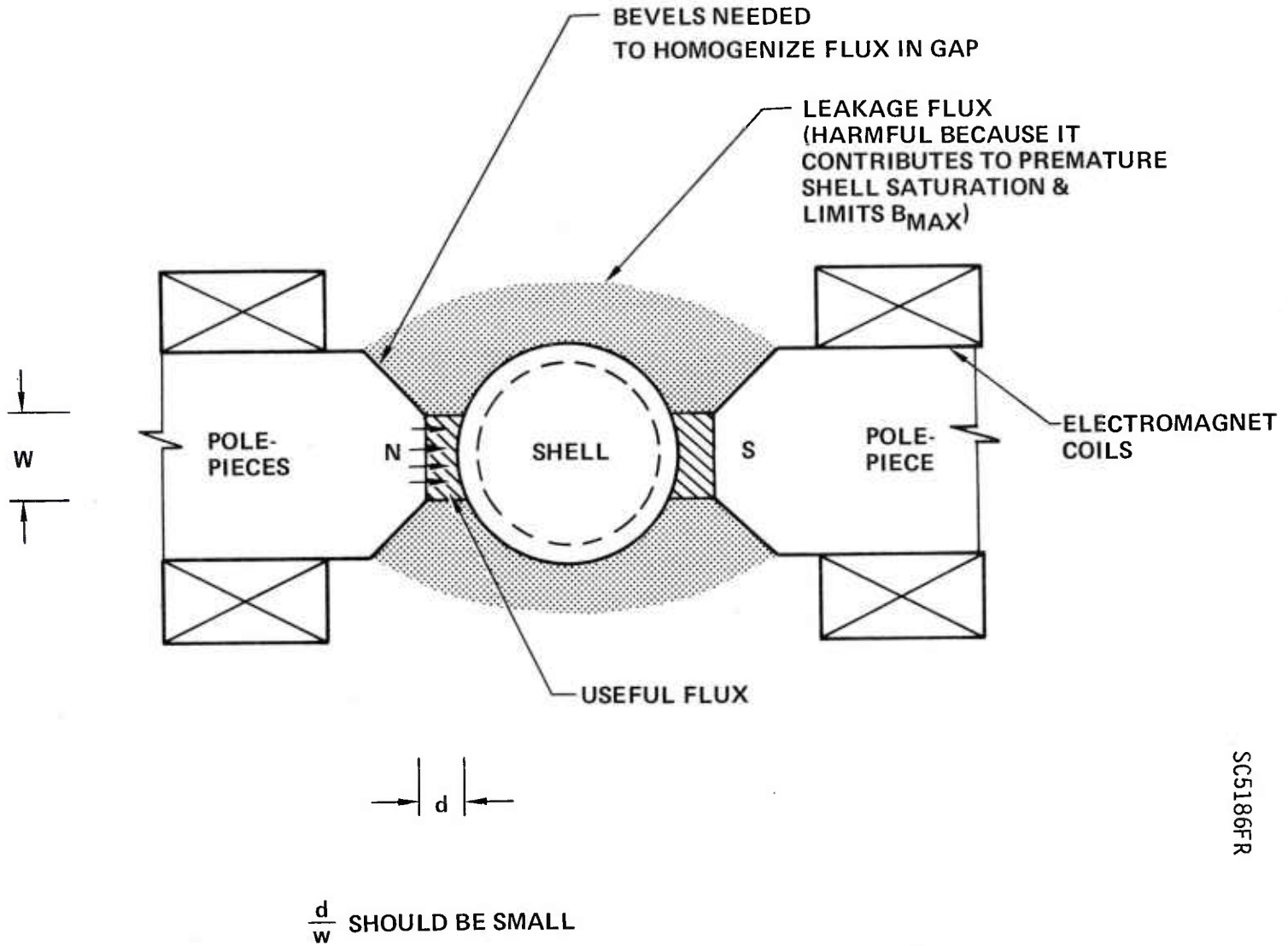

Fig. 12 Dimensional considerations for electromagnet structure design. Goal is to force as much flux as possible at normal incidence into the projectile beneath the pole pieces.

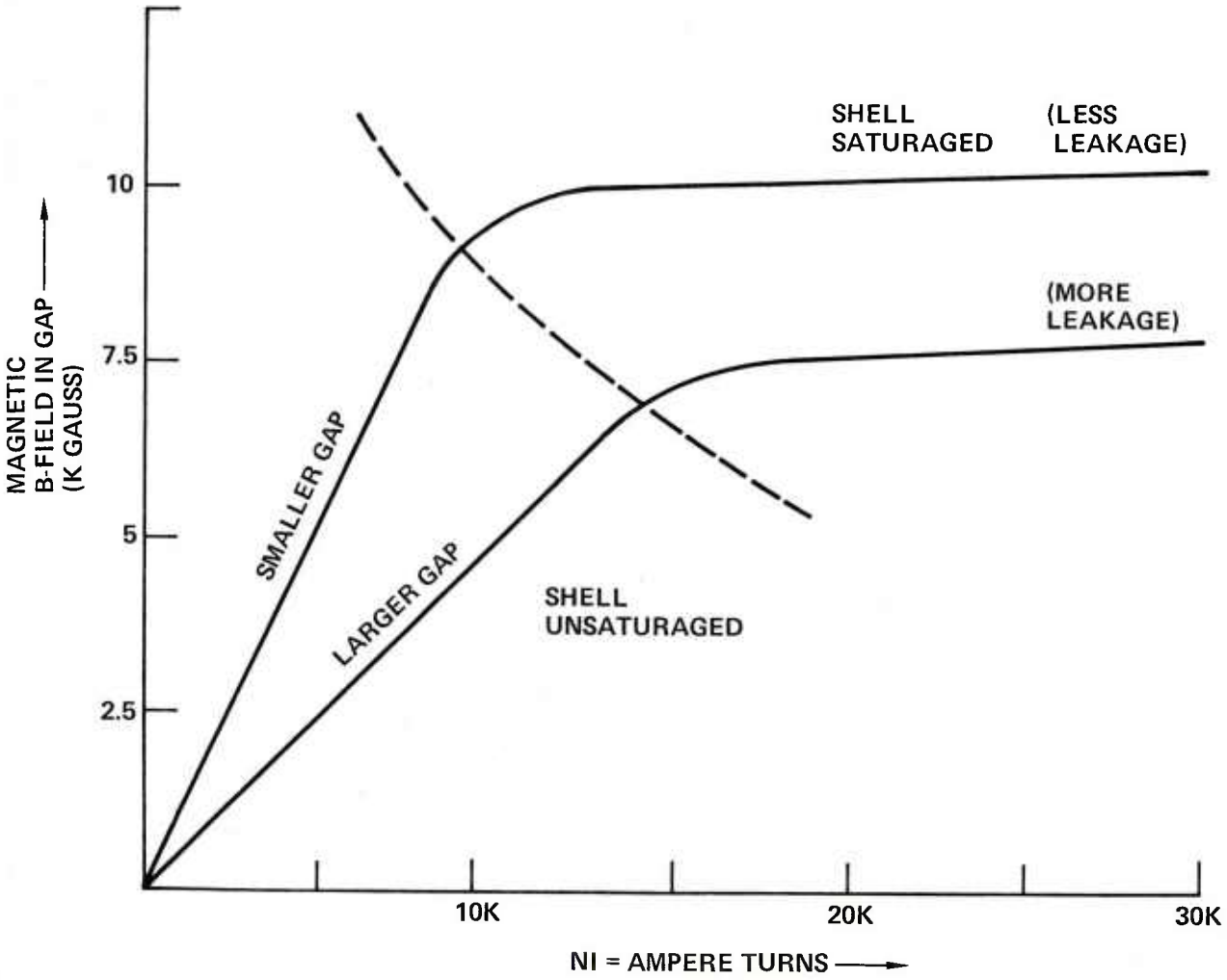

Fig. 13 Calculated magnetic field behavior as a function of gap separation d.

region. Figure 14 illustrates the simple model used. Results of this calculation were used to determine the length and cross sectional area of the yoke, pole pieces and number of ampere-turns required in the electromagnet to achieve the desired field levels. Ohms law for magnetics can be written as:

$$\phi = \frac{NI}{\Sigma Ri} \tag{4}$$

where ϕ is the flux, NI is the ampere turns or magnetomotive force applied and Ri are the reluctances shown in Fig. 14. Reluctance for material is defined as

$$Ri = \frac{\ell i}{\mu Ai} \tag{5}$$

where ℓi is the length of magnetic path, μ the permeability of the material and Ai the cross-sectional area of the path. In the gap

$$\phi_{gap} \cong B \cdot A_{gap} \tag{6}$$

so that

$$B_{gap} = \frac{1}{A_{gap}} \left\{ \frac{NI}{R_G + R_s + R_p + R_y} - \phi_{Leakage} \right\}$$

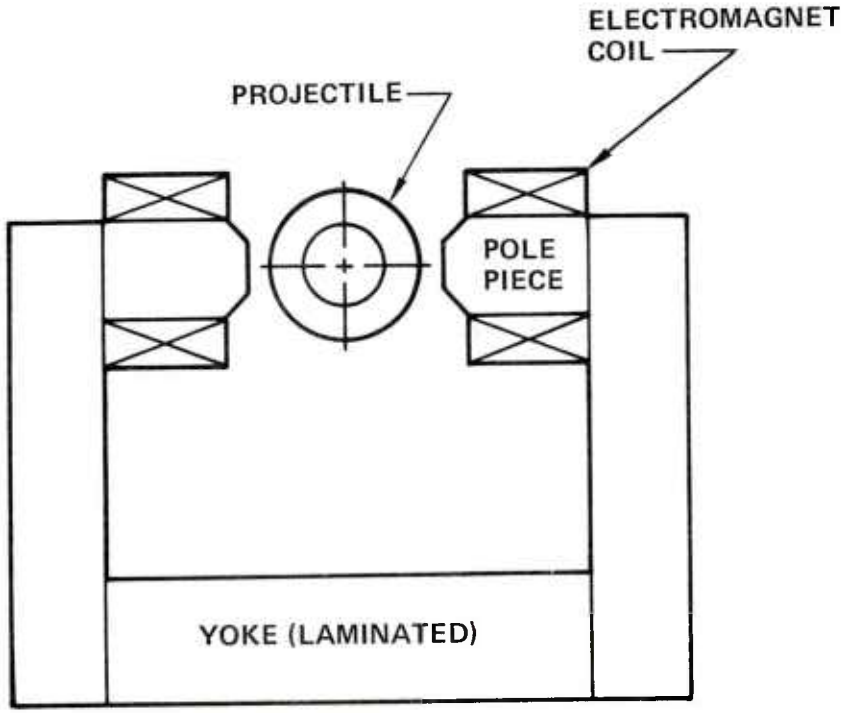

ϵ = MAGNETOMOTIVE FORCE

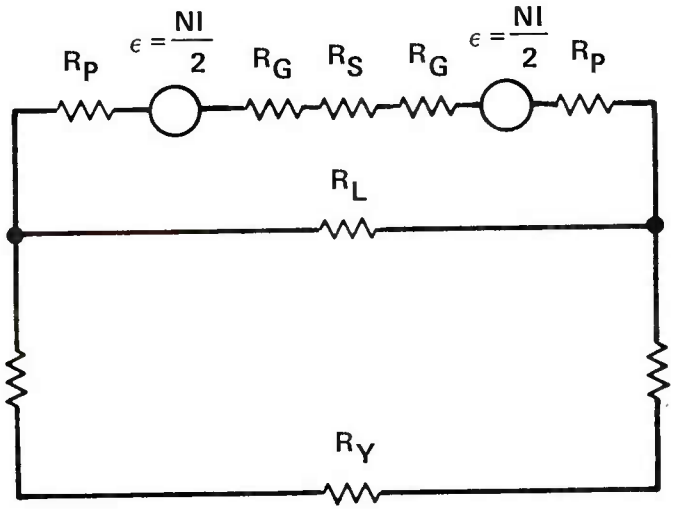

R_G	GAP RELUCTANCE
R_S	RELUCTANCE OF SHELL
R_P	POLE PIECE RELUCTANCE
R_L	LEAKAGE INDUCTANCE (CORE)
R_Y	RELUCTANCE OF CORE & YOKE

SC5186FR

Fig. 14 Electromagnet equivalent circuit model use for final design of yoke, pole pieces and coils.

this reduces to the result of Eq. (3) assuming proper magnet design which reduces R_p & R_y much below R_g and R_s. B_{gap} can be made large by increasing NI to saturation, reducing ϕ leakage and decreasing d which reduces R_g. The lateral width w of the pole piece face effects the reluctance of the gap and thus should be reduced to increase the gap field. Figure 15 shows the B-field intensity measured on a section of projectile for two different width pole pieces (1/2" and 3/4" widths) at a constant gap of 1/8". Substantial width reductions below 1/2" are not practical since the EMAT coil must fully lie beneath the pole face to achieve a uniform B-field. The 1/2" pole face produces about 15% more B-field at saturation compared to the 3/4" face.

The effect on B-field intensity of gap separation d, between the pole piece and projectile are illustrated in Fig. 16. Here for a 1/2" wide pole face, three gaps d = 1/8", 3/32", and 1/16" were used and the corresponding B-fields measured. The narrowest gap of 1/16" yielded fields of over 20 KG at saturation compared to about 16 KG for 1/8". Since the pole pieces are rigidly fixed in any electromagnet design and the cylindrical projectile must be moved laterally into and out of the gap, the pole pieces were tilted at 27° with respect to the horizontal axis to accommodate the vertical projectile motion. A series of measurements showed that the 27° tilt did not substantially add to the leakage flux and this modification was used in the final projectile inspection configuration.

In the final implementation, a gap of 3/32" was chosen as a compromise spacing which yielded sufficiently strong B-field but large enough to accommodate the EMAT coil and any projectile dimensional nonuniformities.

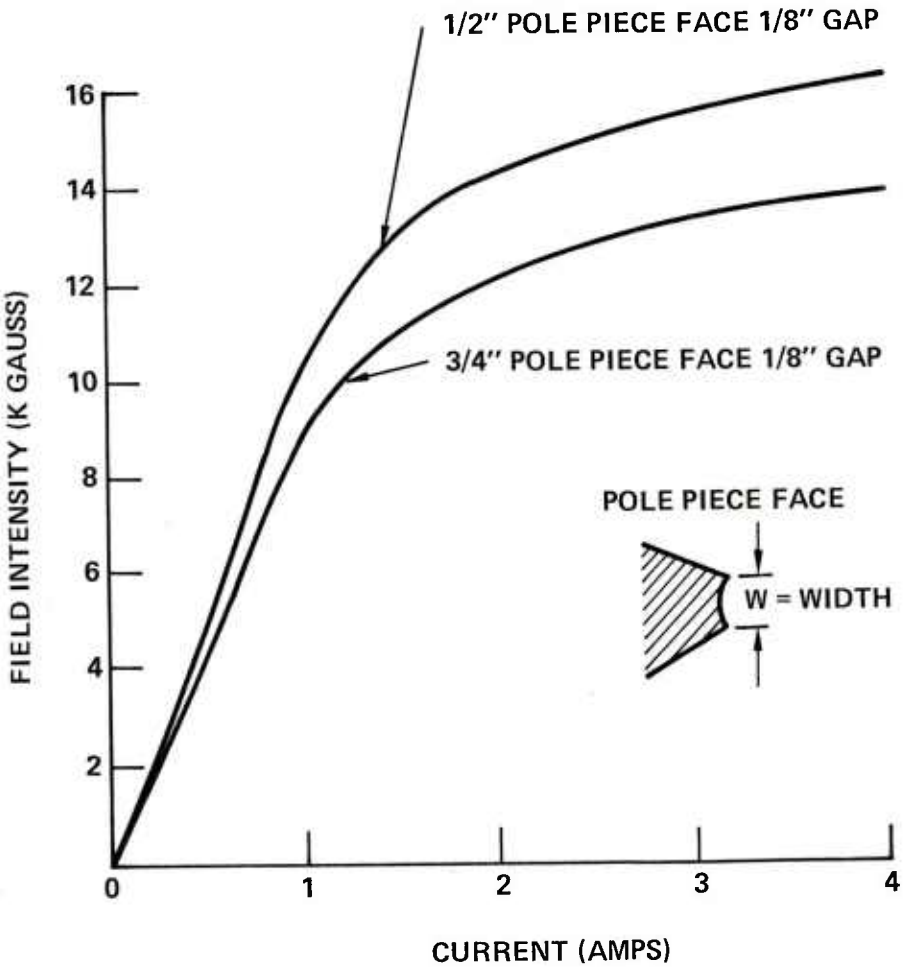

Fig. 15 Field intensity vs electromagnet current for 1/2" and 3/4" pole pieces widths W.

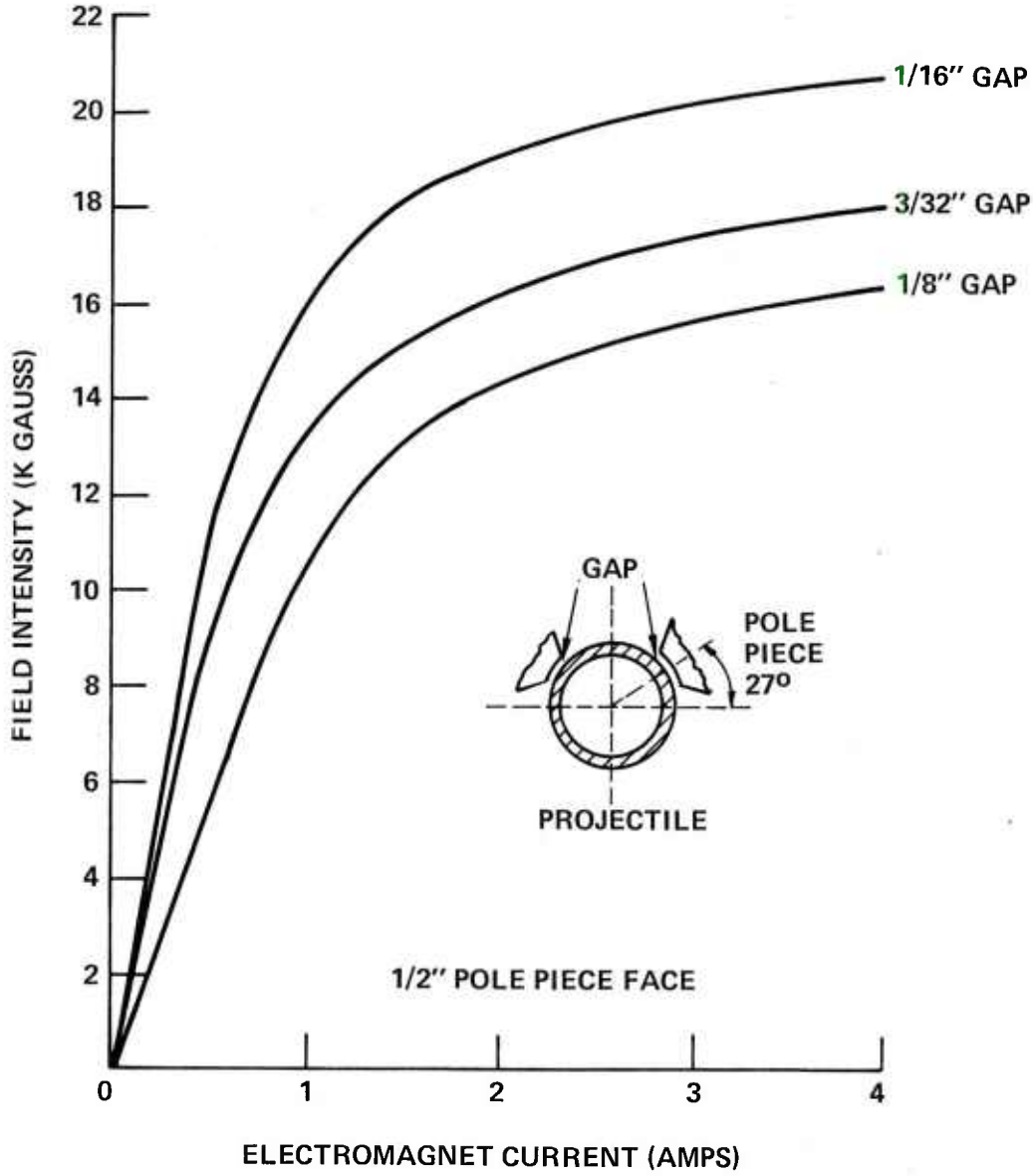

Fig. 16 Effect of pole piece gap width on magnetic field intensity. Pole pieces tilted at 27° from horizontal to accommodate projectile curvature and to allow the projectile to be moved into the magnetic field.

The effect of the shape of the pole piece face was investigated by measuring the B-field uniformity for a flat pole piece compared to a curved pole face (curvature chosen to match the projectile curvature and keep the gap d constant). The measure B-field, shown in Fig. 17, is substantially more uniform for the curved pole face and this type of curvature was used in the final design.

The width w of the pole piece face not only effects the magnetic field strength but also its uniformity. Figure 18 shows that a 1/2" face produces a more uniform and higher intensity magnetic field over its smaller area compared to a 3/4" wide pole piece driven to the same current level.

We also investigated the dynamic influence when the projectile was spun at a high rate near the pole piece face. There was some concern that flux pile-up would occur at the trailing edge of the pole piece. Figure 19 shows the results of spinning the projectile at 180 rpm (4-1/2 times faster than used during actual projectile inspection). Some flux accumulation (about 10%) is observed at the left edge of the gap, however the EMAT transduction efficiency was found to vary less than 5%. Thus projectile motion has minimal effect and EMAT inspection can be readily accomplished on rapidly moving objects (projectiles).

These empirical/quasi analytical results were adequate to lead us through the majority of the magnetic field design process. Still minor adjustments were tedious and time consuming by this approach. By the time the final pole-piece design was to be implemented, the computer program described

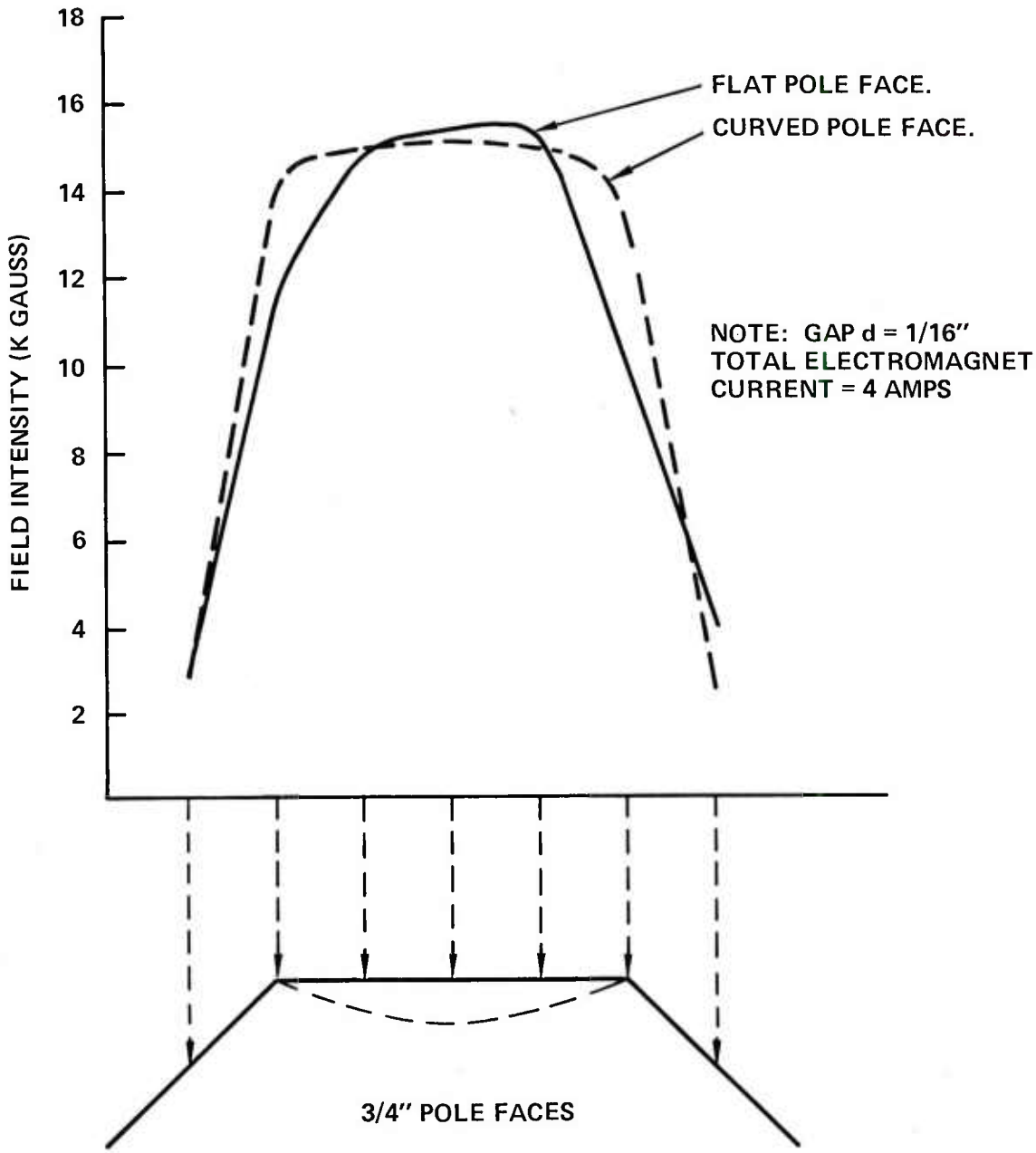

Fig. 17 Effect of pole piece shape on normal magnetic flux uniformity. Curved pole face yields more uniform flux at the projectile surface.

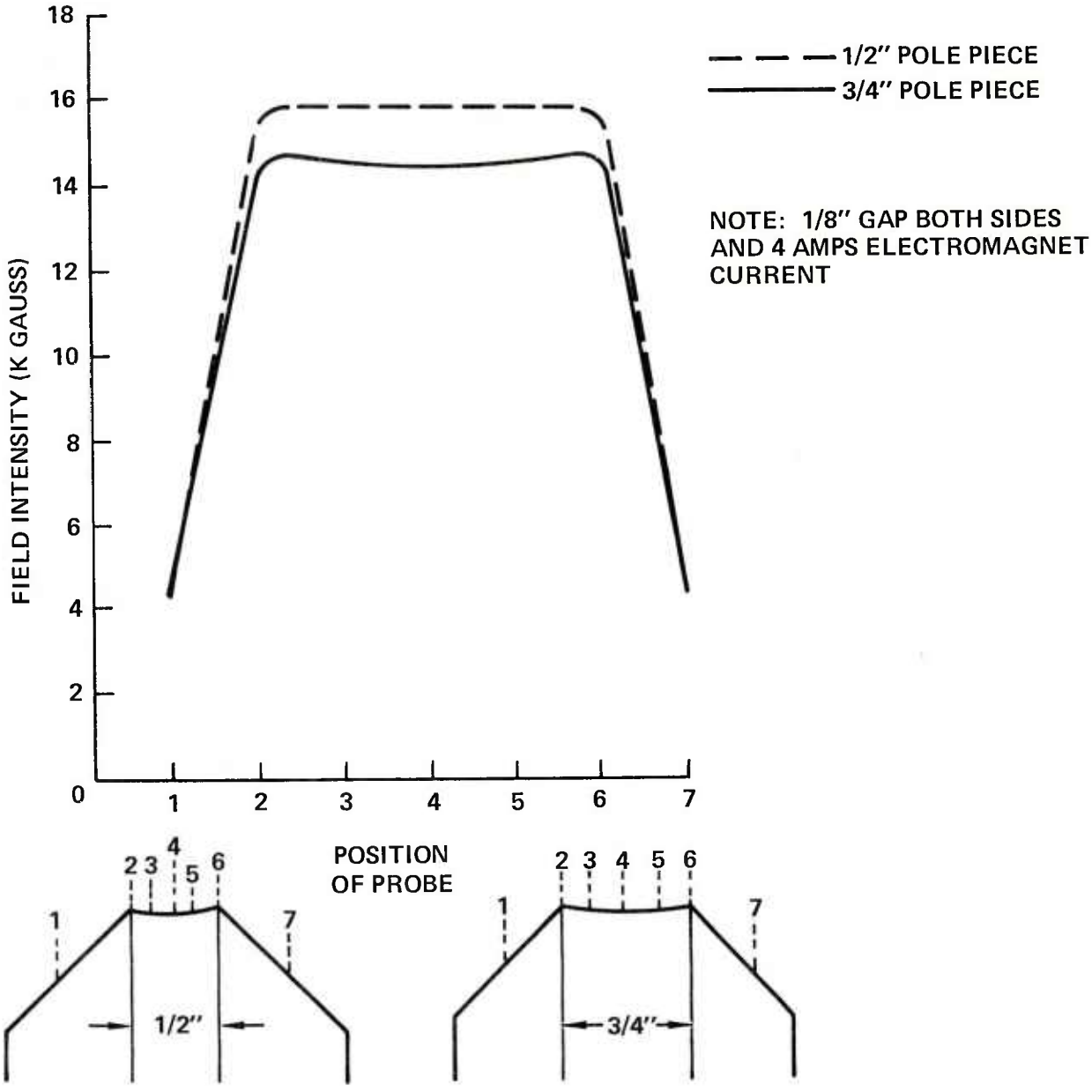

Fig. 18 Effect of pole piece face width on magnetic field uniformity and intensity.

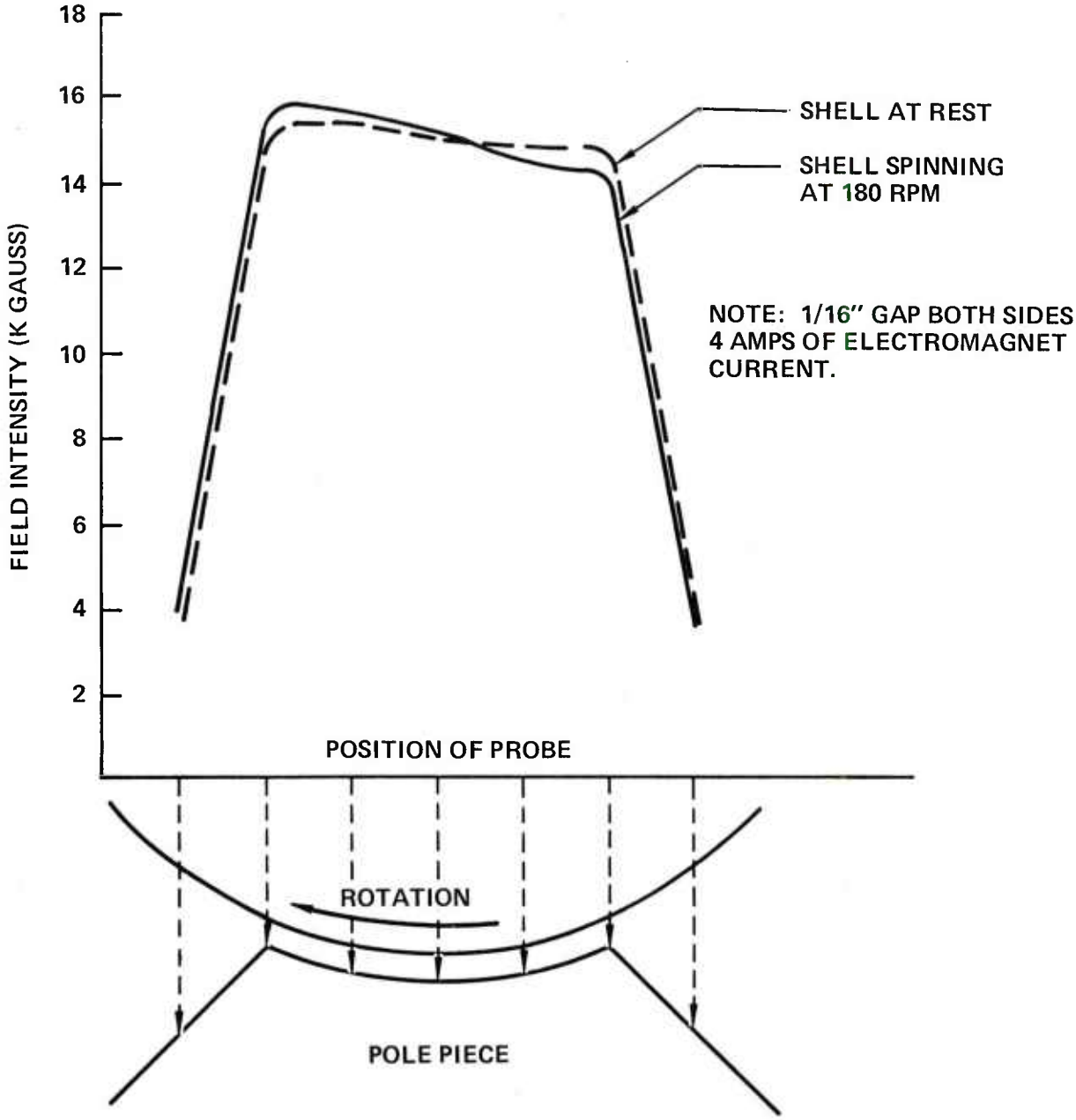

Fig. 19 Effect of shell rotation on magnetic field intensity and uniformity measured in the test magnet apparatus.

in Appendix B had been sufficiently developed for routine use. Several test cases were run using different geometries, different spacings and different tapers on the pole-pieces. A representative plot of the lines of constant magnetic potential ψ which surround the magnetized projectile and pole piece section are illustrated in Fig. 20. The potential ψ obeys Laplace's equation, with zero magnetic sources, in the region outside the metal ($\nabla^2\psi = 0$). The B-field is everywhere perpendicular to these equipotential lines. The other quadrants, to complete the field map, can be determined by symmetry. This overall view of the projectile and pole pieces was used to establish the magnetic boundary conditions and codes were established which allowed expansion of the critical gap region. In all cases shown in Fig. 21(a), (b) and (c), the pole piece are 3/4" wide, have 45° angle levels on its edge and are curved to follow the radius of the projectile. The twelve contours plotted show substantial differences between the 1/4" gap of Fig. 21(a), the 1/8" gap of Fig. 21(b) and the 1/16" gap of Fig. 21(c). Even more precise analysis was possible when the letter indicators were removed and B-field lines plotted. The computer was thus used to verify the magnetic measurements and to "fine tune" all parameters of the final pole piece design. It leads us to choose a gap of 3/32" as optimum spacing. This computer program is seen to be a vital tool in the analysis of different pole piece geometries and was in fact useful for the verification that tilting the axis of the poles 27°, to accommodate the projectile in the small gap, would have no substantial effects on the overall field uniformity or significantly increase leakage flux. Hence computer modeling is of significant use in rapid design of pole pieces for EMAT inspection of differently shaped projectiles.

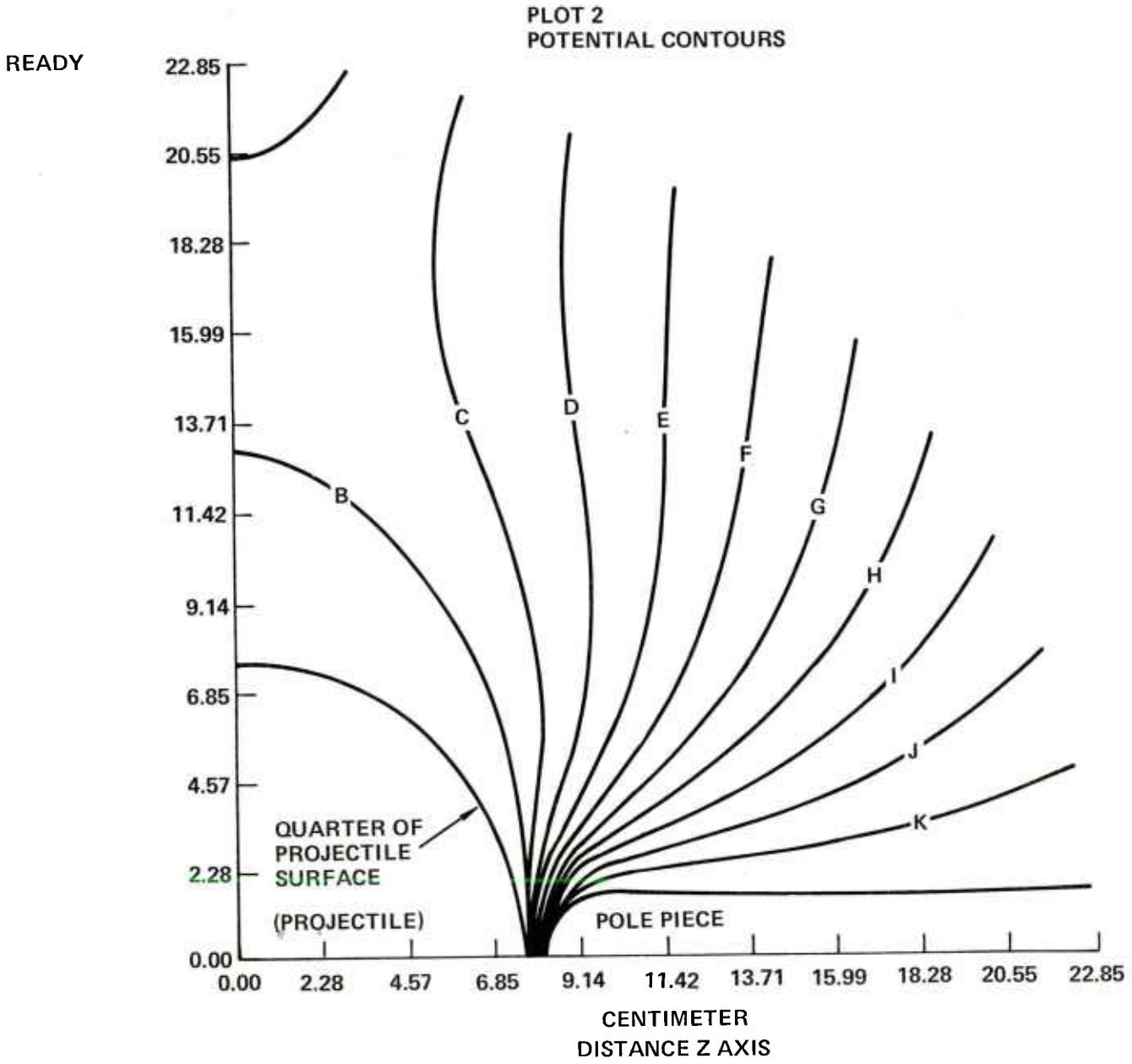

Fig. 20 Twelve magnetic equipotential contours illustrating the computed field between the projectile and a pole piece 1/4" separation of width 3/4" and beveled at 45° angle.

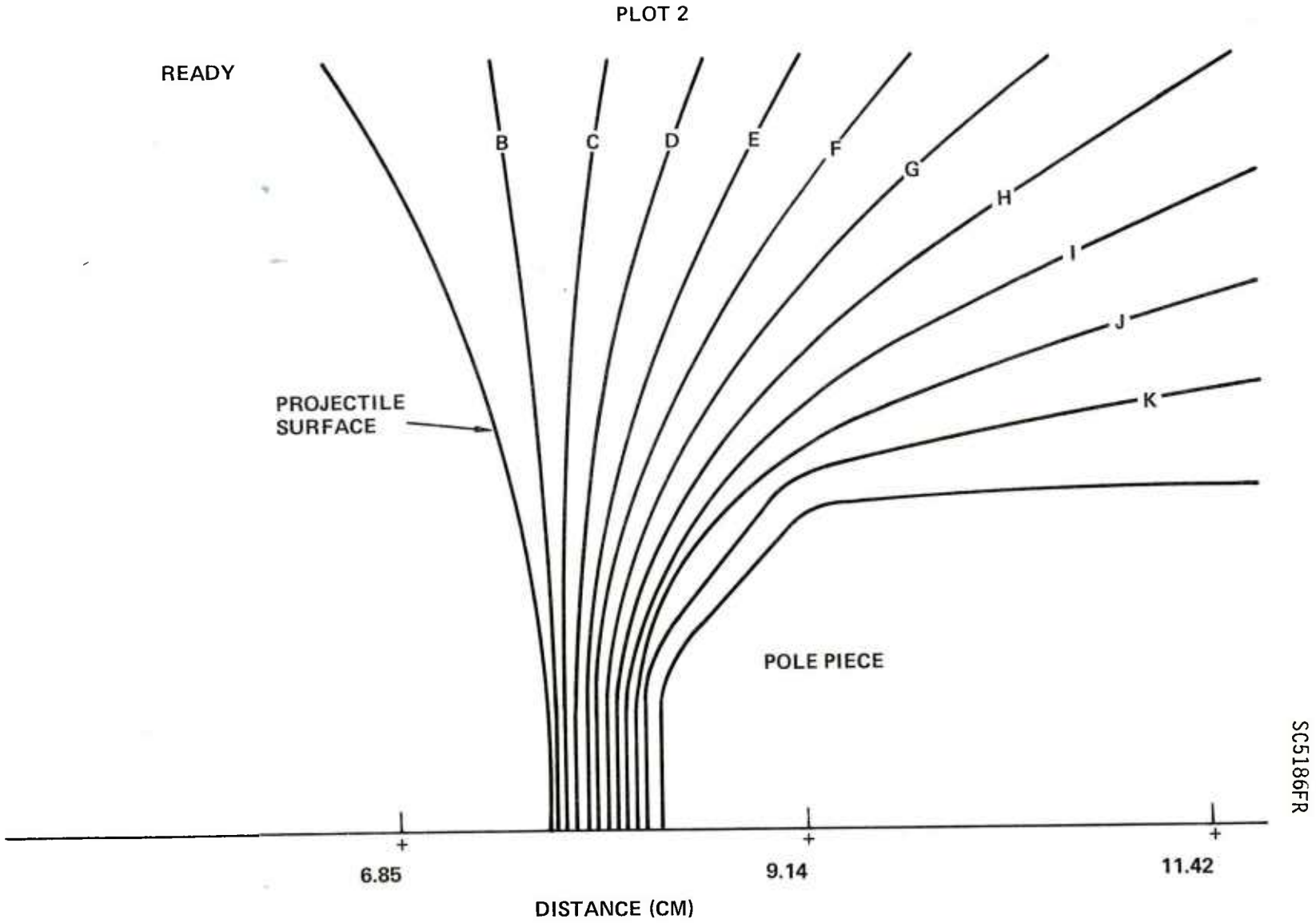

Fig. 21a Magnetic equipotential contours for 1/4" gap.

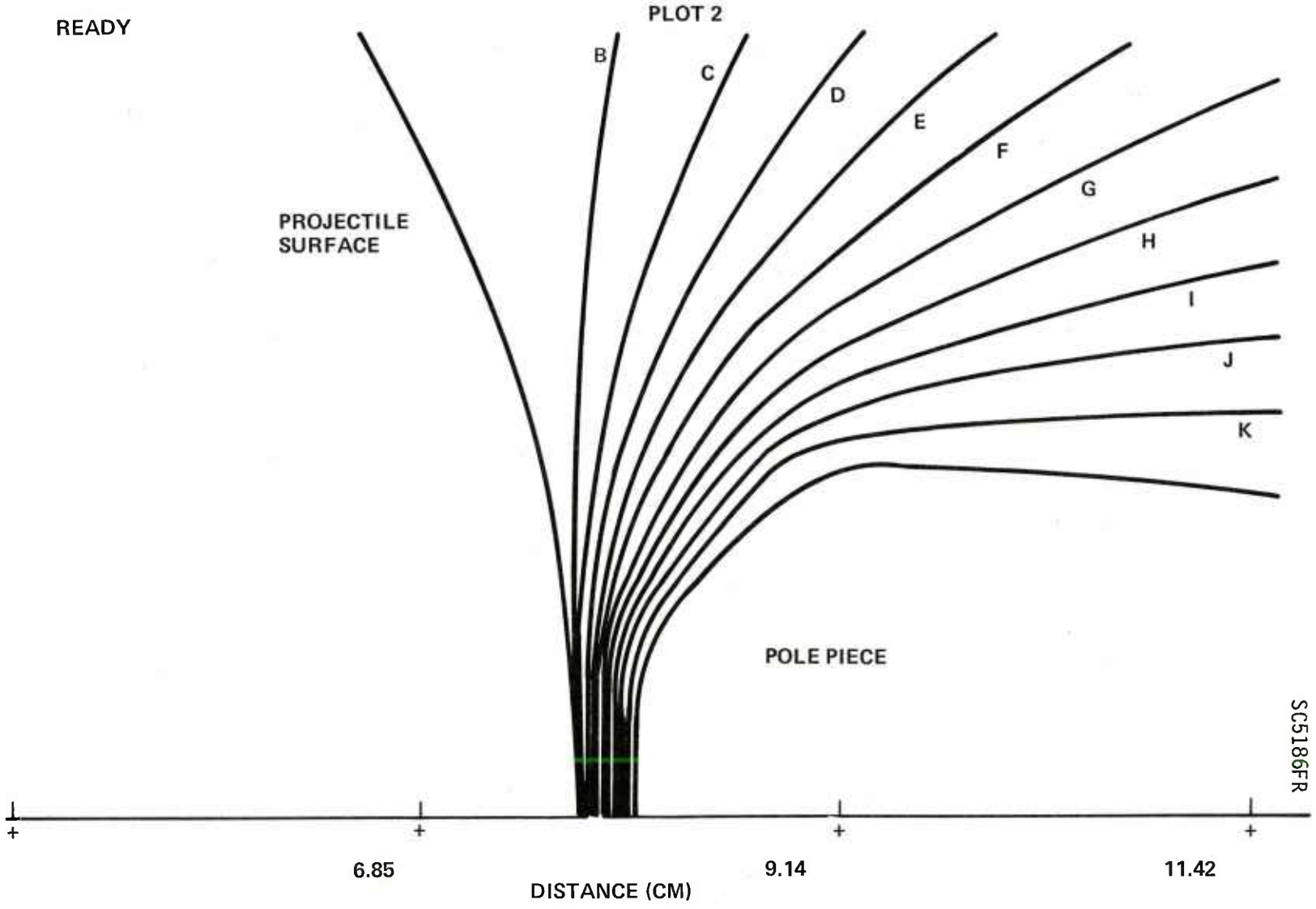

Fig. 21b Magnetic equipotential contours for 1/8" gap.

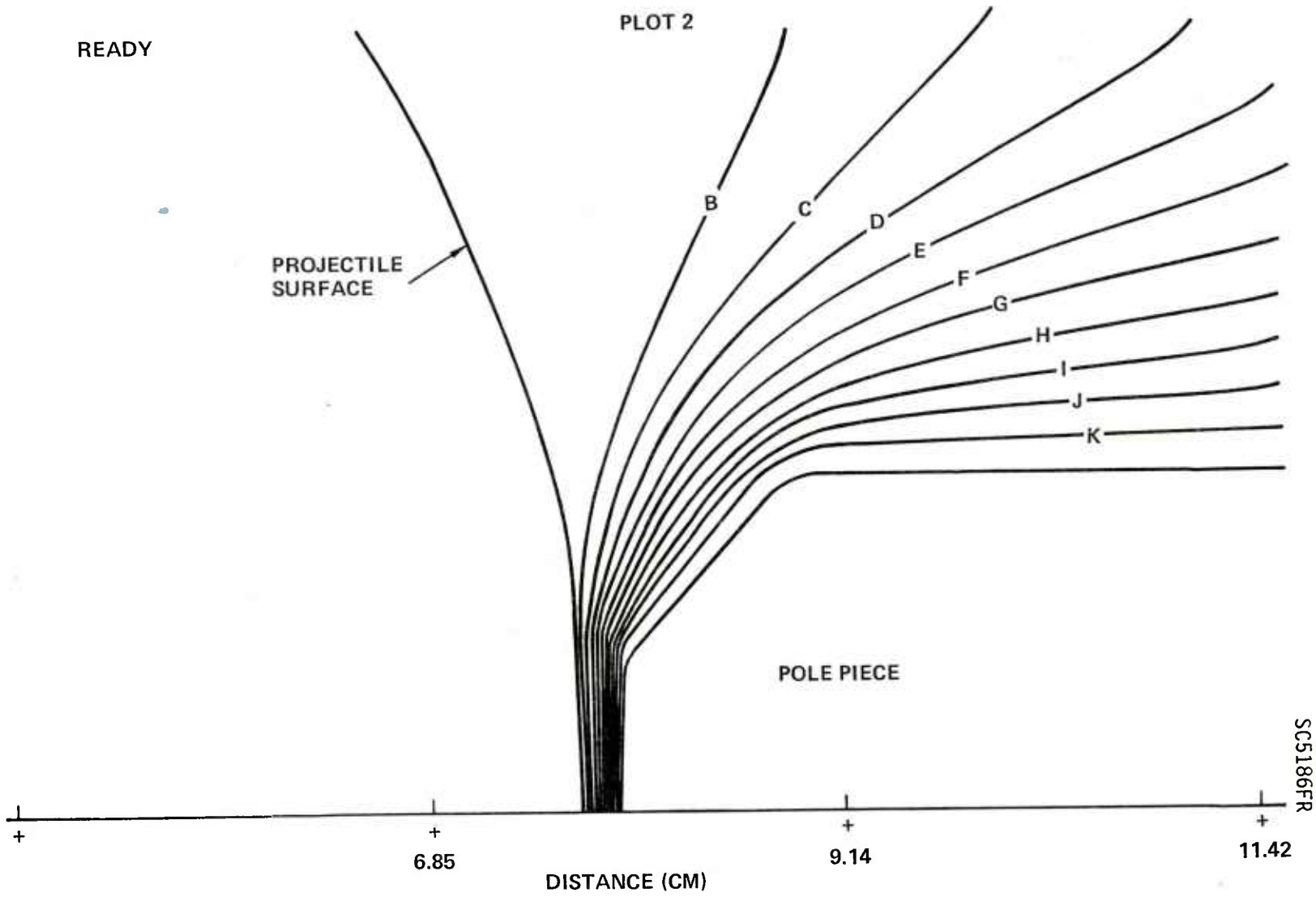

Fig. 21c Magnetic equipotential contours for 1/16" gap.

VI. EMAT ULTRASONIC INSPECTION APPROACH AND RESULTS

As shown theoretically, an EMAT meander coil can be made to efficiently produce SV-polarized shear waves into HF-1 steel at an angle of ~ 30° with respect to the surface normal. The approach chosen was to locate all EMATs along the edge of the pole piece conformable to the projectile to be inspected and inject a series of beams of ultrasound into the shell that would bounce back and forth between the inner and outer walls. The beam of acoustic energy could thus interrogate both the inside and outside walls as well as anywhere between. Figures 22 (a) and (b) depict EMATs producing beams of SV-waves and the resulting acoustic ray-paths that are expected for reflection off the inner and outer surfaces. For circumferential flaws, the EMAT is situated to send a beam parallel to the axis of the projectile and the cross-section is like that of a plate, (Fig. 22a), while for longitudinal flaws the EMAT is oriented to produce a beam that bounces around the circumference (Fig. 22b).

The EMATs are operated as both transmitters and receivers of ultrasound (pulse echo mode) so that the reflections or returns from any flaws present in the projectile can be time resolved and detected. Figure 22(c) shows an anticipated EMAT signal when inspecting a part having multiple flaws located as shown in Fig. 22(a) or (b). There is a large initial signal that is direct detection of the drive pulse. This generally saturates the electronic amplifier circuits attached to boost the EMAT acoustic returns and will exponentially ring down to the electronic noise level. Generally, the ring

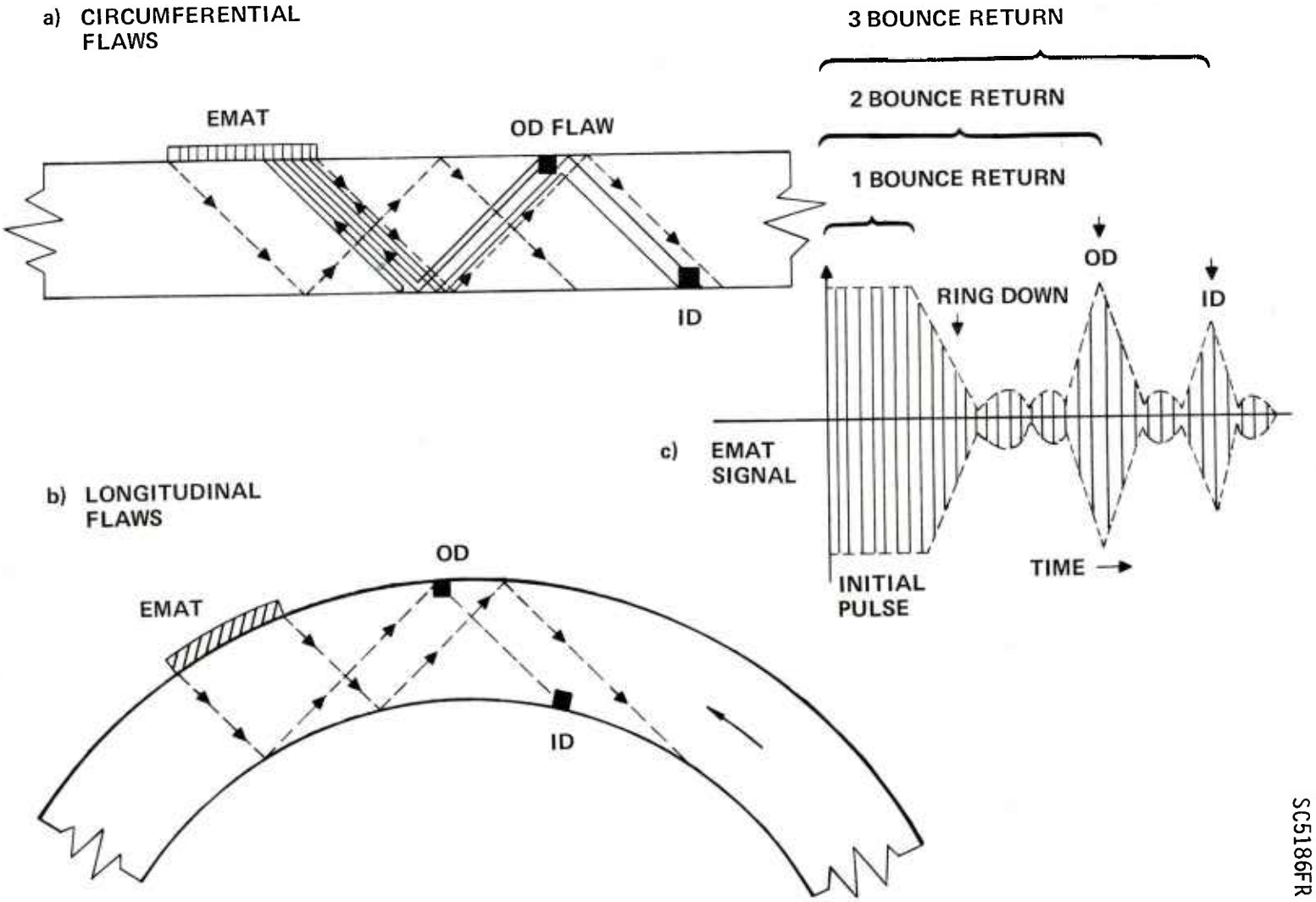

Fig. 22 Ultrasonic approach for projectile wall inspection. A) and B) show EMAT orientation for circumferential and longitudinal flaws, (C) depicts the expected acoustic return signal from the EMAT.

down is long enough, due to the moderate Q of the electronics, that flaws located on the ID surface (that would detected by a single bounce of ultrasound) are lost. However, as the ultrasonic pulse propagates back and forth, an OD flaw located 2 bounces away will be resolved as will an ID flaw located so as to be illuminated acoustically on the third bounce. After three bounces, the acoustic beam begins to be dispersed and poor return signals are detected.

Figure 23 shows experimental results of an EMAT (located on the outside of the projectile) detecting a series of 0.020" deep by 1.00" long EDM (electron discharge machined) notches. Here the ringdown was adjusted to allow flaw detection on the first bounce, however this was not employed in the final inspection equipment. Although the return acoustic signals are easily detectable here, further advances in electronics and magnet design improved the signal-to-noise (S/N) ratio for flaw signals in the final unit to over 30dB. Since the EMAT transducer locations are fixed beneath the magnet pole piece, to achieve full projectile wall coverage the following methods were employed:

(1) for longitudinal flaws, the projectile is rotated about its axis and this sweeps the flawed regions into the EMAT inspection zone.

2) circumferential flaws are detected by making an array of EMATs along the projectile axis which covers the entire wall volume because of the transducer bidirectional characteristics.

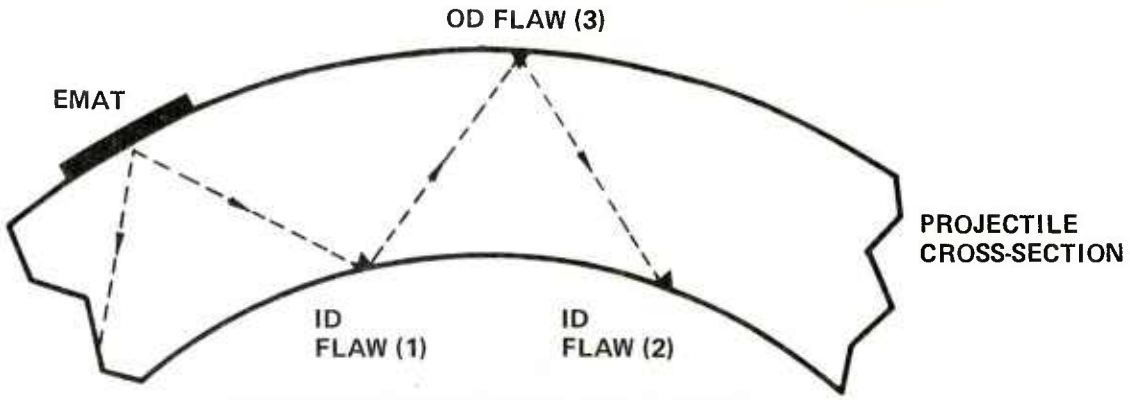

INSPECTION OF PROJECTILE WALL WITH
SHEAR-VERTICAL ACOUSTIC WAVES

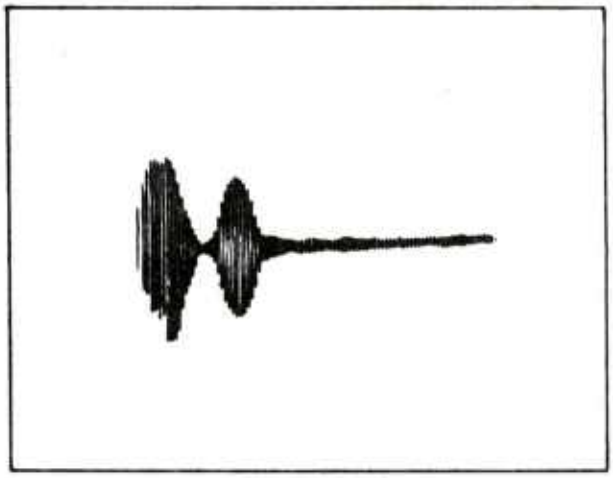

a) ID FLAW
(# 1)

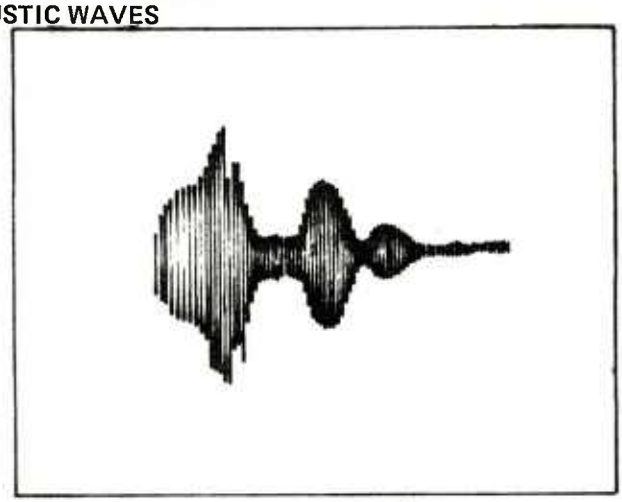

b) OD FLAW
(# 3)

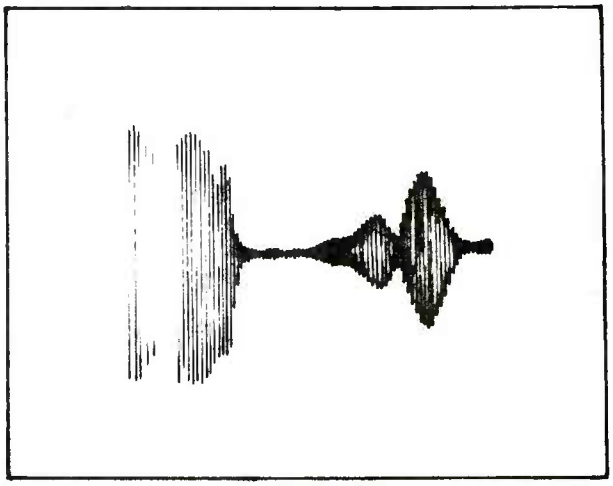

c) ID FLAW
(# 2)

Fig. 23 EMAT detection of OD and ID flaws by bouncing acoustic beam approach. Note different time delays allow differentiation between flaw locations.

The "acoustic beam" approach was chosen so that higher frequency ultrasonic waves could be utilized. A guided or Lamb wave could have been used which fills the entire wall with energy. However, for parts of the wall thickness the wavelengths would be about 0.4" long (frequency = 225KHz) and these waves would be very weakly scattered by the 0.020" deep standard flaws. Thus we chose to use a shear wavelength, λs, of 0.06"(1.5 mm) and operate at 1.94 MHz. This wavelength has good scattering characteristic for flaws in the 0.02" and smaller size when illuminated at a 30° angle. This wavelength is sufficiently small, being 6.7 times less than the wall thickness, and will propagate mainly as a beam and not break up into guide wave energy. Therefore, this 1.97 MHz frequency was found to yield an acoustic beam having good reflection characteristics with only slight spurious mode generation.

The remainder of this chapter details an extensive set of acoustic experiments that were made using a single EMAT to measure the characteristics of the total flaw detection process. The transmit/receive electronics used to interface to the EMAT are similar in design to that used in the final system implementation. The EMATs and magnetic structures were of the same configuration as the final designs. Thus these results closely parallel measurements taken on the delivered hardware.

The first tests were made to determine how large a region the EMAT was able to cover. The 3mm period EMAT had a longitudinal aperature of 13/16" or 2.06 cm in the direction of launch and was 1" wide. The OD circumferential flaw (2-bounce signal) could be detected with 8 volts or more acoustic return

over a 1-1/2" (3.8 cm) region starting 1" away from the EMAT center (see Fig. 24). A similar plot is shown for an ID circumferential flaw where > 8 volt signals are obtained over a 1-3/8" (3.5 cm) region starting about 1-1/2" from the EMAT center (Fig. 25) and a plot taken for a longitudinal oriented flaw shows that 8 volt returns are achieved over 3/4" long region (Fig. 26). Hence the EMATs have a sufficient inspection area to yield complete projectile coverage if properly arranged.

Figures 27 and 28 show the quality of the detected return signal from 0.020" deep notches for several projectile locations in the bourrelet. At a magnetic field of 15 KG, the OD flaw signal output reached 13 volts (receiver saturation) while the ID flaw was 6 volts (which could be increased to 13 volts by raising the field to 20 KG - Fig. 28b). Figure 29 illustrates the EMAT detection of ID circumferential flaws in the ogive section compared to the bourrelet. The ogive signal is observed to be stronger in this test because the projectile has uniform wall thickness. The bourrelet section has tapered walls and yields a less "clean" return signal (exhibits interference). The solution to this problem was to make an EMAT with 10° off-axis electrodes. This EMAT configuration compensates for the projectile wall variation and restored the strong reflected signal amplitude.

EMATs with different number of periods were investigated to determine the effect on signal quality. Figure 30 (a) and (b) compares the return signals observed for a 7 period and 4 period EMAT. The 7 period unit yields stronger signals because of a) the more efficient coupling due to the larger number of acoustic sources, b) the narrower beam that it produces confines the

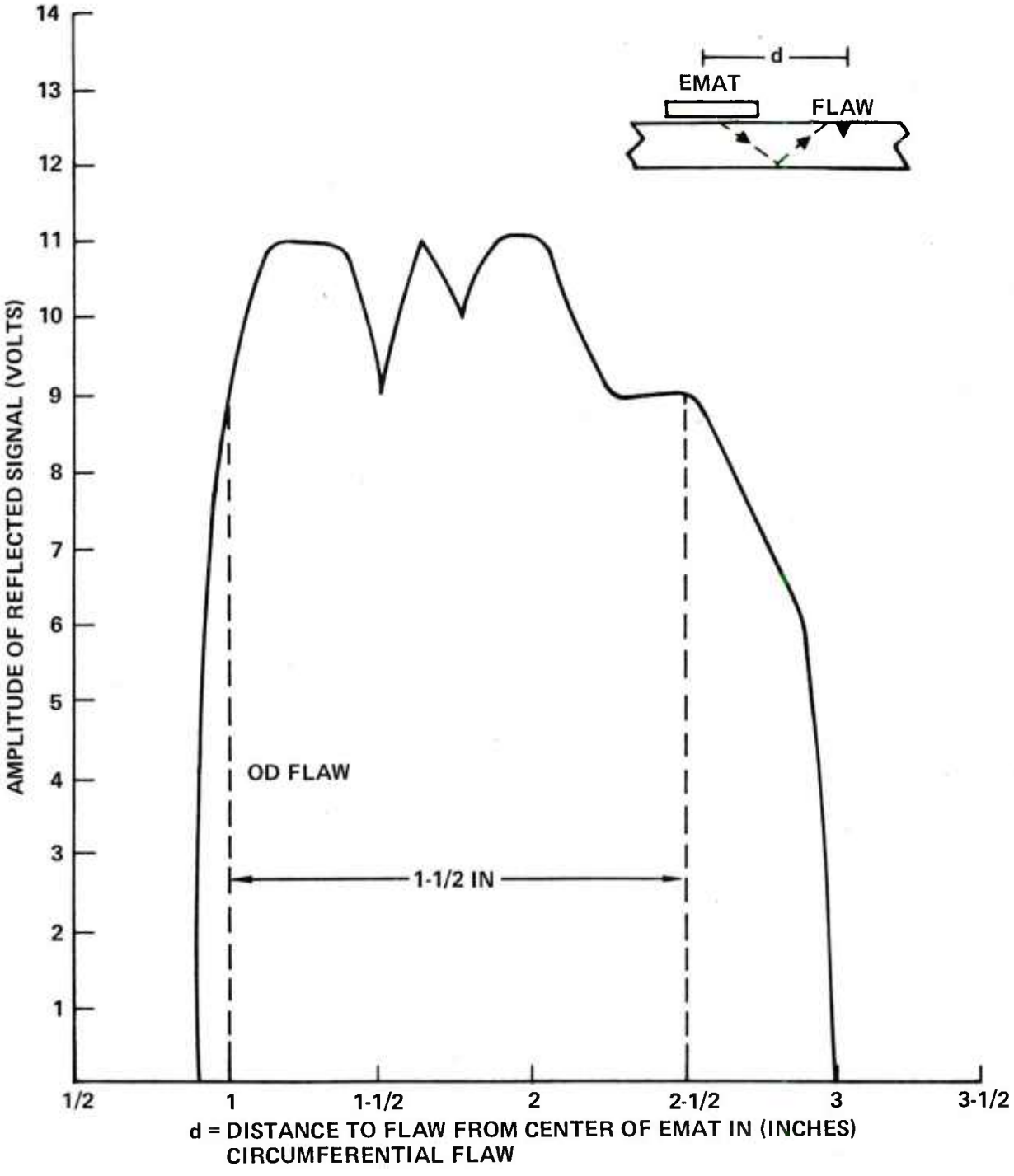

Fig. 24 EMAT sensitivity region for OD flaws (2-bounce signal).

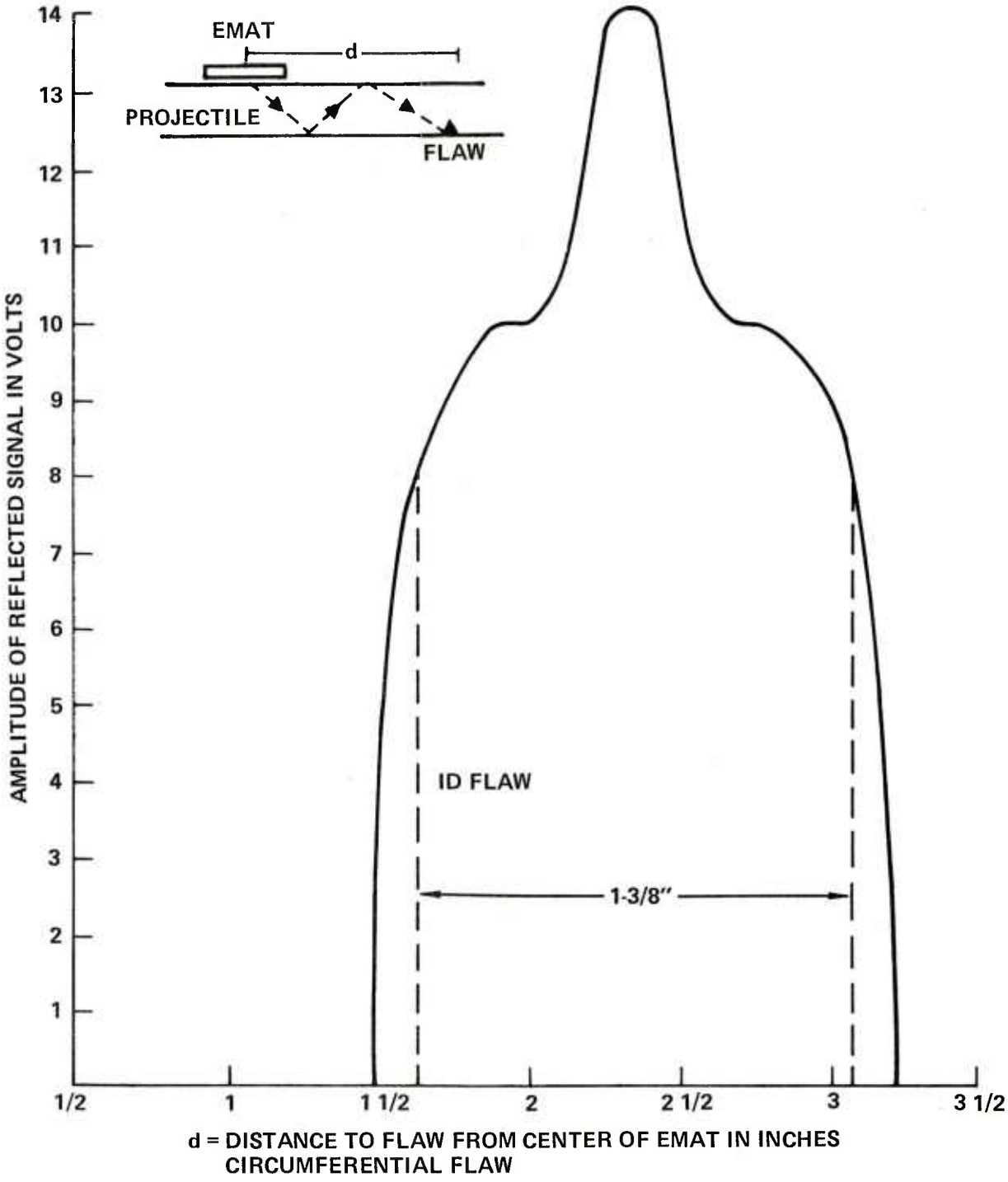

Fig. 25 EMAT sensitivity region for ID flaws (3-bounce signal).

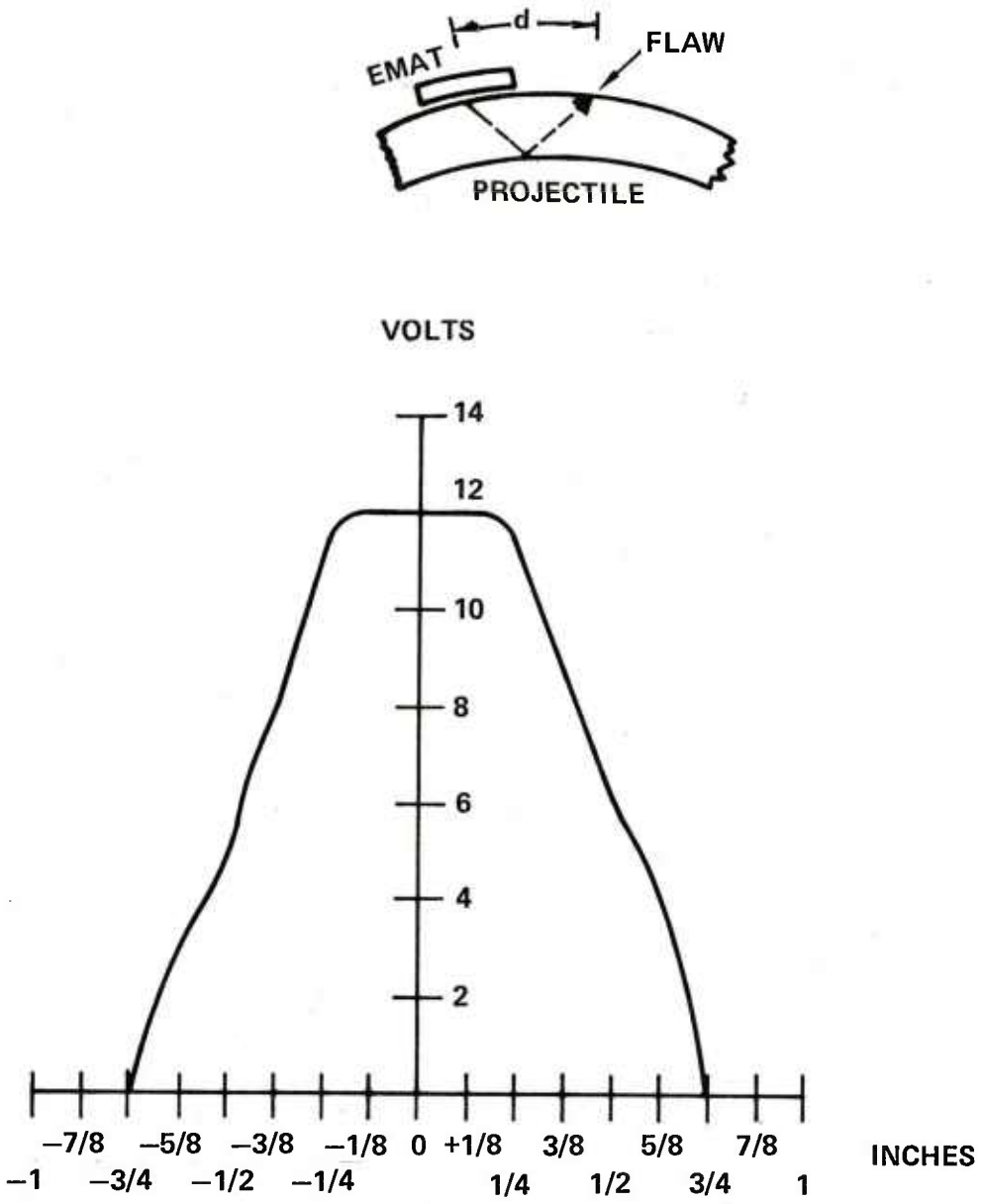

Fig. 26 EMAT sensitivity region for longitudinal flaw.

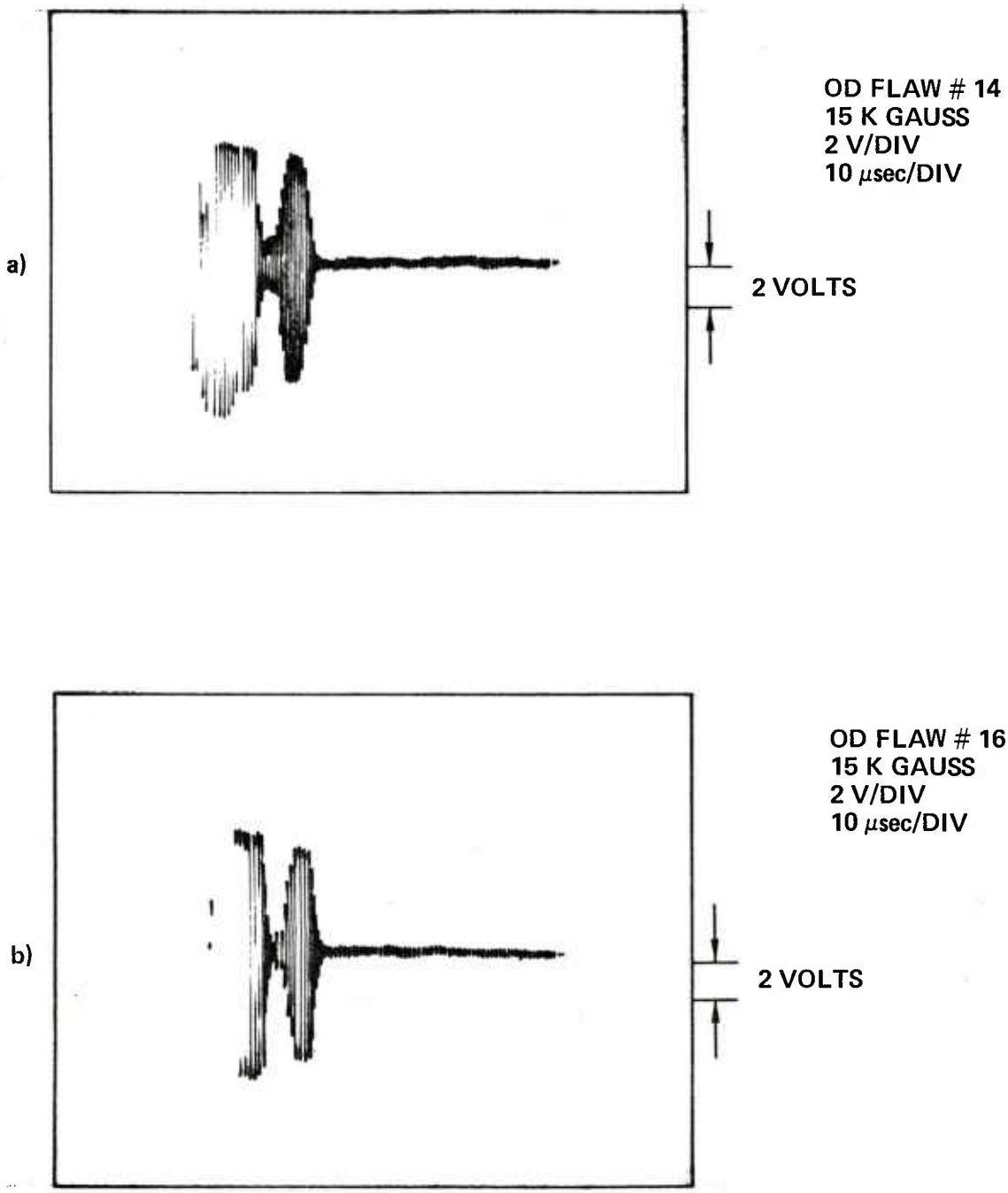

Fig. 27 Detection sensitivity for OD flaws by single channel EMAT and associated electronics.

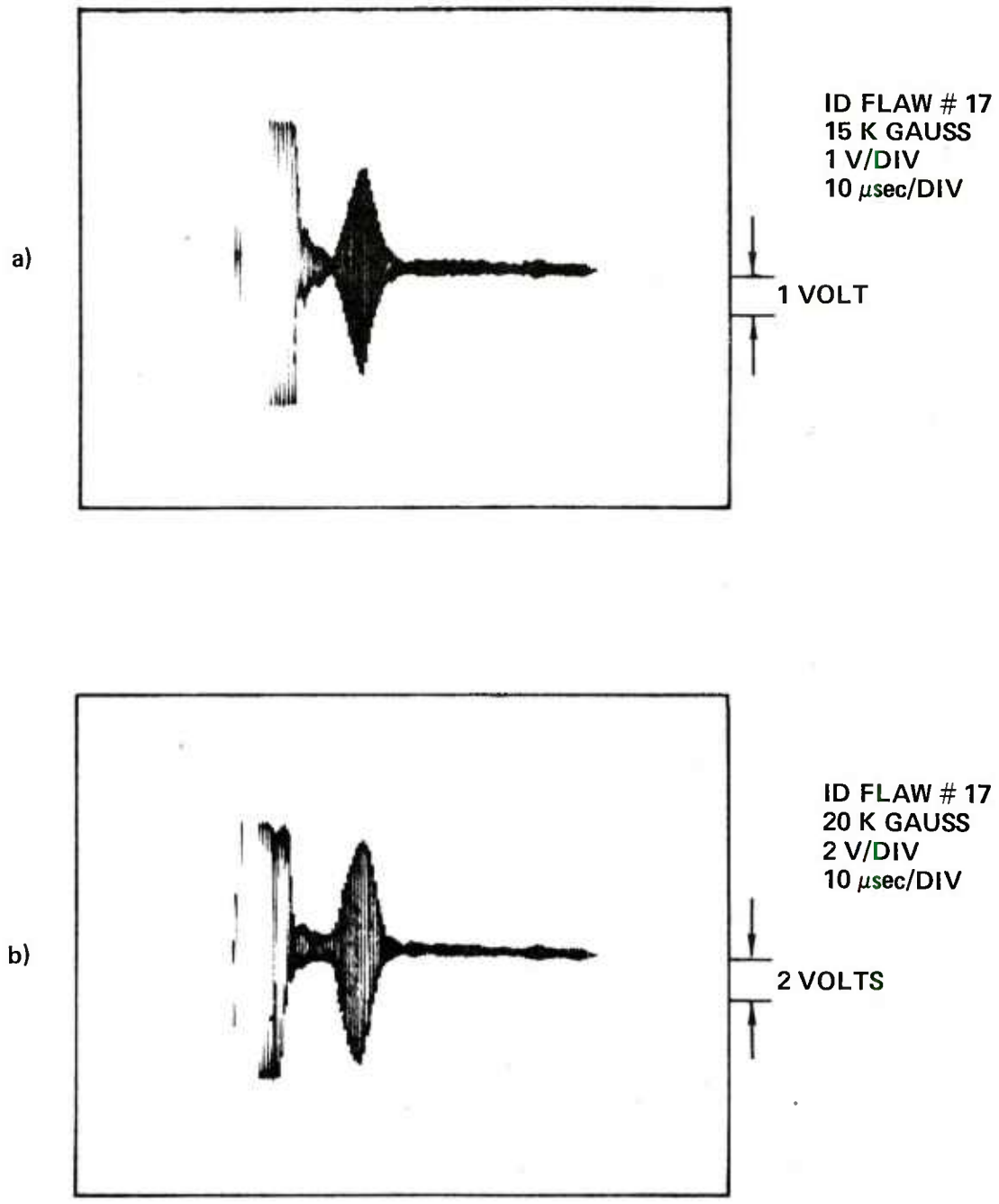

Fig. 28 Detection sensitivity for ID flaws by single channel EMAT and associated electronics.

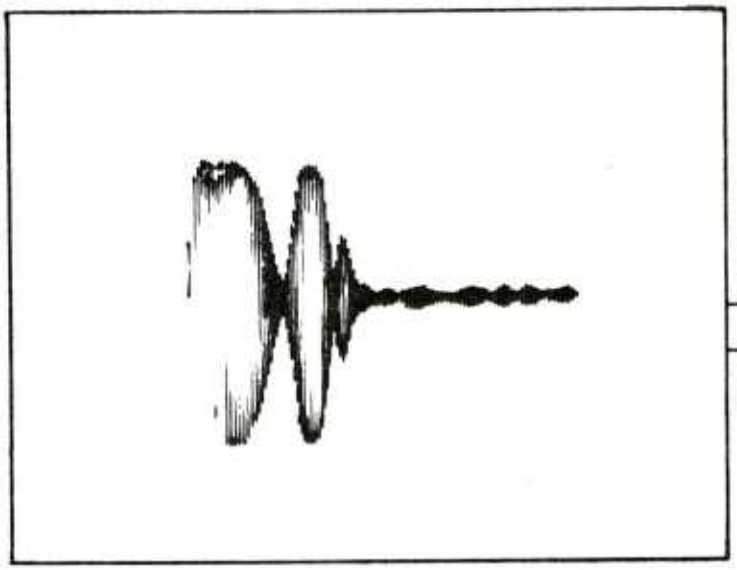

a)

ID CIRCUMFERENTIAL
FLAW (ORIG. STD.)
18 K GAUSS
2 V/DIV
10 μsec/DIV OGIVE

2 VOLT

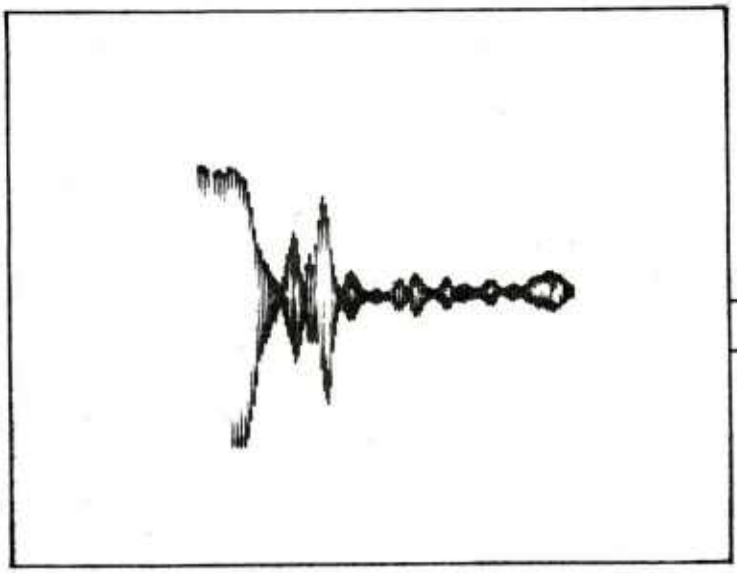

b)

ID CIRCUMFERENTIAL
FLAW (ORIG. STD.)
18 K GAUSS
2 V/DIV
10 μsec/DIV BOURRELET

2 VOLT

ID CIRCUMFERENTIAL FLAWS
PROJECTILE IN LARGE MAGNET

Fig. 29 Comparison of EMAT standard flaw detection in ogive and bourrelet sections of projectile.

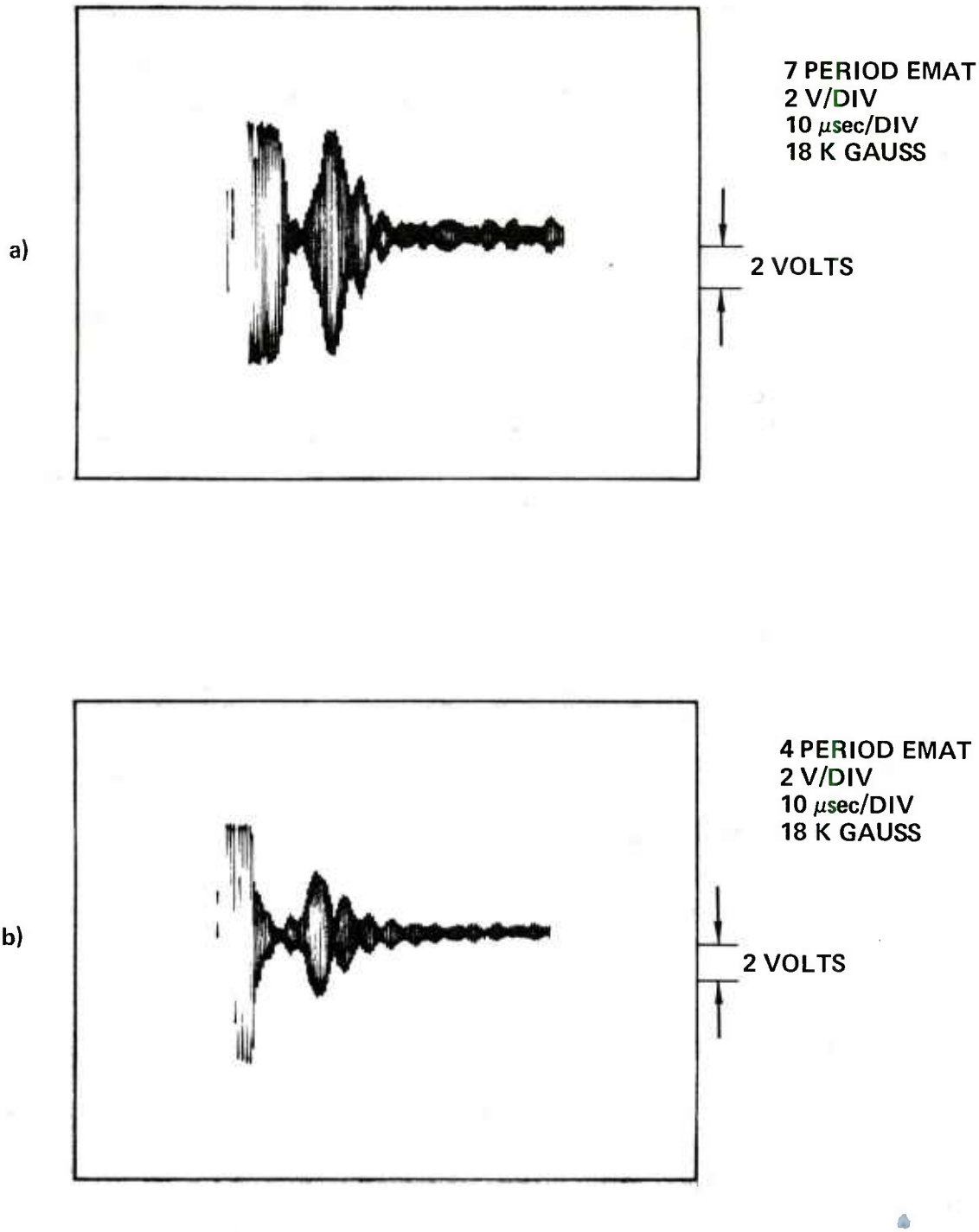

Fig. 30 Effect of using a different number of periods in the EMAT.

acoustic energy to the desired direction, and c) its larger electrical inductance which is easier to match. Because of the broad emission of ultrasound in the 4 period EMAT, sufficient energy is launched vertically so that strong reverberation signals can be observed which are due to waves bouncing between the inner and outer walls. Thus a 7 period unit was used in the final EMAT implementation where maximum signal is desired and 4 period units used where space restriction required minimum size.

Due to the high rate of projectile throughput, it was determined that the EMAT must make measurements on the projectile as it was being rotated. Thus we investigated the dynamic effects (i.e., relative motion between the transducers and the shell) which might degrade the acoustic signals. Figure 31 a) and b) shows the baseline clutter noise level both in the static case and rapidly rotating (300 rpm) case. Since the clutter noise remains approximately the same magnitude, no excess noise should be added by rotating at 40 rpm, the chosen inspection rate. Likewise, Fig. 32 illustrates that the signals obtained from the rapidly moving projectile are almost identical to those observed in the static situation (Figs. 27 and 28). EMAT inspections can thus be performed while the projectile is being rotated which leads to reduced overall inspection time.

An exhaustive set of tests were carried out on the base region of the projectile to determine if the critical flaws could be detected there. The base is a particularly difficult region to ultrasonically inspect due to the curved inner radius and the various protrusions (all of which either scatter acoustic beams or add spurious reflections). No definite method was evolved

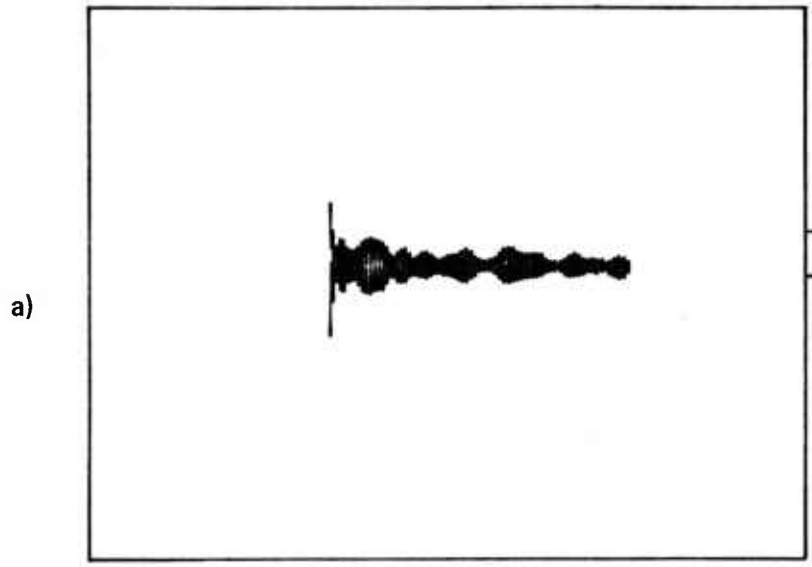

Fig. 31 Baseline clutter noise detected for static and rotating bourrelet section of projectile.

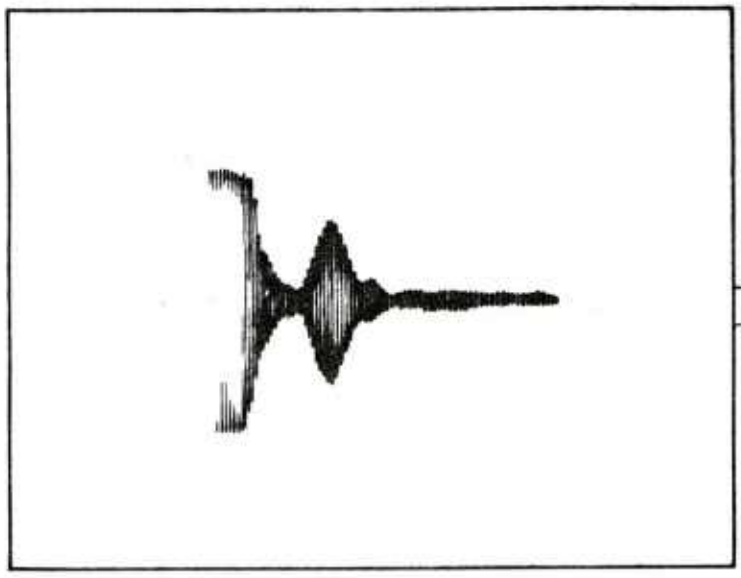

ID LONGITUDINAL
FLAW 0.020" DEEP
19 K GAUSS
2 V/DIV
10 μsec/DIV

2 VOLTS a)

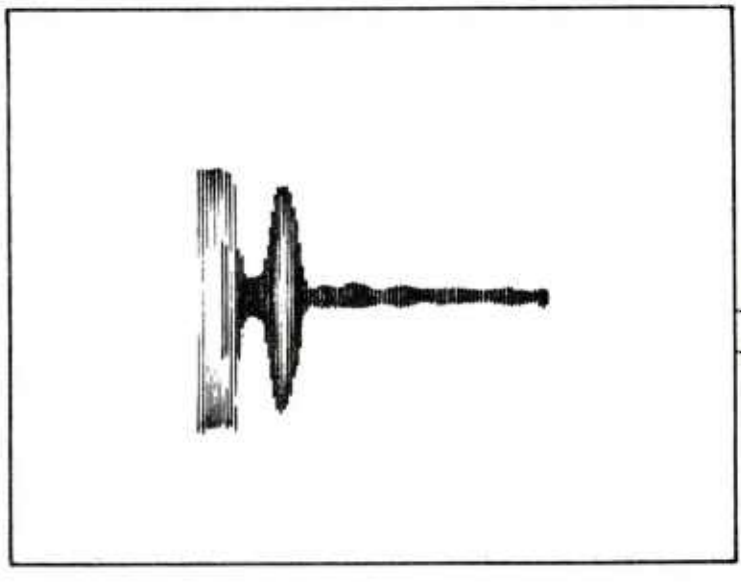

OD LONGITUDINAL
FLAW 0.020" DEEP
19 K GAUSS
2 V/DIV
10 μsec/DIV

2 VOLTS b)

ROTATING BOURRELET SECTION 300 RPM

Fig. 32 Effect of projectile motion on detection of flaws by EMATs.

to detect the inner base notches. However, a viable approach was established to find flaws on the outer surface of the base. This is shown schematically in Fig. 33 b) and c) where a surface wave (launched at 1 MHz) is directed at the base flaws. The reflected signal is either returned to the sending EMAT b) or to another EMAT c). The photograph a) shows that adequate signal to resolve the acoustic signals is achievable. This surface inspection technique was not implemented on the final unit because of time constraints but could be retrofitted at a future date.

Figure 34 plots the observed EDM notch signal and clutter noise amplitude as a function of applied magnetic field. This plot is similar to the final result but about 50% lower amplitude. It, however, illustrates the following points. First, the return signal level is highly nonlinear and rises to an acceptable level at 19 or 20 KG. The nonlinearity is believed to be due to the field homogeneity and uniformity improvements as the shell begins to saturate magnetically. Also, the "noise" level detected is due to acoustic clutter signals and is not due to the intrinsic electrical noise of the EMATs amplifier components (which is about 20 μ volts). The clutter signals are due to the acoustic scattering that occurs as the waves bounce off the rough (or wavy) inner projectile surface. This waviness is attributed to the forging process. Thus the signal to noise ratio of any ultrasonic inspection approach, using either EMATs or conventional piezoelectrics, will be limited by this mechanism. Hence, EMATs should be of comparable sensitivity to conventional ultrasonic detection methods when operated at the same frequency and at the same inspection angle.

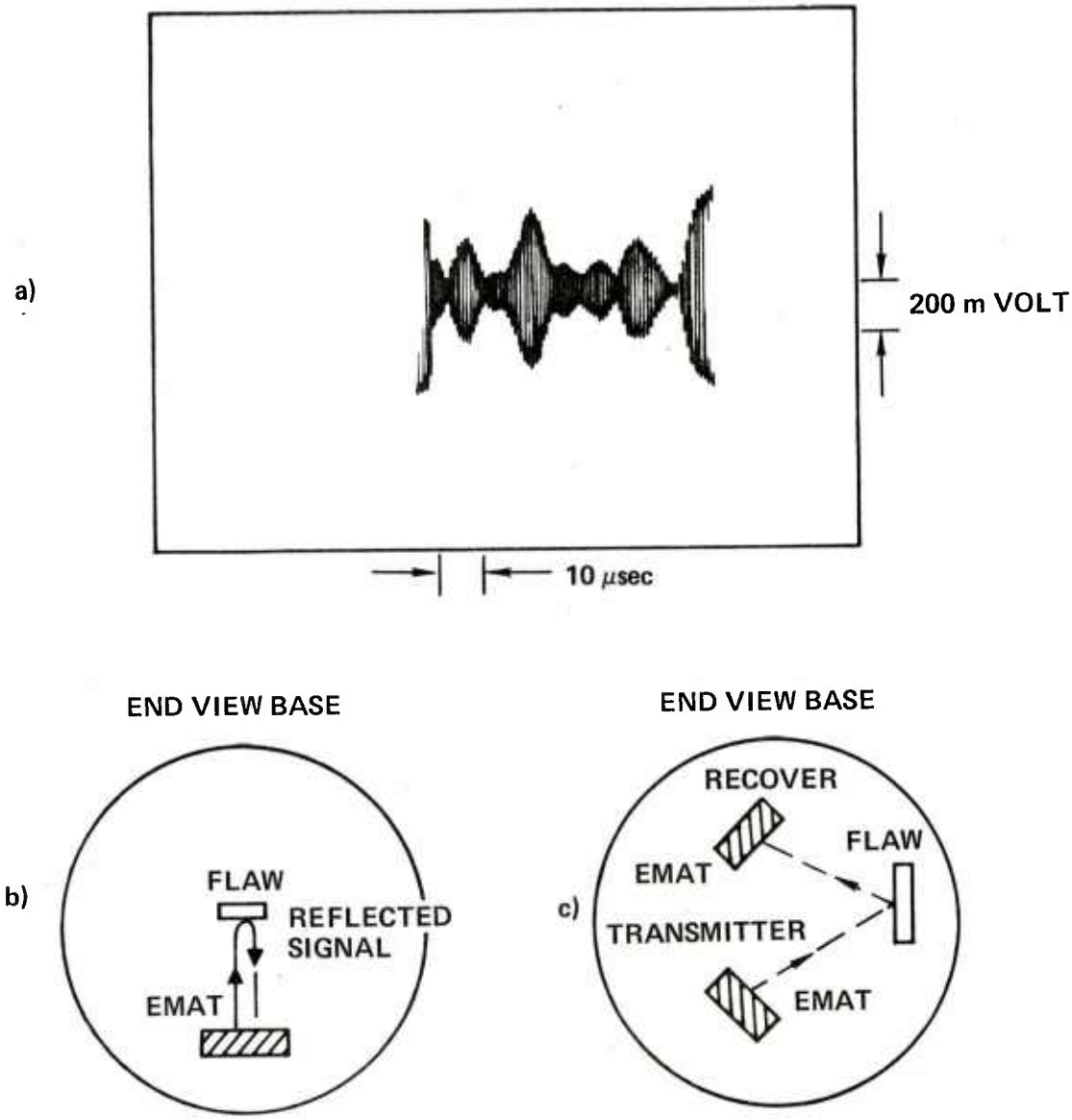

Fig. 33 Inspection of base outer surface notch using surface acoustic wave at 1 MHz.

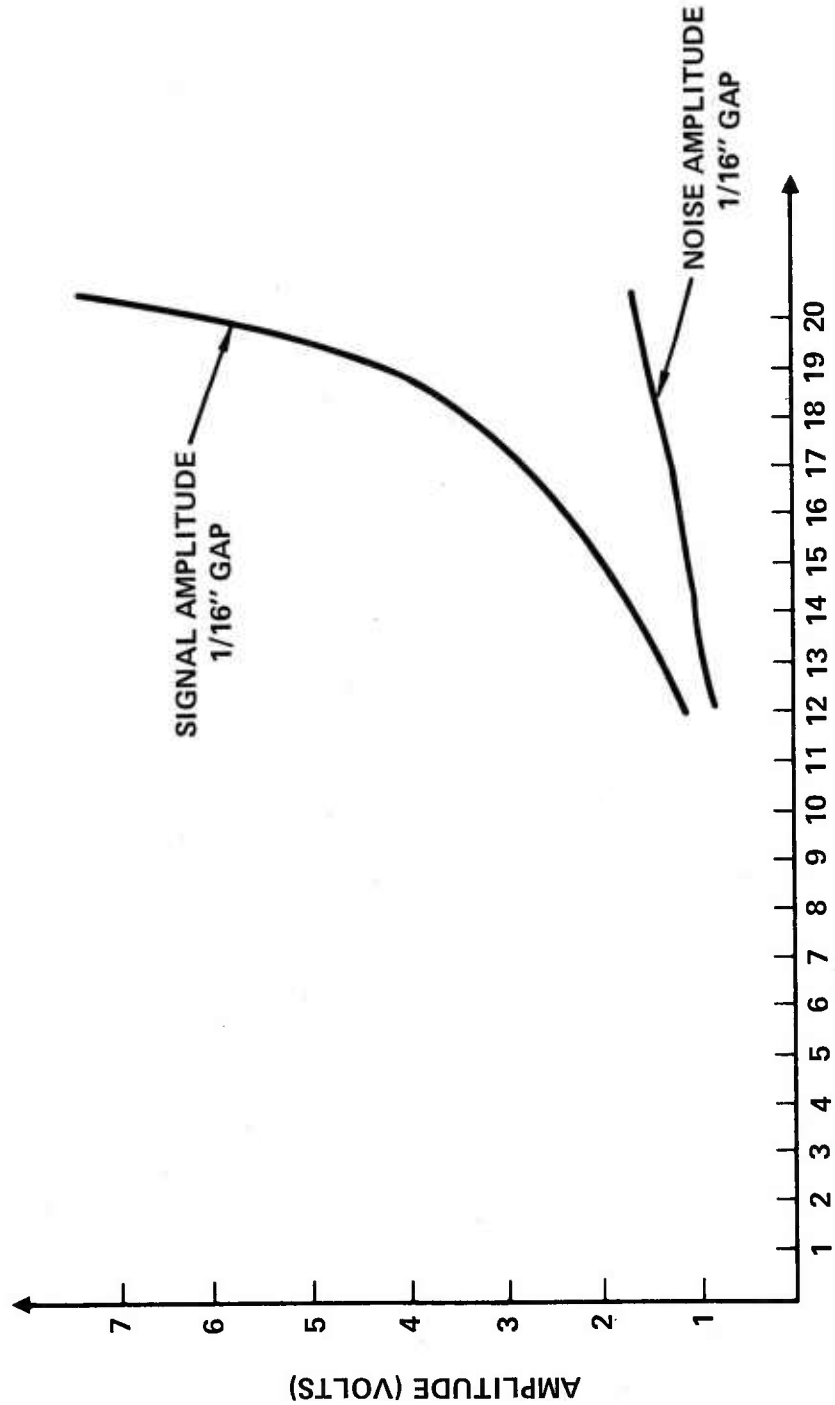

Fig. 34 Signal amplitude and clutter noise amplitude vs field strength for ID longitudinal flaw.

In concluding this section, it is enlightening to list the several technical problems which were both encountered and ultimately solved in order to produce a viable projectile inspection technique using EMATs.

Table 1

Acoustic Problems Identified with EMAT Inspection of Projectiles

Problem	Solution	Comment
1. Poor EMAT efficiency in tangential B-Field on Norris projectiles	Use normal B-field configuration	Identified in Phase A
2. Poor EMAT efficiency in normal B-field	Sophisticated Magnet Design to produce uniform, normal high intensity B-fields at EMAT coil	
3. Spurious echo signals observed	Add more periods to EMAT coil (4 up to 7) to better confine ultrasonic beam	
4. Could not detect ID flaws	Higher B-fields and better EMAT design overcame poor signal quality	Observed during Phase A
5. Could not resolve ID flaws on first bounce	Improved ring down time of electronics and detect ID flaws on third bounce	
6. Portions of bourrelet yield poor signal quality	Build a 10° tilted EMAT to compensate for non-parallel projectile walls	
7. Base is difficult to inspect using bulk shear wave EMAT	Design a special surface wave EMAT that detects outer surface base flaws	Not all standard flaws can be detected
8. EMAT highly effected by lift-off from projectile surface	Specially designed spring loaded EMAT support that holds transducer within 10 mils of surface	See design next section

VII. ANALOG ELECTRONICS

The analog electronics that are required for EMAT operation are composed of a high power amplifier to excite the acoustic waves and a low-noise receiver to boost the return (reflected) signal level. Both units are optimized for the 1.94 MHz EMAT frequency. The situation is somewhat complicated by the fact that the same EMAT coil is used for sending and receiving energy so that ways of preventing the full transmitter power from being sent into and damaging the receiver were required along with advanced design techniques to optimally couple (match) the EMAT to the electronics. The electronics were implemented using all solid state components and construction practices (such as heat sinking) and operational procedures (such as conservative device biasing) were used which should lead to long reliable operation. No unit failures were encountered during our several months testing program in which all 50 electronic transmit/receiver (T/R) modules built were test operated.

The transmitter/receiver units (shown in Fig. 35) were fabricated on a printed circuit (PC) board that had edge connectors to transfer the electrical signals and provide dc bias. The high power bipolar transistors (2N6277 and 2N6341) were heat sunk to the PC board and radio frequency (RF) signals were routed to the output by coaxial lines to prevent radiation. Since the transmitters are operated in the pulsed RF mode with less than 0.5% duty cycle, thermal effects were minimized. The circuit layout also tends to reduce electrical cross talk between the transmitter and receiver.

SC80-9472

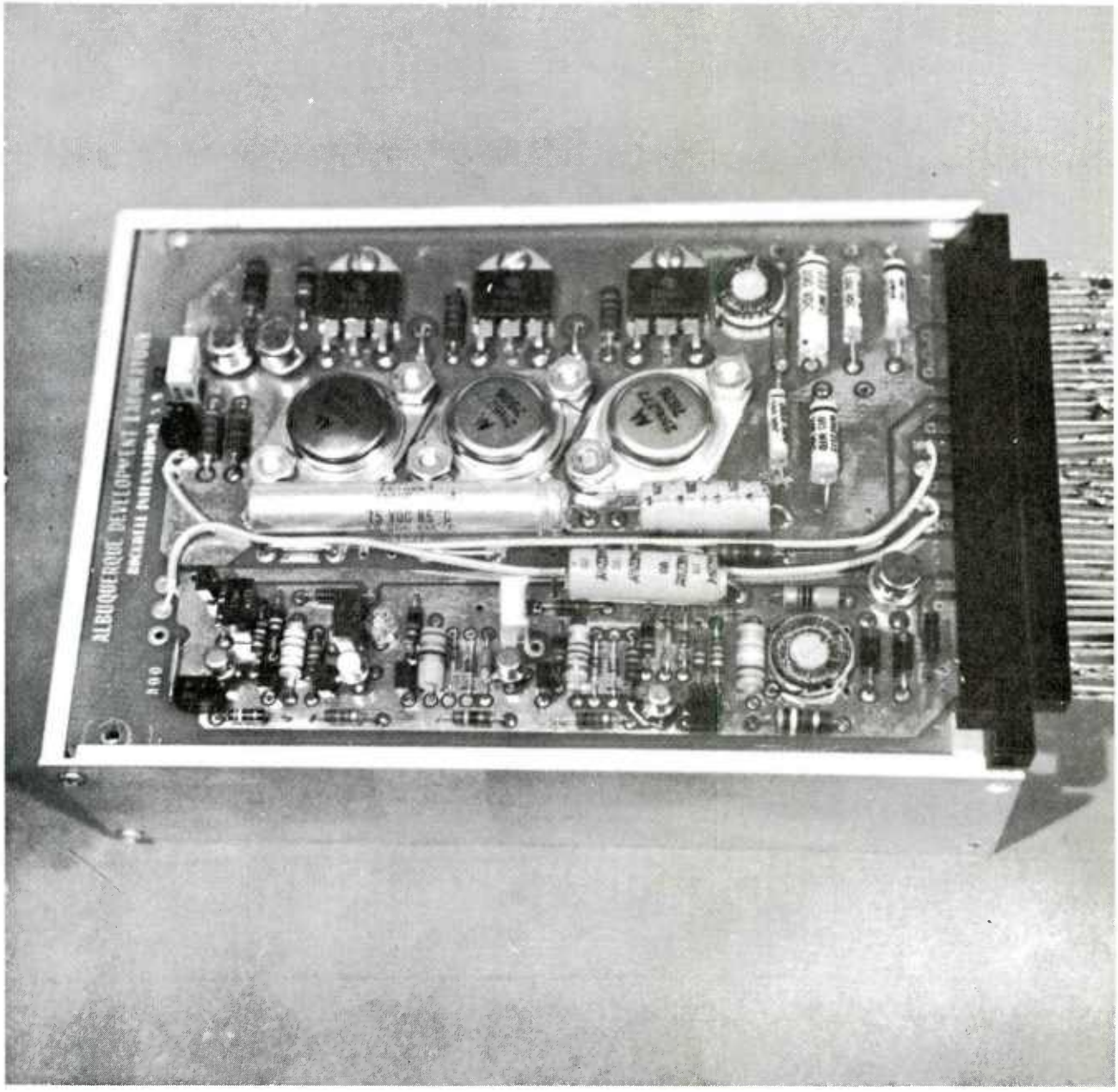

Fig. 35 Photograph of RF transmitter/receiver board.

Figure 36 shows a detailed schematic of the electronics. The transmitter uses a 60 V dc bias and is driven by a TTL level (2-5 volts) square wave input. The RF signal is boosted to a pulse level of about 80 amps at the output and is coupled to the EMAT coil by a transformer and matching capacitor C_{11} to resonate out the coil inductance. The reflected signal is input to the low noise FET preamplifier by a diode switch and limiter that protects the input transistor stage. An acoustic signal input of 40 μ volts will be boosted to a 3 volt level at the output. Substantial design effort was focused on achieving good ring-down characteristics by a) providing isolation at the input of the circuit, b) maintaining modest circuit Q^S and c) discharging any storage elements (capacitors) that would be effected by the direct feedthrough signal. Also, special bias circuit techniques were employed to reduce direct coupling. The electrical performance of the analog electronics is summarized in Table 2 and Fig. 37. This data shows state-of-the-art performance for the special EMAT circuits which leads to the superior detection capabilities that were achieved.

The final inspection system requires 44 of the T/R circuits to power the 44 independent EMAT inspection channels. These electronics T/R cards are mounted in two large card cage units that sit atop the inspection part handler. The various channels 1 through 44, are sequenced in a firing order so that signals will not cause acoustic cross-talk. All EMAT firings are under microprocessor control and interface to our system control computer. Provisions have also been made to individually operate each EMAT T/R card so that system diagnostics are facilitated.

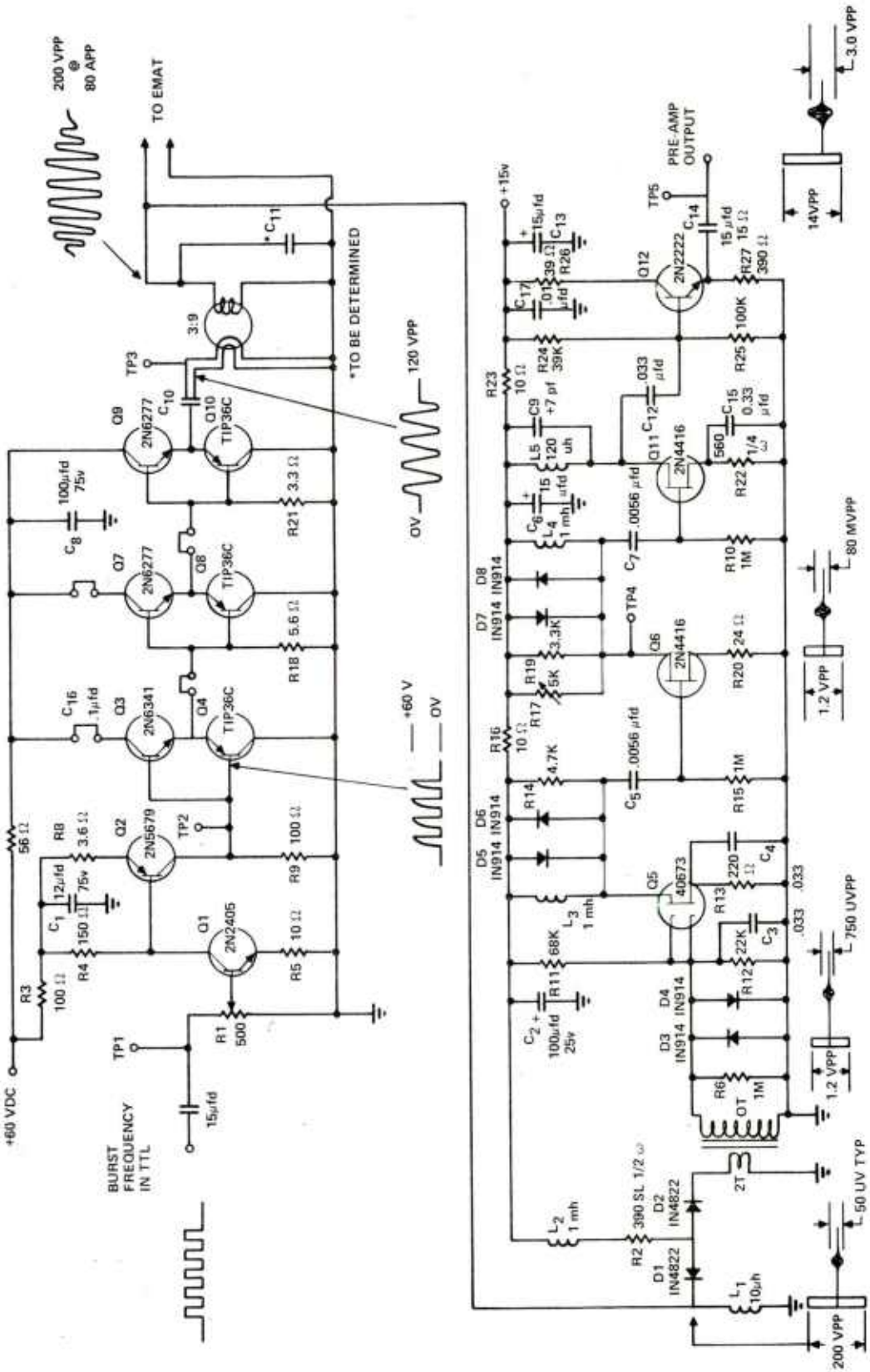

Fig. 36 Schematic diagram of transmitter/receiver card.

Table 2

Summary of Electrical Performance (Analog)

Transmitter Data (Board #1002)

Operating Center Frequency	1.94 MHz
Rep. Rate	10 ms
Number of Pulses	15
VCC	60 VDC @24 ma
Output Voltage	20 Vpp PCB Output
Transducer Voltage	85 Vpp
Transducer Current	80 A

Receiver Data (Board #1002)

Input		Output
T 1 Out	20μV	350 μVpp
Q 5 Out	20μV	6.4 mVpp
Q 6 Out	20μV	35 mVpp
Line Out	20μV	1.5 Vpp

Gain 75,000
RCV BW 270 KHz

Signal to noise 44dB W/20μV Input
(Measured in 3dB of 30 KHz)
NF 6dB

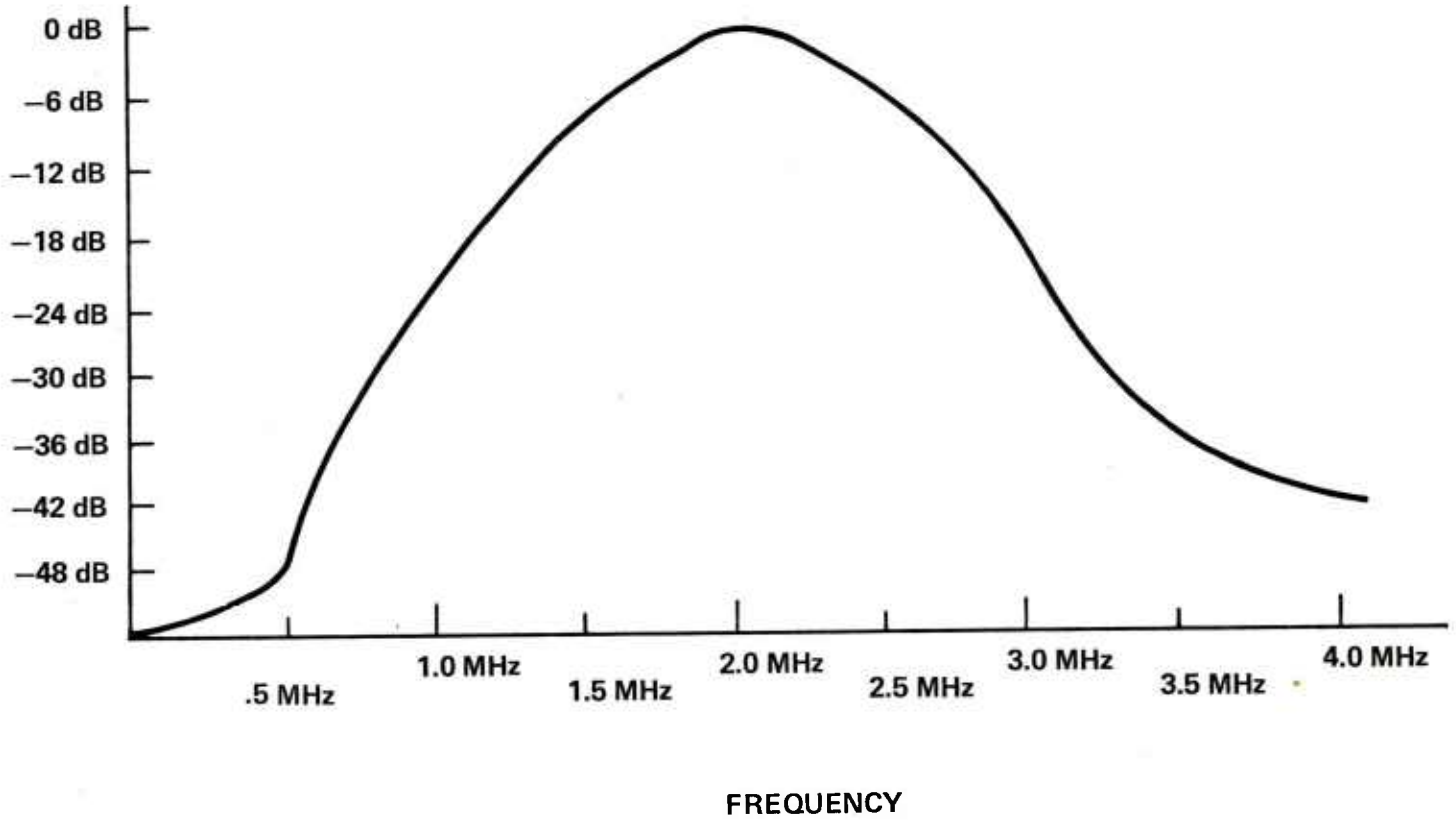

Fig. 37 Frequency response of receiver circuit.

VIII. EMAT TRANSDUCER AND SUPPORT

An EMAT coil and support assembly has been designed to meet the following goals: 1) produce SV-mode acoustic waves at a 30° angle to the normal, 2) fit in the 3/32" gap between the pole piece and projectile and accommodate any projectile dimensional variations, 3) keep a constant spacing between the coil and the projectile, and 4) be rugged and reliable in operation. These goals were addressed by several unique construction techniques. First, the EMAT coils themselves were fabricated on a thin strong "CAPTON" printed circuit material. The coil period was 3 mm which yields the desired 30° SV-beam angle at 1.94 MHz in the HF-1 steel. This thin coil was bonded onto a high strength Lexan plastic backing plate (60 mils thick) that was shaped (using a casting fabrication technique) to conform to the radius of the projectile wall. Six alumina ceramic feet were embedded in this backing plastic and extended 10 mils from the surface to act as spacers and absorbed the abrasion as this unit rides lightly on the projectile. A set of Be-Cu springs were used to provide the contact force to the EMAT assembly. The EMAT assembly is shown in Fig. 38. Two EMATs, one to launch circumferential and one to launch longitudinal SV-waves are fabricated on each backing plate. The flexible CAPTON could be bent around the edge of the backing plate to allow electrical solder connections to be made at the rear of the assembly. The backing material is about 1" wide by 1-3/4" long. Mechanical tests conducted on the abrasion resistance of the ceramic wear buttons showed them to be very sturdy. Forty-eight hours of continuous rubbing on a projectile (at the force level

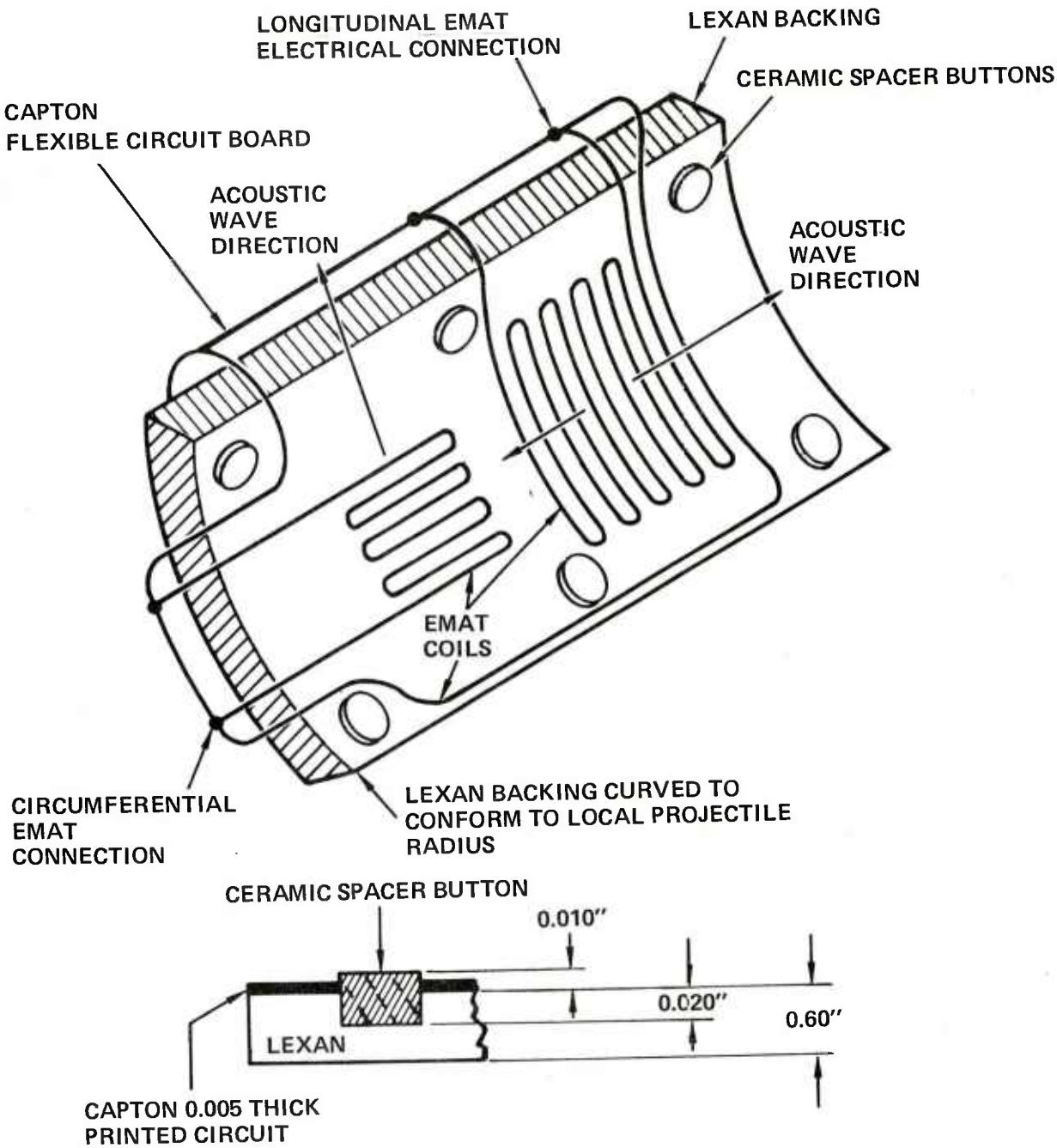

Fig. 38 a) Configuration of EMAT used to launch both longitudinal and circumferential acoustic waves on projectile. b) Cross-section of EMAT holder.

anticipated) showed no detectable wear. Estimated life for the buttons is 3000 hours of operation between replacement.

The exact dimensions of the wire widths and pad sizes used in the EMAT designs are shown in Fig. 39. All coils are 30 mils (by 2 mils thick) copper plated onto the CAPTON backing. The bourrelet region required that the EMAT that launched waves in the circumferential direction be tilted at about 10°degrees from the axis in order to achieve clean return signals. This was done by printing a new set of EMAT with the specified 10° tilt built-in.

The connection of the EMAT holder to the pole piece is shown in Fig. 40. The Be-Cu material is naturally springy and is positioned to lightly force the ceramic feet onto the projectile and keep the EMAT in close proximity to the shell. The spring guide structure has sufficient flexibility to allow it to "ride over" the wall variations that are within production tolerances of the M549 projectile. Note that shells grossly out of dimensional tolerance must be rejected before inspection by this scheme because too large a diameter projectile may crush the EMAT and ceramic supports into the pole pieces. Another potential problem exists with testing out-of-round projectiles having non-uniform cross sections. Here the excessive in and out motion tends to weaken the EMAT connections and eventually leads to open or short circuits at the EMAT. This problem can be overcome by strengthening the wire that wraps around the edge of the holder. Also a higher dimensional tolerance backing would be desirable because the LEXAN tends to flatten out in time.

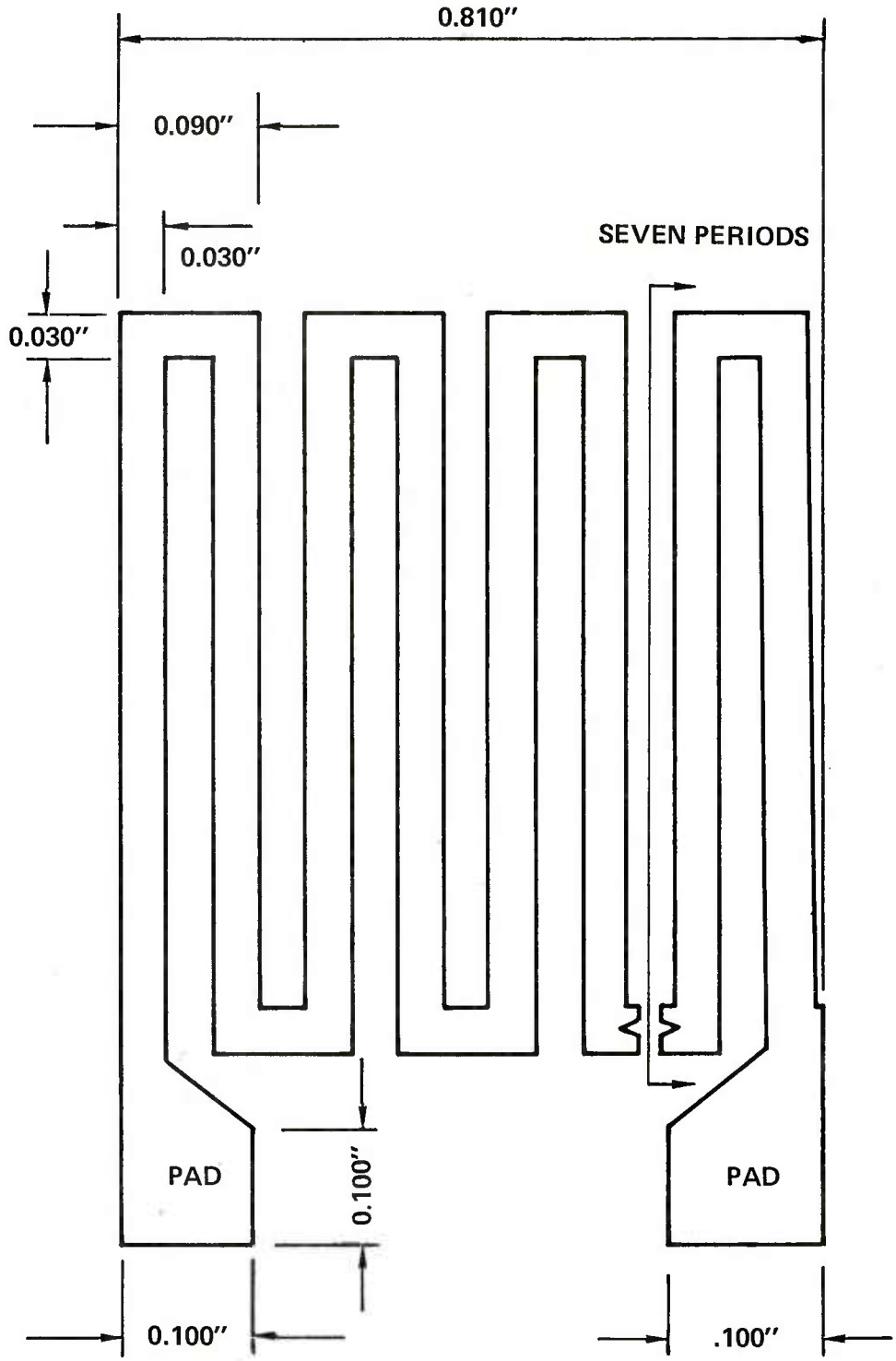

Fig. 39 EMAT meander coil dimensions.

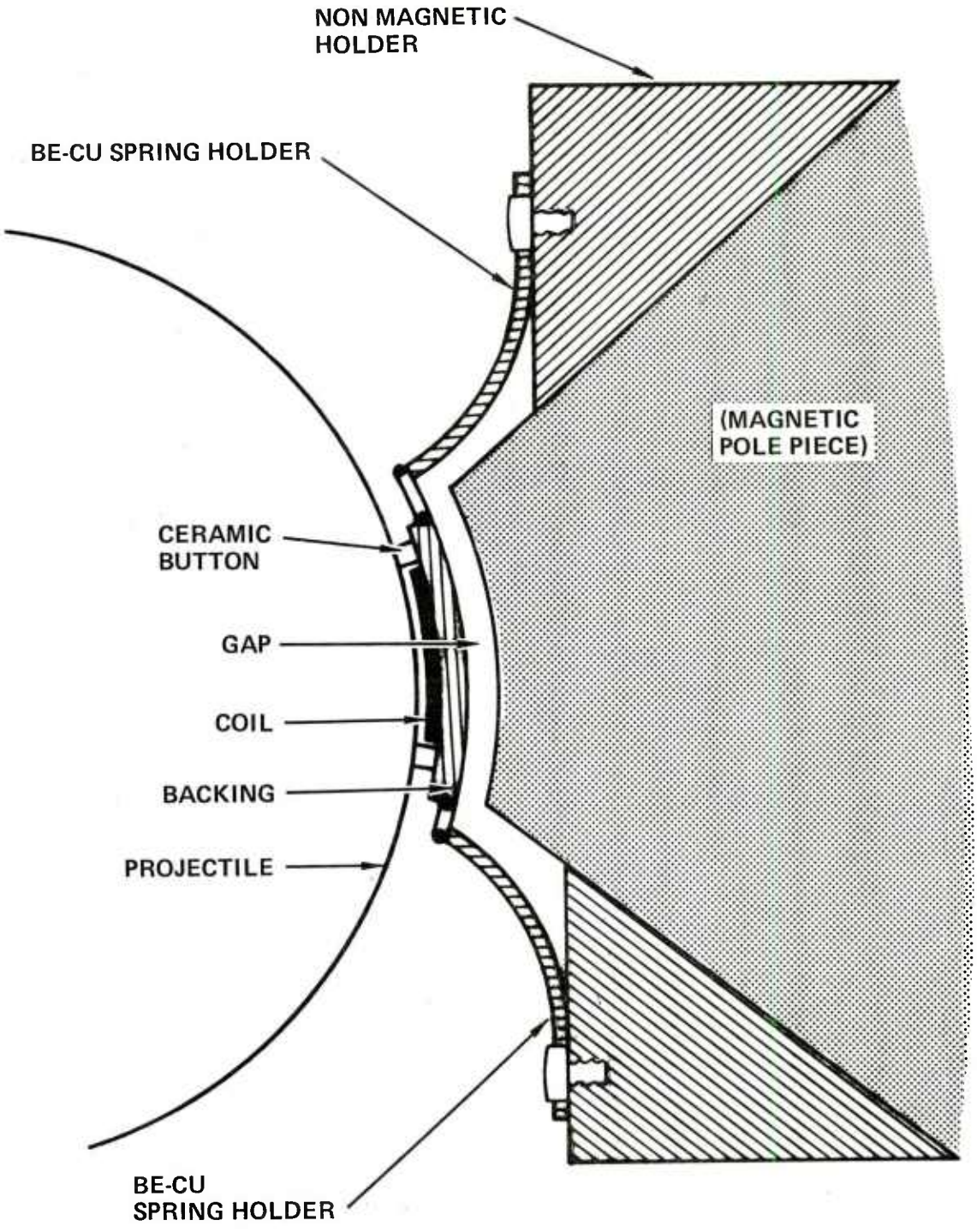

Fig. 40 Detail of EMAT holder and its position relative to projectile.

Figure 41 schematically illustrates the placement of the 22 EMAT pair array (11 on each pole piece) along the pole piece. The photograph of Fig. 42 shows the EMATs mounted on the test electromagnet structure and the associated spring mounting hardware. The assembly was used to verify that reliable inspection could be performed at each EMAT location before the entire unit was mounted into the inspection system. The 22 EMAT pairs yielded total coverage of the ogive and bourrelet region of the projectile.

IX. MECHANICAL PART HANDLING EQUIPMENT

The projectile handling equipment was built under subcontract by K.J. Law Engineering Inc. to Rockwell specifications. This equipment and operation is fully detailed in a companion publication to this final report entitled "Operation Manual for EMAT Ultrasonic Inspection System." Also, a complete set of engineering drawings for this handling equipment was delivered to ARRADCOM, Dover, NJ, under separate transmittal. Hence this section will only briefly describe the equipment and its operation.

The part handling apparatus is composed of three units. The first is a large mechanical station (Fig. 43) in which the electromagnet, pole pieces and EMATs are housed. The electromagnet assembly is mounted with the poles facing downward, tilted at 27° angle to accommodate the shell and hold the EMATs at the optimum angle (see Fig. 44). The projectile is elevated from its "load" position to its "inspection" position for operation. There is a large hydraulic bed that first clamps the two ends of the projectile then raises it

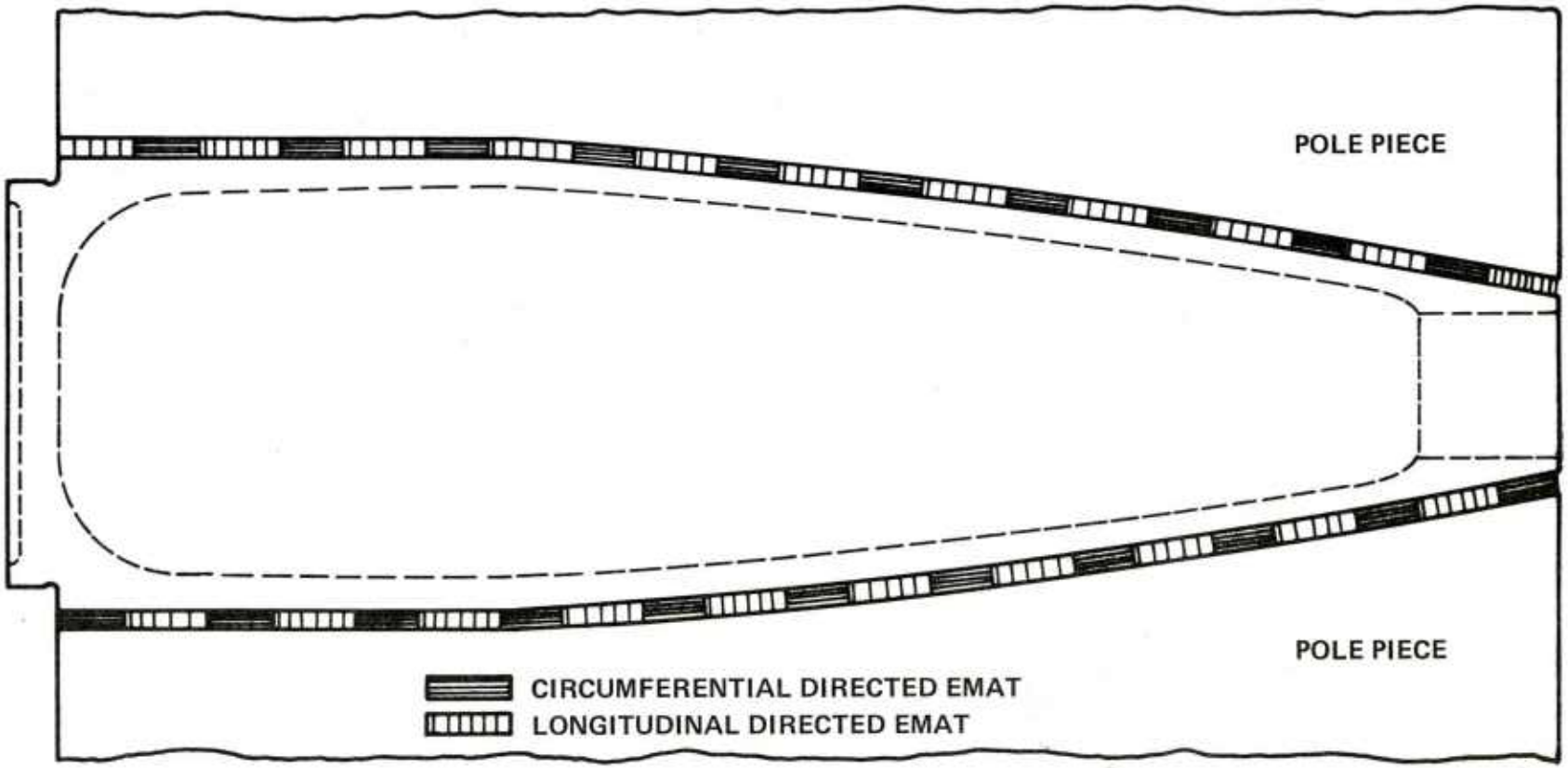

Fig. 41 EMAT placement about projectile to achieve full coverage.

SC80-9471

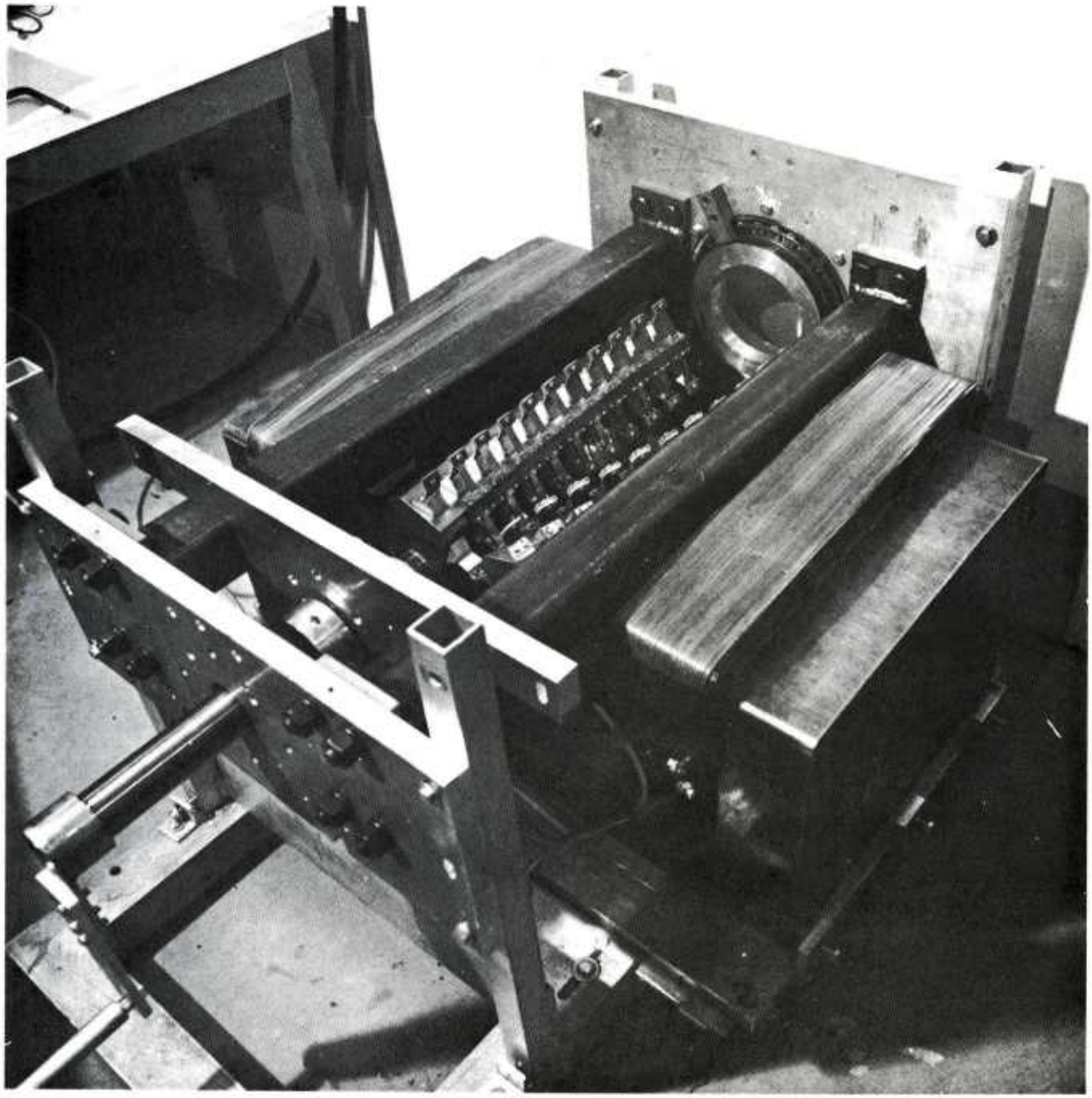

Fig. 42 Position of 22 EMAT array installed on electromagnet.

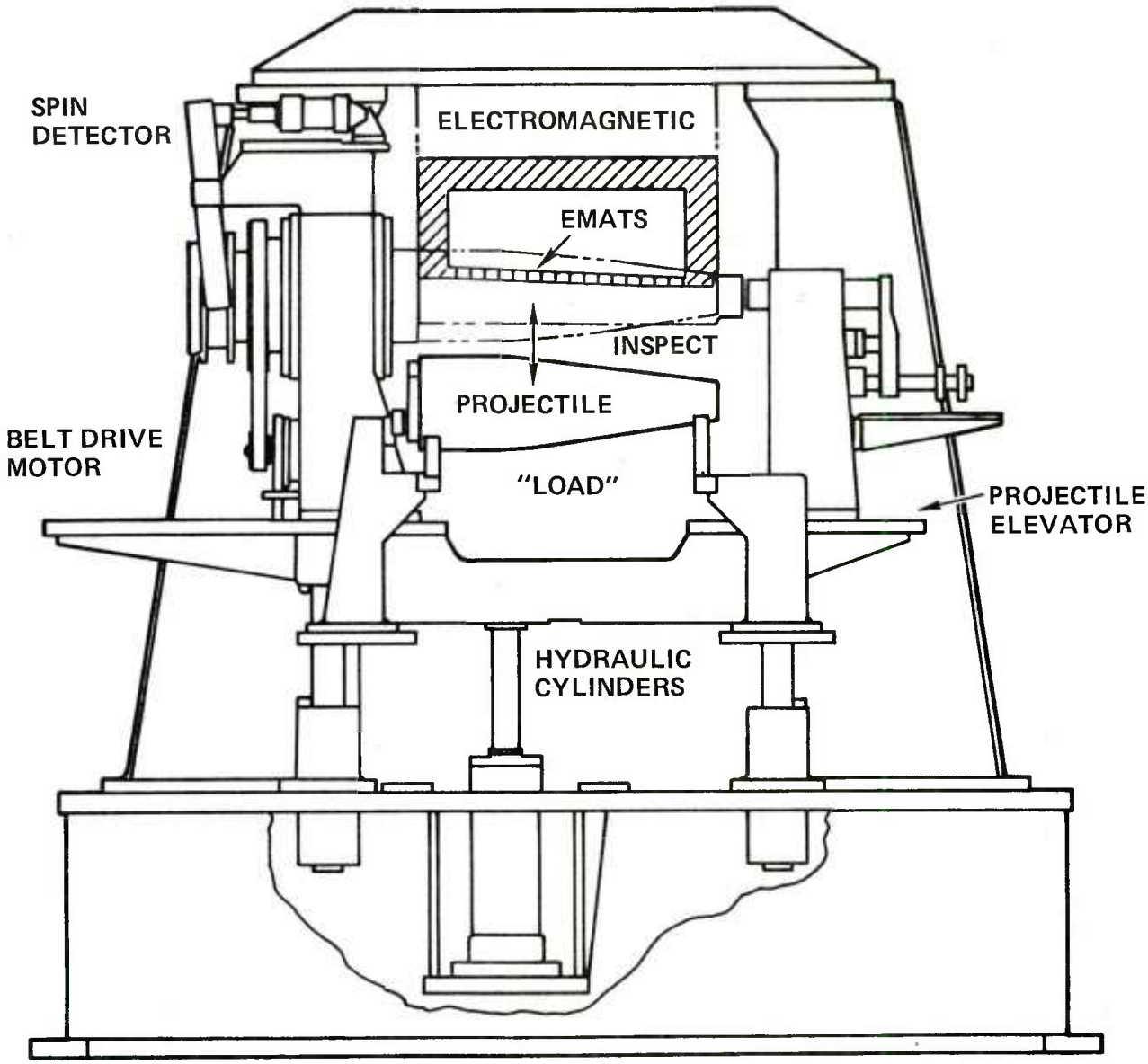

Fig. 43 Mechanical part handling apparatus (cross-section).

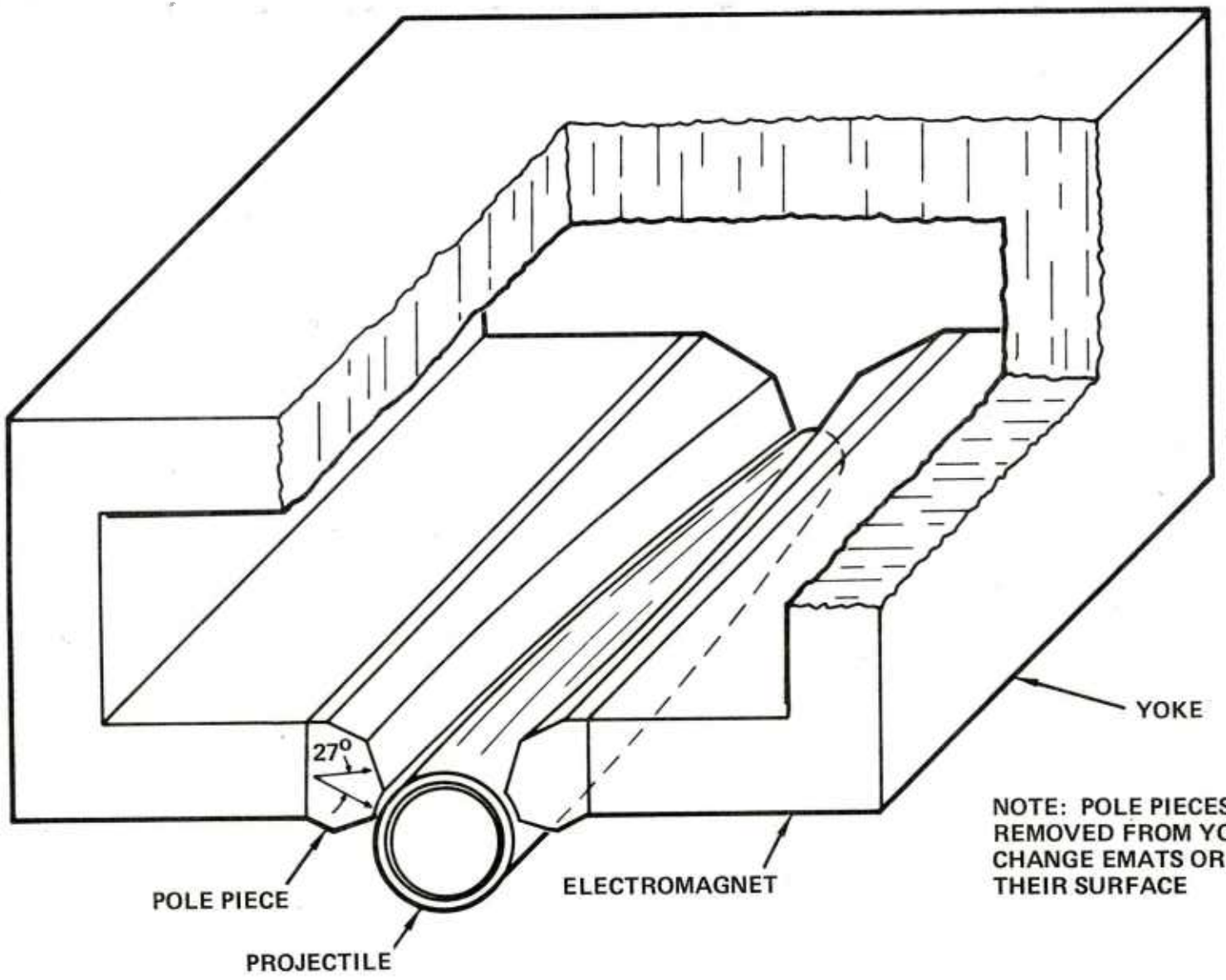

Fig. 44 Cutaway drawing of detail of electromagnet, tilted pole piece and projectile as configured in the final inspection apparatus.

into precise alignment with the EMAT transducer array holding it to 3/32" gap on either side. There are positive stops (plus adjustments) on each mechanical motion that is accomplished. The same hydraulic motor used to lift the projectile is used to rotate the shell while inspection is proceeding. The hydraulic motor, the second unit, is located behind the main station. The third cabinet contains all of the electrical switching and power distribution for the machinery.

The overall equipment layout is illustrated in Fig. 45, showing the part handler, the hydraulic motor, the electronics control cabinet and the Rockwell computer control unit (which will be described in the next section). Inspection can be accomplished either in a step-by-step manual mode using the control station on the front of the part handling unit or automatically from the Rockwell computer control unit.

A brief summary of the manual operation sequence is given below:

1. Manually load projectile onto carriage. Push carriage fully into machine until it locks in place.

2. Start hydraulic motor, clamp projectile ends and raise into inspection position. Energize electromagnet and bring current to desired level.

3. Rotate projectile at desired rate (40 rpm maximum) and perform EMAT inspection (i.e., each EMAT is fired as many times as necessary to yield complete coverage).

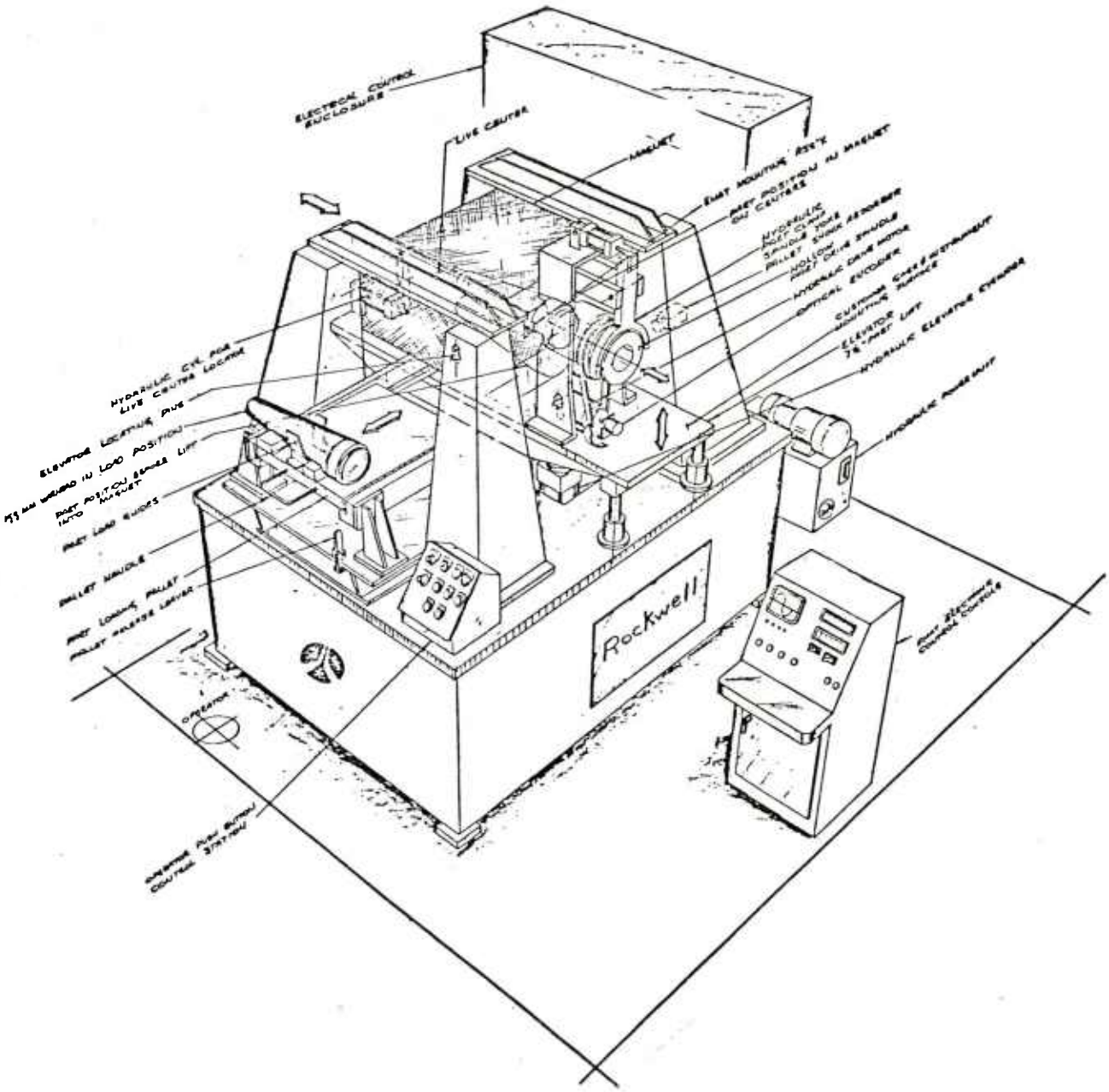

Fig. 45 Schematic layout of projectile inspection system.

4. Decrease electromagnet current, stop rotation, and lower shell from inspection to load position.

5. Unclamp projectile, unlock carriage, and withdraw projectile.

Two important points should be noted: A) The above process effectively demagnetizes the projectile as it is being removed from the electromagnet to the point where a paper clip will not be attracted to the surface after completion. Hence a separate degauss station once considered to be needed is not required; B) The part handling equipment is design to accept the retrofit of a "walking-beam" automatic load system. Thus if at some future date this machine is put into production line inspection, the automatic load-unload feature can be added to yield a totally automated system.

X. DIGITAL AND MICROPROCESSORS SUBSYSTEM OPERATION

This section describes the electronics control data analysis and display circuits (hardware) fabricated to interface to and control both the EMATS as well as the part handler. The corresponding software development and details of programming are fully explained in the companion publication, the system operation manual. A block diagram of the microprocessor control subsystem is shown in Fig. 46. The "Central Processing Unit" is based on the Motorola M6800 microprocessor and can be considered the "brain" of the system which initiates and coordinates all inspection activities. The CPU is completely

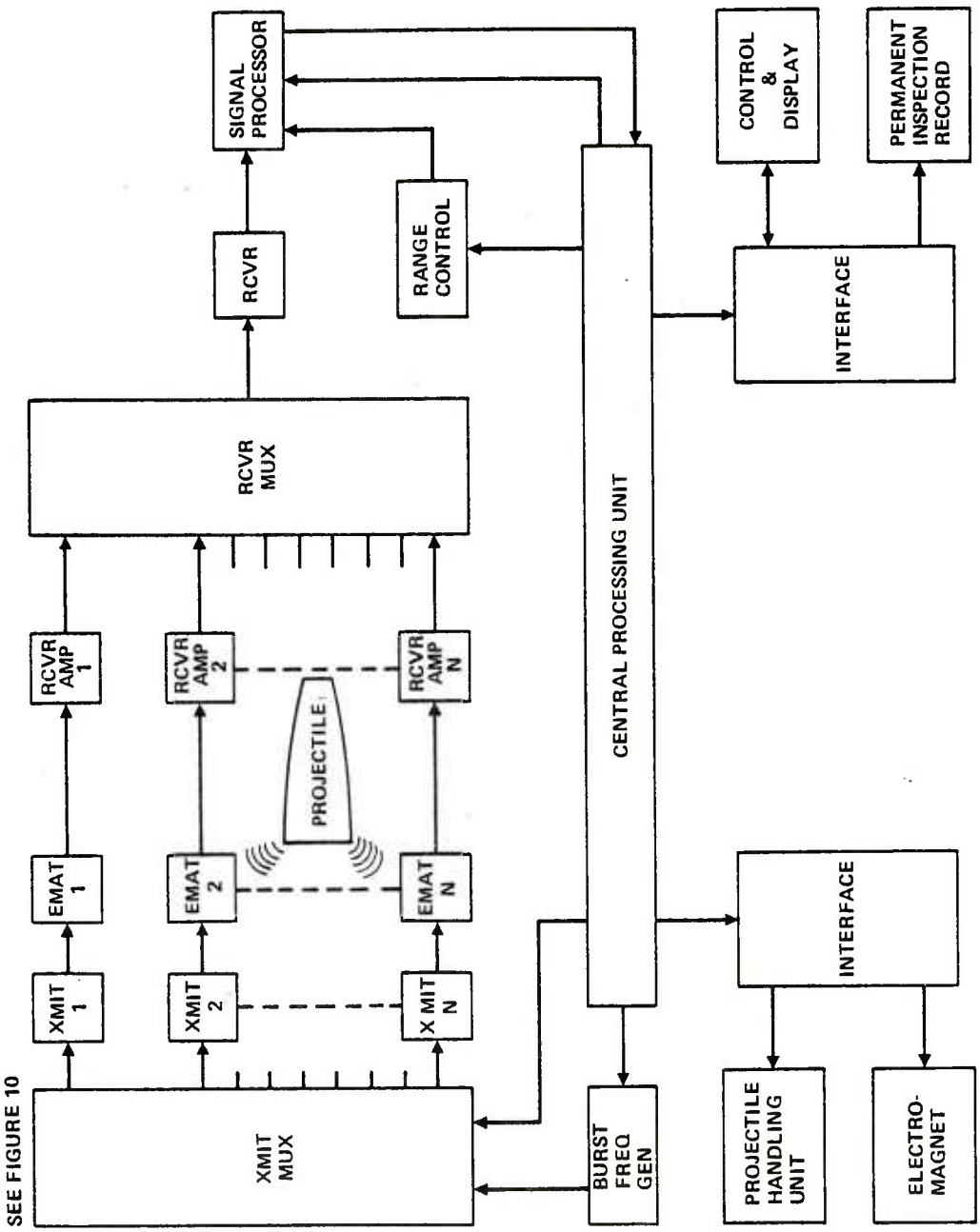

Fig. 46 Block diagram of projectile inspection control microprocessor system.

interfaced with the projectile handler (to determine its status and command its operation), the electromagnet (to energize or turn off), the transmitters/receivers and signal processing units (to initiate and coordinate inspection), a shaft encoder (to determine projectile position) and displays and keyboard (for information output or instruction input).

When the part handling unit indicates that a projectile is in position, the CPU initiates the test procedure for that projectile. First, an address is applied to the transmitter multiplexer circuit which selects the avenue through which the burst generator's output will be applied to a specific transmitter (XMIT N). At the same time, the receiver multiplexer selects the receiver associated with that transmitter and applies its output to the receiver (RCVR). At the appropriate time, the burst generator is fired and the signal processor is gated "ON" by the range control circuit. Any received signal is amplified, sampled, and sent to the CPU for processing.

The exact technique for digitizing the analog acoustic return signal is of interest. The method is illustrated in Fig. 47 where (a) shows the preamplified acoustic RF return signal which in (b) has been range gated, amplified and envelope detected. Figure 47 (d) shows the signal after it has passed through a peak sample and hold circuit and a reset operation. While the signal level is held at its maximum level it is sampled and digitized into one of 256 possible levels by an A/D converter. This magnitude is associated with the amplitude of the acoustic reflection. The location of the flaw is determined by knowing which EMAT was operated and the relative rotation of the projectile (using the shaft encoder signal). All of this data is stored and

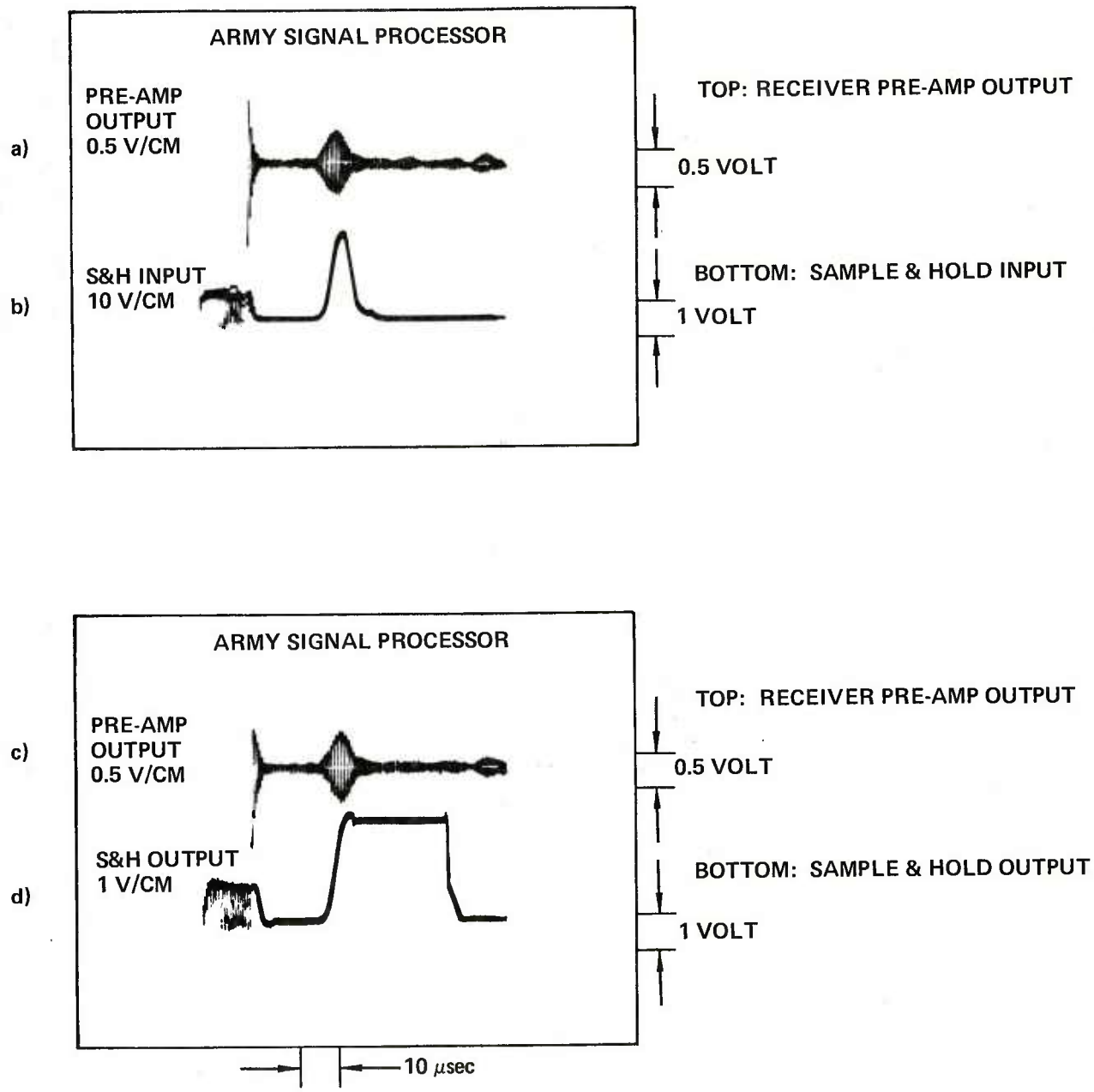

Fig. 47 Digitization technique for acoustic return signals.

can be printed out as a "map" of flaw magnitudes and locations. Whether a flaw is on the OD or ID is determined by moving the range gate between the two expected times of arrival and seeing which resolution cell (2 bounce or 3 bounce) contains the flaw signal. A plastic sleeve (divided into 1" square areas) fits over the projectile to identify the physical flaw location from the code so that destructive flaw verification can be accomplished if desired.

Figure 48 shows a more detailed microprocessor control block diagram. All elements or blocks to the left of the address, control and data buffers are housed in the main CPU enclosure and are tied directly to its buss. The keyboard for control is a hexidecimal (base 16) keypad located on the control panel as is the Datel printer. It is through these devices that the operator communicates with the system. The read-only-memory (ROM) contains the program or sequence of instructions which cause the MPU to execute the various required tasks. The random-access-memory (RAM) is the MPU's "Scratch Pad" and stores data for subsequent printout. The critical acoustic signal processing elements are controlled and operated as follows. The I/O interface block connects the MPU buss to the address, control, data, buffer (ACDB) block housed in a separate chassis, as are the remaining circuits. In conjunction with the I/O interface block, the ACDB buffers and then decodes the addresses of the various components in the system. Each slot in the I/O cabinet is associated with a unique address. When the MPU issues an address, the ACDB selects the appropriate slot and the circuit in that slot comes to life.

Referring to Fig. 48 when the MPU selects a transmitter/receiver pair, that address is latched into the address latch circuit (AL). "Latched"

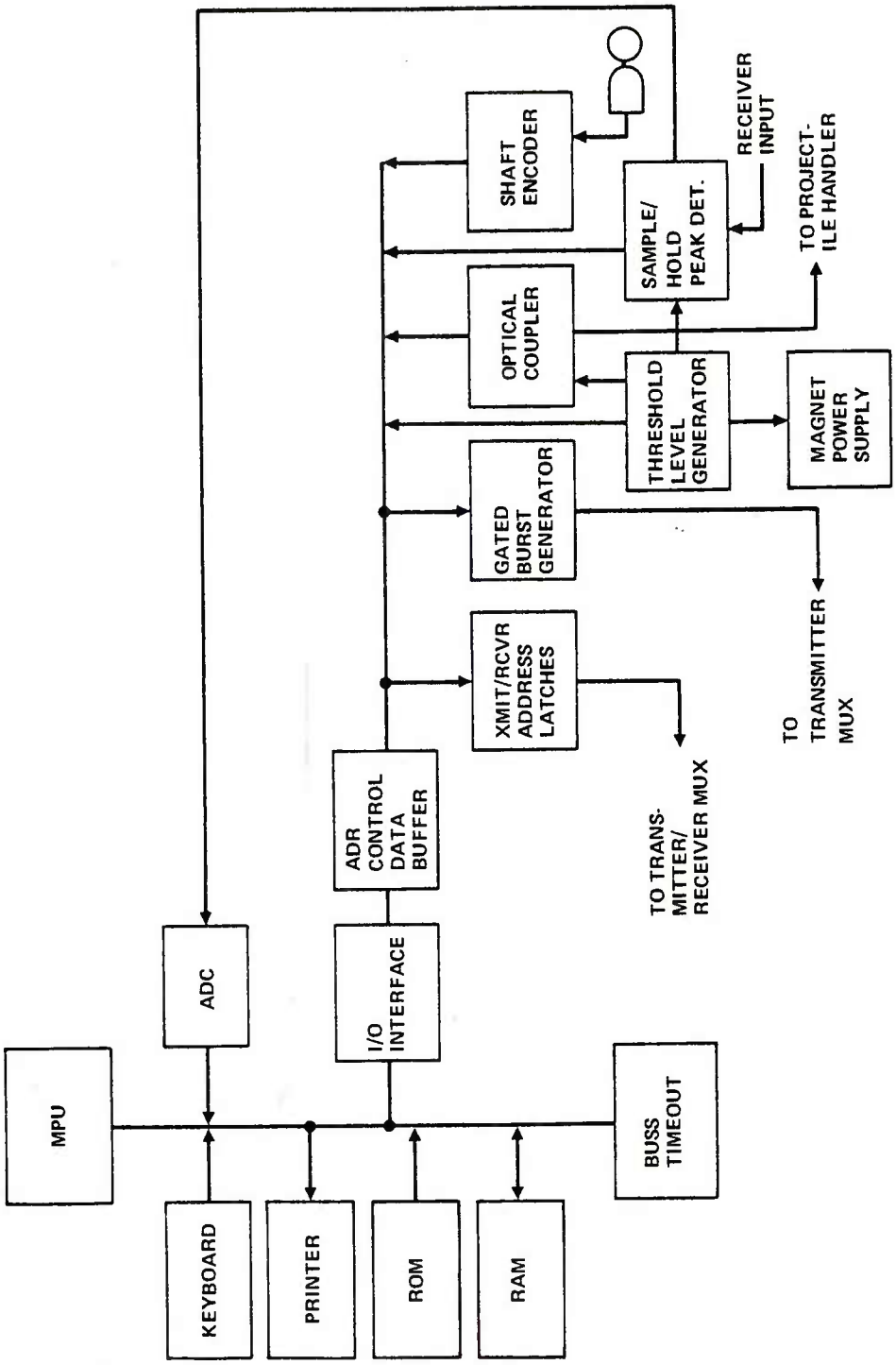

Fig. 48 System block diagram.

can be interpreted to mean that the input signal can go away, while the output retains the value which was entered. This allows the MPU to address other devices while the address latch remembers which transmitter/receiver pair was selected.

The shaft encoder receives angular data generated by the optical encoder wheel attached to the projectile's axis. Using this angular information and the physical position of the EMAT that was fired, the location of any flaw may be ascertained.

The MPU waits for the proper angular location and, upon its detection, fires the gated burst generator (GBG). The GBG can be programmed to select one of two pre-determined frequencies, and from one to sixteen cycles per burst. The circuit is designed in such a way as to give the prescribed number of complete cycles. This is important in order to keep unwanted harmonics to a minimum.

After the burst generator has been fired, the ultrasonic wave propagates through the material and, if any reflections occur, their presence will be sensed at the EMAT and, ultimately, the receiver. At the time of EMAT selection by the address latches, a threshold value associated with that particular EMAT was used to establish a threshold, below which a received signal would not be detected. This value is unique to every EMAT/Receiver and is established during calibration. With every EMAT/Receiver selection during the inspection process, its unique threshold value is issued by the MPU to establish this sensitivity point. It is the function of the threshold level gen-

erator to supply this voltage to the sample/hold peak detector. Data supplied by the MPU is applied to an 8-bit digital-to-analog converter (DAC). An operational amplifier is adjusted such that it scales the DAC's output from 0 to 2.5 volts. The resolution of the circuit is approximately ten millivolts (.010 volt), since 2 to the 8th power is 256.

A separate output of the threshold generator is applied to voltage comparator of the sample hold and range gate. If the analog signal input exceeds the threshold value, the MPU is notified and a flaw has been detected. The time at which the signal arrived is detected by the signal slicer circuitry. A schematic timing diagram for the ID vs OD flaw detection is given in Fig. 49. The range gate is set to turn-on the EMAT receiver (b) at the time that return signals from OD or ID flaws (a) would be expected. The resulting receiver output (c) is applied to the peak sample and hold which gives the output indicated in (d). The signal slicer selects first one then the other time slots and feeds it to a flip-flop circuit. If a peak detector output is present the corresponding flip-flop will be tripped and will be indicative of the presence of a flaw at the OD or ID locations. This information is read by the MPU and stored for readout. A block diagram of this flaw "mapping" circuit is given in Fig. 50. Table 3 summarizes the type of data printed out by the computer after a mapping operation.

All communications with the projectile moving device is routed through the optical couplers. These devices consist of light emitting diodes and photosensitive triac switches. Isolation is on the order of 5000 volts. The projectile mover notifies the MPU that a particular position has been

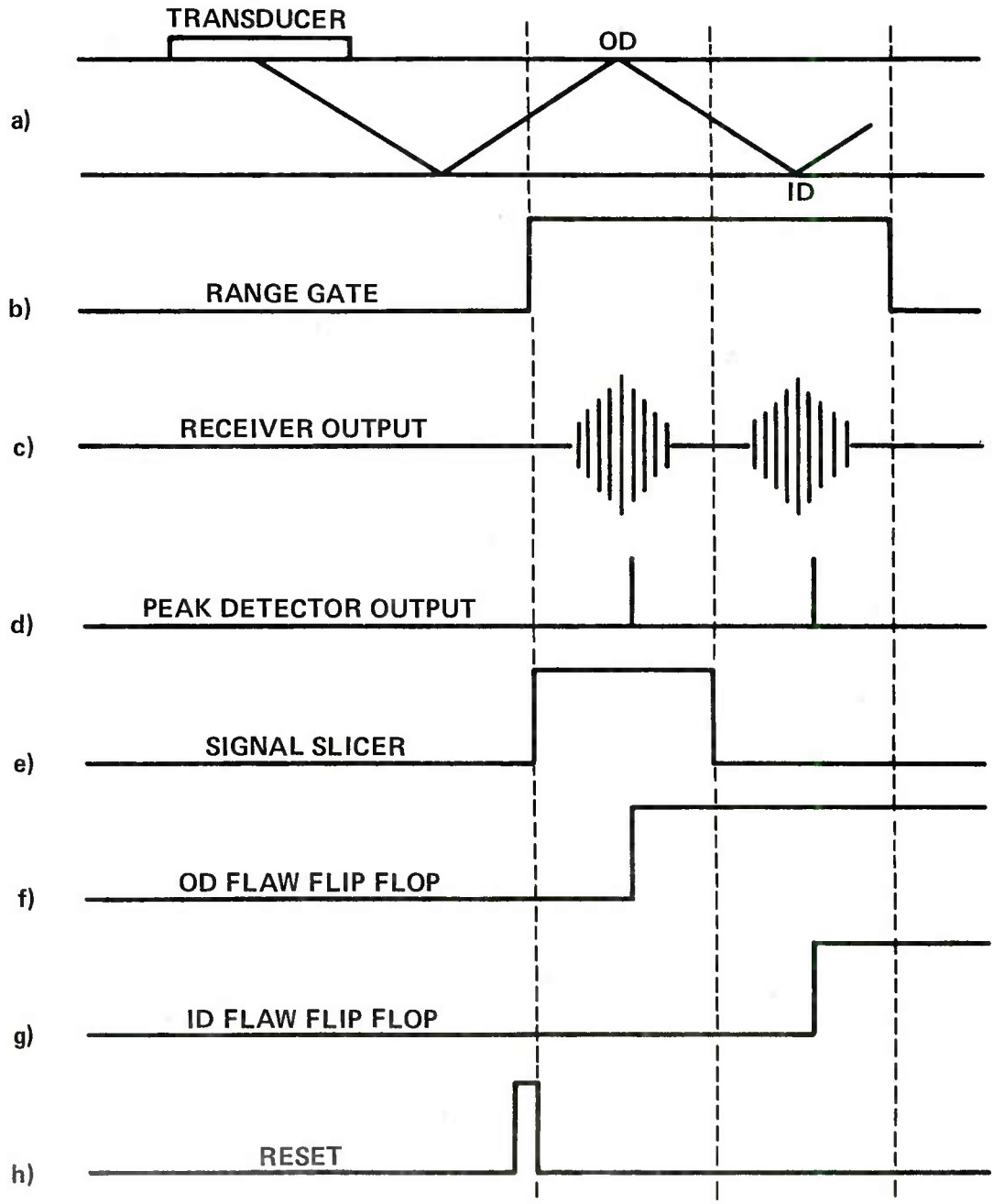

Fig. 49 Timing sequence diagram for classification of echo into OD or ID flaws.

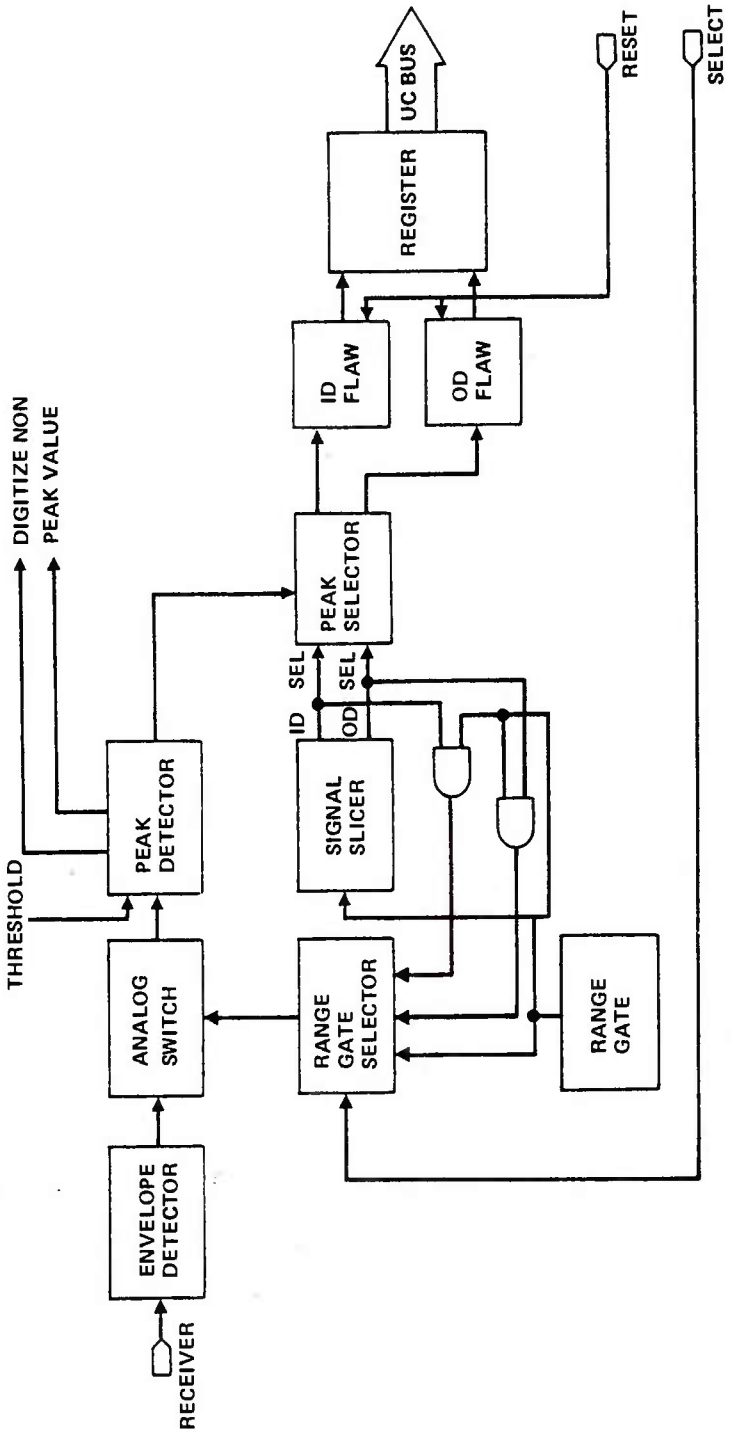

Fig. 50 Projectile flaw mapping circuit for OD and ID location.

attained through switch closures and discrete voltage levels (120 VAC). These are routed through the optical couplers to the MPU. The MPU actuates the projectile mover in a reverse manner.

This essentially summarizes the digital hardware circuitry. The reader is directed to the operations manual for further detail on software development or system programming.

The microprocessor and digital circuits, optical isolators, key board, print out unit and display lights are all integrated in the central control unit. The front panel input-outputs are broken into five sections: (1) keyboard (16 pad hexidecimal)

Table 3

Simulated Flaw Output Data (Print Out from Computer)

EMAT INSPECTION SYSTEM MAP

FLAW#	LOCATION	GRID COORDINATE	MAGNITUDE
1	OD	F - 2	2.2 T
2	OD	F - 3	2.3 T
3	ID	A - 10	1.2 T
4	OD	C - 1	5.1 T
5	ID	D - 8	3.2 T
6	ID	E - 8	3.4 T

Note: The #1 and #2 indications show an OD flaw of size about 2.2 times the threshold level that is large enough to fill F - 2 and F - 3 cells (circumferentially). Flaws #3 and #4 are isolated with #3 being barely over threshold while #4 is very serious. The #5 and #6 flaws are likely joined on the projectile interior and run longitudinally.

The flaw coordinate grid is lettered A through T to cover 20 1" long sections longitudinally down the projectile and numbered 1 through 19 (starting at an indicated reference line) circumferentially around the projectile.

(2) Datel hardcopy printer (3) start-reset buttons for automatic system operation (4) red "flaw" and green "no flaw" indicator lights (the lighting of the red light also sounds an audible alarm) and (5) a series of system status indicator lights. These lights tell if the 110 and 220 volt power is properly applied. If the MPU is ready, it is indicated by a light as well as if there is a CPU failure. Between each projectile inspection there is a self test algorithm that is sequenced to make sure all transmitters/receivers and EMAT are properly functioning. If any problem is detected it is indicated on the front panel lights and the projectile inspection sequence will not be initiated. If all subsystems are operating properly, a system OK light is illuminated and test can proceed. All of these self tests occur in a matter of a few seconds and do not appreciably effect the speed of inspection. It is believed that their inclusion was extremely important in order to assure the equipment is functioning satisfactorily before inspection decisions are made. This test methodology is directed at achieving the very highest (1 part in 10^6) reliability goal of inspection and thus minimize false acceptances. Only when the test equipment itself is proved to be working accurately can accurate and high confidence inspections be accomplished. This level of sophistication is believed necessary to produce the advanced military projectile inspection unit that is fail safe and capable of the highest quality inspection.

XI. OVERALL SYSTEM PERFORMANCE

This section summarizes the technical inspection results obtained using the EMAT inspection system in its final configuration to analyze both "standard" flawed projectiles and several other projectiles.

Figure 51 shows a photograph of the final system being loaded with a projectile for inspection. The part handling control actuators and microprocessor control console are being programmed by the operator to perform the desired inspection operation. The coils of the electromagnet are observable at the top center of the apparatus. Directly behind the unit is the hydraulic motor with hard plumbed connections to the main assembly. Not observable in this photograph are the power distribution console and the two military type card cages that reside on top of the unit. The card cages hold the 44 individual transmitter/receiver cards which interface to the EMAT ultrasonic transducers. Each T/R card is individually connected to one of the respective longitudinal or circumferentially oriented EMATs by a miniature coaxial cable. The T/R cards are easily replaceable so that if an electrical malfunction should occur, the appropriate EMAT electronics can be substituted in very rapid order. Five back-up (spare) T/R cards were supplied with the delivered unit along with duplicates of all important and unique system elements (including the microprocessor and memory boards and several space EMAT assemblies).

The design concepts for reliable system operation can be seen in several areas. First, the basic part handling apparatus is very sturdily built weighing more than 14,000 lbs and built of heavy gauge steel. The hydraulics

SC80-9473

Fig. 51 Photograph of fully assembled EMAT inspection system during projectile inspection.

and moving parts are all constructed to yield extended operation before maintainance. Second, the electrical power supplies for the electromagnet, RF electronics, and digital circuits are all capable of considerable more current than they will have to deliver in normal operation. For example, only 40 amps out of a possible 100 amps is required by the electromagnet to achieve the desired magnetic field. The electromagnet coils themselves were redesigned to operate continuously at 50 amps without overheating. However, in normal operation the current should reach only 40 amps for a 50% duty cycle. As stated previously, the RF and digital circuits are also operated considerably below their "rated" levels. All of the above steps were taken to try to achieve high reliability with little down time at high rates of inspection -- as is expected to be required in future production line operations.

Figure 52 shows the sequence of events that comprise a complete projectile inspection operation by the EMAT system. The time that each step requires at present is listed in the first column and a projected time is listed for inspection at a slightly more rapid rotational rate. The desired program goal of inspecting 1400 projectiles per month (one projectile every 44.6 sec of each 8 hr work day) is easily met by the system as it stands. However, analysis of the time spent in each step shows that the actual EMAT inspection requires only 10 sec and over half the time is consumed in energizing and de-energizing the electromagnet unit. If a different power supply could be used to more rapidly bring up the coil current or else a different mechanical support arrangement devised that could operate with the B-field left at its maximum level, then the projectile inspection times could be reduced to the 20 second range.

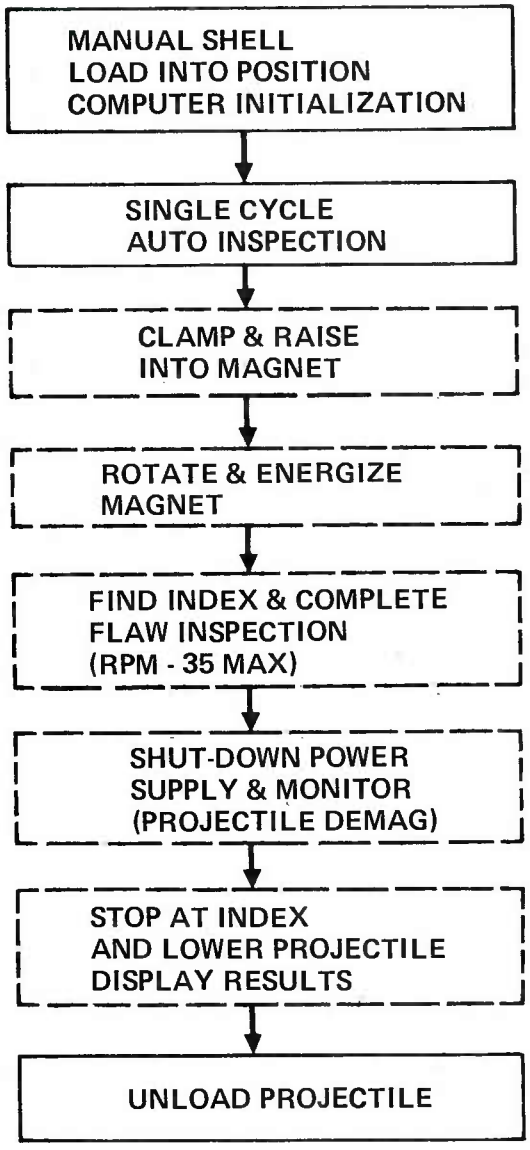

	CURRENT TIME	PROJECTED TIME
MANUAL SHELL LOAD INTO POSITION COMPUTER INITIALIZATION	N.A.	N.A.
SINGLE CYCLE AUTO INSPECTION		
CLAMP & RAISE INTO MAGNET	3 SEC.	3 SEC.
ROTATE & ENERGIZE MAGNET	12 SEC.	10 SEC.
FIND INDEX & COMPLETE FLAW INSPECTION (RPM - 35 MAX)	10.2 SEC.	8.5 SEC.
SHUT-DOWN POWER SUPPLY & MONITOR (PROJECTILE DEMAG)	10 SEC.	10 SEC.
STOP AT INDEX AND LOWER PROJECTILE DISPLAY RESULTS	3 SEC.	3 SEC.
UNLOAD PROJECTILE	N.A.	N.A.
	38 SEC.	34.5 SEC.

Fig. 52 Sequence and corresponding times required for projectile inspection.

It must be noted that the high B-field used puts considerable stress on the projectile (calculated to be 6000 lbs distributed over the shell surface) which necessitates precautions be taken in the design of the handling unit. The overall strength and rigidity of the clamping and lifting assemblies must be controlled or else undesirable deflections were found to occur which endanger the EMATs in the pole piece gaps.

The location on the projectile of the standard EDM notches is shown in Fig. 53. During the test, the RF outputs of each EMAT was disconnected from the computer and directly observed on an oscilloscope. The projectile was rotated while the inspection was carried out and the EMAT firing synchronized to the angle of projectile rotation. The 19 OD and ID longitudinally oriented flaws located in the projectiles ogive and bourrelet regions were detected with high reliability. The majority of the responses exhibited outstanding signal to noise ratio and were repeatably detected. As stated previously, the base flaws could not be detected by the EMATs located along the projectile sidewalls and a special surface wave EMAT approach is required (this was not implemented on the delivered system). The EMAT system was not tested on the circumferential standard flaws because the standard projectile was not available during the final weeks of the program. This flaw standard part arrived shortly after the equipment was sent to ARRADCOM so it was forwarded for inspection. It is anticipated that the circumferential flaws will be found with the same S/N ratio as achieved for the longitudinal ones. The description of flaw standards is given in Appendix D.

The set up and calibration methods for the system are as follows:

1) perform automatic system status check - lights indicate system O.K. to

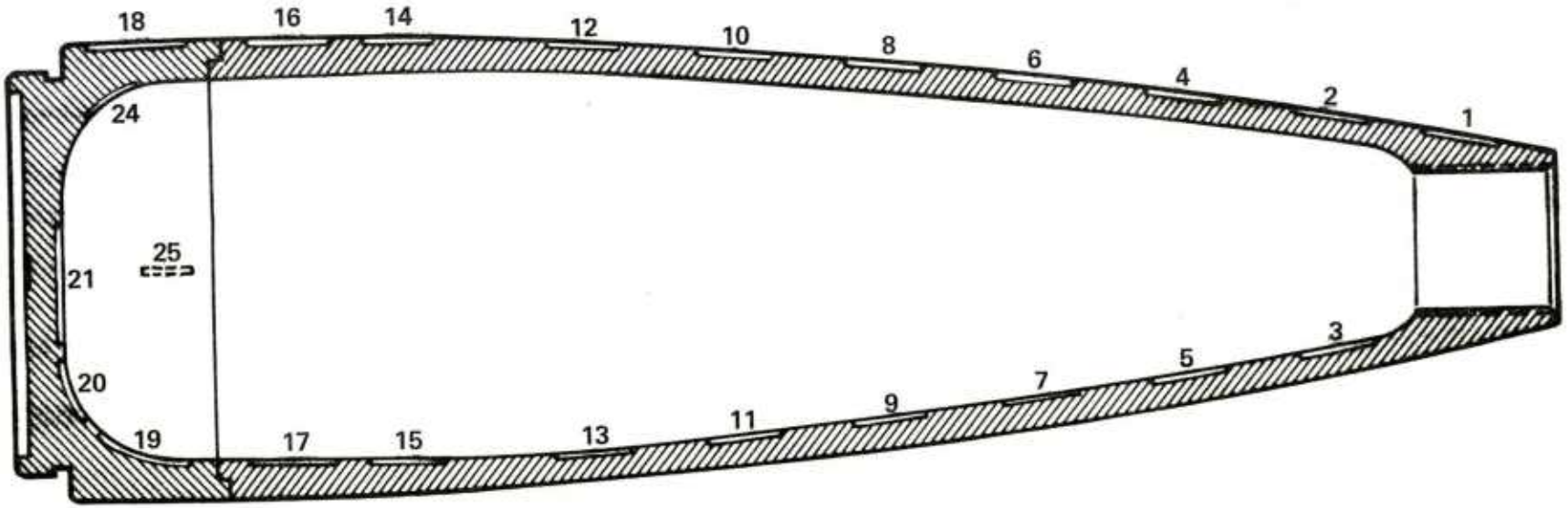

SC5186FR

Fig. 53 Location of standard EDM notches on projectile.

proceed, 2) insert standard flawed projectile and measure and record magnitude and locations of all flaws found, 3) scale the threshold levels to some fraction of the standard (the threshold can be set to "just detect" the standard or be as small as 1/256 times smaller). A trade-off exists between false alarms due to small ripples on the forged projectile surface - which can give a small acoustic reflection and too large thresholds that will only detect reflectors comparable to the standard flaw reflections. Once this calibration level is set it can be locked-in and can't be changed by an operator until a new calibration is performed. After calibration the equipment is ready to be used either manually or in the auto mode.

During the week period that the ARRADCOM engineering team was performing acceptance tests on the EMAT unit, a number of projectiles were tested. The standard projectile having 19 independent OD and ID flaws was always identified as being faulty by the automatic inspection. A projectile having only one EDM OD flaw was also consistently identified as being flawed. Several ultrasonically clean projectiles were also tested. After suitable calibration, all of these were classified as unflawed. Thus the EMAT inspection equipment performed with high reliability and consistent inspection quality during all inspection tests performed.

The contract specified the inspection of a run of 300 projectiles from the Norris Plant as a system demonstration and test verification. However, these projectiles were not sent to Rockwell during the duration of the program so that these tests will have to be postponed to be accomplished at ARRADCOM after the unit is set-up at that facility.

XII. CONCLUSIONS

Phase B of this program has been completed with the successful demonstration of a unique EMAT ultrasonic inspection system for the nondestructive evaluation of M549 RAP projectiles. This inspection apparatus has been subsequently delivered to the ARRADCOM facility in Dover, NJ, for installation and further testing.

The salient results that have been achieved are as follows:

- EMAT inspection of projectile ogive and bourrelet regions validated.
- System is capable of finding 0.020" deep by 1" long EDM notches in 0.400" thick projectile with 30 dB S/N ratio (comparable to conventional ultrasonic techniques).
- EMATs can be made to have uniformly high detection sensitivities to OD and ID flaws oriented either longitudinally or circumferentially to the projectile's axis. EMATs themselves are easily calibrated.
- Flaws can be located while projectile is rapidly moving (demonstrated at spin speeds up to 180 rpm).
- Flaw detection process takes 10.2 sec and total inspection time is less than 40 seconds which meets the program goal (14,000 inspections/month).
- Measurement and accept/reject decision process under complete microprocessor control which minimizes human interpretation and intervention.

- System is amenable to fully automated operation including final part accept/reject decision. A mapping mode can produce a hard copy output of flaw type, size, orientation and location for destructive test verification.
- Electronic and mechanical hardware designed for rugged and reliable operation. Software designed for flexibility and ease of use.

We believe that several unique technical contributions were made during the course of the EMAT system development. Virtually every subassembly fabricated (e.g., EMAT transducers electromagnet pole piece, transmitters/receivers electronics, digital signal processor and microprocessor control unit) has some novel design or employs an unusual fabrication technique. The several patent disclosures field on this project is evidence of the above claim.

The final proof of the EMAT technique (and technology) rests on successful demonstration of this first prototype EMAT system in a continuing laboratory or field inspection environment. The fact that it was capable of detecting simulated flaws (EDM notches) consistently in the laboratory must be verified and extended to a large enough population of "real" flaws to establish a track record for EMAT inspection. It is hoped that the promise of EMAT superiority -- for the next generation of ultrasonic projectile inspection -- will be established by continued reliable operation of this first field unit at ARRADCOM's facility.

REFERENCES

1. "A Model for the Electromagnet Generation of Ultrasonic Guided Waves in Ferromagnetic Metal Polycrystals," R. B. Thompson, IEEE Transactions on Sonics and Ultrasonics, Vol. SU-25, No. 1, Jan. 1978.

2. "Rapid Ultrasonic Inspection of Artillery Projectiles," M. W. Mahoney, Final Report, Contract DAAK-10-78-C-0490, Document No. SC5186.24FR, Aug. 1979.

3. "Periodic Magnetic Non-Contact Electromagnetic Acoustic Wave Transducer - Theory and Application," C. F. Vasile, R. B. Thompson, Proc. IEEE Ultrasonics Symposium, 1977.

4. "Rapid Inspection of Artillery Projectiles with Electromagnetic Transducers," C. M. Fortunko and R. B. Thompson, Proc. IEEE Ultrasonic Symposium, 1977.

5. "Inspection Criteria for the Projectile Warhead Component Based Upon Fracture Mechanics Methodology," J. H. Mulher, Mat. and Mfg. Tech. Division ARRADCOM, 1977.

APPENDIX A

TECHNICAL COMPARISON OF EMAT AND CONVENTIONAL ULTRASONIC NDT EQUIPMENT FOR INSPECTION OF ARTILLERY PROJECTILES

The primary principle of current NDT operational inspection philosophy developed by the Artillery/Tank Systems Division, Product Assurance Directorate (PAD), ARRADCOM, can be summarized as follows:

> DEVELOP AN INSPECTION PLAN THAT HAS THE HIGHEST RELIABILITY OF PREVENTING CRITICAL DEFECTS FROM REACHING THE STOCKPILE BY ELIMINATING HUMAN INTERPRETATION AND UTILIZING THE MOST EFFECTIVE STATE-OF-THE-ART INSPECTION TECHNIQUES.

From this statement, four criteria can be developed in order to evaluate and compare similar NDT techniques to determine which most closely satisfies the NDT inspection goals. The four criteria are:

1. Highest flaw detection sensitivity
2. Equipment must have high operational reliability
3. Equipment automated to eliminate human interpretation
4. Lowest cost per projectile inspection

A secondary principle of the same NDT operational philosophy can be stated as follows:

A QUANTITATIVE MEASUREMENT IS DESIRED AS THE BASIS FOR ESTABLISHING ACCEPT/REJECT CRITERIA WHICH PREVENT THE REJECTION OF PARTS CONTAINING NON-CRITICAL DEFECTS BUT REJECT ALL PARTS CONTAINING CRITICAL DEFECTS.

This statement leads to a fifth criteria on calibratability of the required inspection equipment, which can be stated as follows:

5. Equipment calibration reproducible. Standard flaws detected with uniform sensitivity in like region of projectile.

With these guidelines, this appendix seeks to define the unique capabilities of EMAT inspection systems for inspecting artillery/tank projectiles in a manufacturing environment as compared to conventional ultrasonic methods which require a coupling fluid or water bath to conduct sound between the transducer and the projectile under inspection.

Table A-1 Summary of EMAT Advantages Over Conventional Ultrasonics

EMAT System Characteristic	Description of Characteristic	Goal Addressed
1. Noncontacting Transducer	Ultrasonic energy directly coupled to projectile. Rapid inspection of EMAT promises to lower per-projectile inspection times from several minutes to ~15 sec. EMAT system compatible with assembly-line inspection via "walking beam" approach. No restrictive couplant fluid required.	Cost Detection Automation
2. Redundant Inspection Capability	High inspection speed. The manner in which ultrasonic energy is generated, coupled with the fact that EMATs inspect two sides of a projectile at once, yields redundant inspection. Every volume element inspected by sound beams of two perpendicular orientations.	Detection
3. Ultrasonic Beam Uniformity	Due to planar EMAT construction, no ultrasonic "hot spots" are formed as often happens with conventional transducers. Thus, EMATs give equal sensitivity to flaw at any position in the beam.	Detection Calibration
4. Beam Scanning	The angle that the EMAT acoustic beam enters the projectile can be varied so that detection is enhanced.	Detection
5. Capable of Acoustic Mode Selection	Because of its unique coupling characteristics, EMATs can inspect with either longitudinal or SV or SH polarized shear acoustic waves. This versatility is difficult to achieve using fluid coupled conventional ultrasonic transducers, since shear waves cannot be supported by a liquid.	Detection

Table A-1 (Continued)

EMAT System Characteristic	Description of Characteristic	Goal Addressed
6. EMAT Mechanically Less Complex	No complex transducer motion is needed with EMATs to get complete projectile coverage. Conventional transducers must be scanned to cover projectile.	Detection Reliability Automation Cost
7. Sturdy Transducers	Conventional piezoelectric transducers are much more fragile because they are composed of a ceramic material that easily fractures. Replacement cost of an EMAT transducer is correspondingly less than a piezo-transducer.	Reliability Cost
8. Insensitive to Surface Contamination or Temperature	Due to noncontact feature, EMAT can inspect surface with contamination (oil or other matter) on surface; or could be at elevated temperature. However, surface must be free from large particulate matter for EMATs operation.	Detection Calibration
9. Electrically Identical Transducer	Since EMAT efficiency only depends on field strength and the separation of coil from the part, all all transducers are identical. Conventional piezoelectric transducers exhibit large variations between supposedly identical units because the ceramic material is nonuniform.	Calibration Reliability Detection Automation
10. High Sensitivity to Small Flaws	Due to noncontact nature and direct electromagnetic coupling, high sensitivity is achieved for small flaws. The sensitivity is essentially equal to or superior to conventional ultrasonic techniques, with both being limited by "clutter" signals' (superior when surface contributes significantly to clutter).	Detection

Table A-1 (Continued)

EMAT System Characteristic	Description of Characteristic	Goal Addressed
11. Capable of Self-Test	Under microprocessor control, EMAT units can be self-tested to assure reliable operation. Components tested include magnet assembly, EMAT, RF electronics, and computer system. Status is verified before inspection can begin.	Automation Reliability Detection Calibration Cost

EMAT technology does however possess some drawbacks when compared to more common piezoelectric technology.

Table A-2 Summary of EMAT Disadvantages Compared to Conventional Ultrasonic

EMAT System Characteristic	Description of Characteristic	Goal Addressed
1. New Technology	Although EMATs have been under study in the research community for over 8 years, this effort is one of the first to develop a viable EMAT system for routine use. Further engineering advances are required to ruggedize EMATs for field applications.	Reliability
2. High Magnetic Fields Required	EMAT inspection systems that must sense very small flaws require extremely high magnetic fields to achieve adequate S/N ratios. This in turn means large, heavy (costly) electromagnets must be used and massive support structures required. This increases the cost to build such units.	Cost

Table A-2 (Continued)

EMAT System Characteristic	Description of Characteristic	Goal Addressed
3. Less Efficient Transduction	The EMAT must be driven by higher power transmitters than conventional units to achieve similar S/N ratios. However, solid state electronic transmitter units have been developed which can produce sufficient power to yield comparable ultrasonic detectability in EMATs and piezoelectrics.	Cost

Even with the above disadvantages clearly in mind, it is believed that EMAT inspection more fully meets the product assurance goals set forth than conventional ultrasonics. The noncontact nature and unique acoustic beam generation characteristics allow high speed operation with more opportunity to detect critical flaws in the projectile. Mechanical simplicity should lead to a higher reliability while automated measurement will decrease human interpretation.

APPENDIX B

MAGNET DESIGN CODE

This appendix summarizes the efforts by a subcontractor to help develop the necessary computer software to analyse the magnetic field profile that enters the projectile. The goal was to aid in the final design of the magnetic pole-piece assembly for optimally coupling energy into the projectile from an adjacent EMAT coil.

25 July 1979

Prepared By: Falcon Research and Development Co.
2350 Alamo Ave., SE
Albuquerque, NM 87106

TABLE OF CONTENTS

INTRODUCTION

The goal of this work was to develop a two-dimensional finite difference computer code capable of solving Laplace's equation in 2-dimensional cylindrical geometry for arbitrary boundary conditions.

Previous memos released by Falcon Research and Development to Rockwell personnel have outlined the methods and capabilities of the code and the goals of this work. Changes have been made during the course of this work, and therefore, some of this material will be included here again for completeness. A User's Manual for the computer code, in the form of this report is also being furnished.

In addition, a polar contour plot package in support of this work for graphical display of the code output has been developed. Also included in this report are two analytic test cases in verification of the accuracy of this code.

BASIC EQUATIONS AND IDEAS

The code developed, henceforth called LAPLACE, solves Laplace's equation in cylindrical coordinates with arbitrary boundary conditions. In order to attain the required resolution in the mesh, a non-uniform grid spacing in both the r, and θ directions was implemented.

Laplace's equation in cylindrical coordinates is given by

$$\nabla^2 \psi = 0$$

$$\Rightarrow \frac{1}{r} \frac{\partial}{\partial r} \left(r \frac{\partial \psi}{\partial r} \right) + \frac{1}{r^2} \frac{\partial^2 \psi}{\partial \theta^2} = 0 \qquad (1)$$

An explicit second order difference technique (truncation error $\propto \psi'''$ and $\varepsilon \Rightarrow \frac{1}{4} \varepsilon$ when $\Delta h \rightarrow \Delta h/2$) was used to arrive at

$$\frac{1}{r_j (r_{j+1/2} - r_{j-1/2})} \left[r_{j+1/2} \frac{(\psi_{j+1,k} - \psi_{j,k})}{(r_{j+1} - r_j)} - r_{j-1/2} \frac{(\psi_{j,k} - \psi_{j-1,k})}{(r_j - r_{j-1})} \right] + \frac{1}{r_j^2} \frac{1}{(\theta_{k+1/2} - \theta_{k-1/2})} \left[\frac{(\psi_{j,k+1} - \psi_{j,k})}{(\theta_{k+1} - \theta_k)} - \frac{(\psi_{j,k} - \psi_{j,k-1})}{(\theta_k - \theta_{k-1})} \right] = 0$$

where the subscripts refer to the r, θ mesh locations as depicted in Fig. 1.

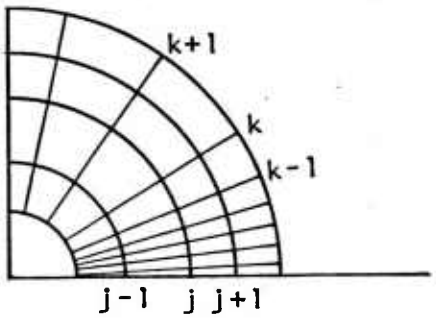

Fig. 1 Mesh geometry.

The ± 1/2 subscripts are defined as

$$r_{j\pm1/2} = \frac{(r_j + r_{j\pm1})}{2} \tag{3}$$

and similarly for θ.

The difference equation (2) is exactly second order for uniform mesh, however, this mesh is defined as follows:

$$r_j = r_{j-1} + \Delta r_o \ \delta^{j-1}$$

$$\theta_k = \theta_{k-1} + \Delta\theta_o \ \lambda^{k-1} \tag{4}$$

where r_1, and θ_1 are specified as well as the initial increment Δr_0 and $\Delta\theta_0$. Depending on the values of (δ,λ), Eq. (4) will introduce a mesh expansion (>1) or contraction (<1) which in turn will mean the difference equations will not be centered, hence no longer second order. If the factors (δ,λ) are close to one, the error introduced to the difference equation is small and no correction need be made. If this factor is larger, the error grows proportionally and the method becomes first order.

As originally proposed, a first order correction term was to be used to re-center the derivatives. However, this actually increases the relative error in the approximation to the Laplacian in cylindrical coordinates. For meshes which vary no more than ~5% from cell to cell (i.e. δ or λ = 1.05) the results of Eq. (2) are quite good. For more rapidly expanding (or contracting meshes) a different approach is warranted. This approach will be discussed in Appendix A.

The solution technique used to solve the coupled set of algebraic equations from Eq. (2) is called cyclic successive over-relaxation (S.O.R). First, a brief description of this technique follows. Equation (2) is rewritten, regrouping terms to obtain:

$$\psi_{j,k} = \left[\frac{1}{r_j(r_{j+1} - r_{j-1})} \left\{ \frac{(r_{j+1} + r_j)}{(r_{j+1} - r_j)} + \frac{(r_j + r_{j-1})}{(r_j - r_{j-1})} \right\} \right.$$

$$\left. + \frac{2}{r_j^2\,(\theta_{k+1} - \theta_{k-1})} \left\{ \frac{1}{(\theta_{k+1} - \theta_k)} + \frac{1}{(\theta_k - \theta_{k-1})} \right\} \right]$$

$$= \frac{1}{r_j\,(r_{j+1} - r_{j-1})} \left[\left(\frac{r_{j+1} + r_j}{r_{j+1} - r_j} \right) \psi_{j+1,k} \right.$$

$$\left. + \left(\frac{r_j + r_{j-1}}{r_j - r_{j-1}} \right) \psi_{j-1,k} \right]$$

$$+ \frac{2}{r_j^2\,(\theta_{k+1} - \theta_{k-1})} \left[\frac{\psi_{j,k+1}}{\theta_{k+1} - \theta_k} + \frac{\psi_{j,k-1}}{\theta_k - \theta_{k-1}} \right] \tag{5}$$

In matrix form, Eq. (5) can be expressed as

$$\underline{\underline{A}}\ \underline{\psi} = 0 \tag{6}$$

where $\underline{\underline{A}}$ is a five banded diagonal matrix. $\underline{\underline{A}}$ can be split into three matrices such that

$$\underline{\underline{A}} = (\underline{\underline{L}} + \underline{\underline{U}} + \underline{\underline{I}}) \tag{7}$$

Equation (6) becomes

$$(\underline{\underline{L}} + \underline{\underline{U}})\ \underline{\psi} + \underline{\underline{I}}\underline{\psi} = 0 \tag{8}$$

From this equation, all iterative numerical methods can be derived. For the case of cyclic S.O.R with an arbitrary acceleration factor ω, Eq. (8) becomes

$$\psi_{\nu}^{n+1} = - \omega(\underline{\underline{L}} + \underline{\underline{U}}) \quad \psi_{1-\nu}^{n} + (1-\omega) \; \psi_{\nu}^{n-1} \tag{9}$$

where the subscript ν is used to denote the cyclic (in grid point space) solution of the ψ's. In the case of finite difference mesh, ν is either 1 or 0 depending on the grid point. The mesh is swept twice (half of the grid points each time). The difference form of Eq. (9) then becomes

$$\psi_{j,k}^{n+1} = (1-\omega_n) \quad \psi_{j,k}^{n-1} + \frac{\omega_n}{\gamma_j(\alpha_j+\beta_j) + \frac{\gamma_k}{r_j^2} \quad (\alpha_k + \beta_k)}$$

$$\left[\gamma_j \; (\alpha_j \; \psi_{j+1,k}^{n} + \beta_j \; \psi_{j-1,k}^{n}) + \frac{\gamma_k}{r_j^2} \; (\alpha_k \; \psi_{j,k+1} \right.$$

$$\left. + \beta_k \quad \psi_{j,k-1}) \right] \tag{10}$$

For convenience, the parameters α, β, γ are introduced to denote

$$\alpha_j = \frac{(r_{j+1} + r_j)}{(r_{j+1} - r_j)} \qquad \chi_k = \frac{1}{(\theta_{k+1} - \theta_k)}$$

$$\beta_j = \frac{(r_j + r_{j-1})}{(r_j - r_{j-1})} \qquad \beta_k = \frac{1}{(\theta_k - \theta_{k-1})}$$

$$\gamma_j = \frac{1}{r_j \; (r_{j+1} - r_{j-1})} \qquad \gamma_k = \frac{2}{(\theta_{k+1} - \theta_{k-1})} \tag{11}$$

The subscript on the acceleration parameter ω_n is used to indicate variable acceleration (Chebyshev). Omega is defined as

$$\omega_n = {}^{1}/(1 - 1/4 \ \mu_m \ \omega_{n-1}) \tag{12}$$

where μ_m is the largest eigenvalue (spectral radius) of the coefficient matrix given by Eq. (10), and $\omega_1 = 1$. Then, as $n \Rightarrow \infty$, the optimum acceleration parameter can be found for the cartesian form of the Laplacian as

$$t^2 \ \omega_{opt}^2 - 16\omega_{opt} + 16 = 0 \tag{13}$$

Where $t = 2 \cos(\pi/n)$, ω_{opt} is the largest root of (13), and n is the number of cells on a side of the 2-D cartesian mesh. It is also better to estimate ω_{opt} too large rather than too small. From Eqs. (12) and (13) an estimate of ω_{opt} and (indirectly) μ_m can be obtained if it is not possible to estimate the spectral radius directly.

The code was written for either quarter or half-plane symmetry. Thus at the end theta-grid-points, the boundary condition

$$\frac{\partial \psi_{j,k}}{\partial \theta} = 0 \tag{14}$$

is applied exactly. The inner and outer boundaries are user defined Dirichlet conditions.

CODE INPUT DESCRIPTION

The data fields for each card for LAPLACE are described below. No format fields are required.

First Card

JMAX, KMAX, MAXITER, RIMIN

JMAX = the number of cells in r direction
(JMAXP = JMAX + 1 = # of grid points)

KMAX = same as JMAX but in θ direction

MAXITER = maximum # of iterations allowed to converge solution

RMIN = radius of inner boundary

Second Card

DELR, DELT, GAM, XLAM, SPR

DELR = ΔR_o

DELT = $\Delta \theta_o$

GAM = radial mesh expansion factor as in Eq. (4)

XLAM = theta mesh expansion factor as in Eq. (4)

SPR = estimate of spectral radius (~.6 - .9)

Third Card

ERR, JERR, KERR, INTERP

ERR = relative error convergence

JERR, KERR = subscripts of point for error check

INTERP = flag for $^{1}/r$ mesh interpolation (0 = no, 1 = yes)

Fourth Card

IPF, IPTF, NCTRS

IPF = flag for starting grid values print option as with INTERP

IPTF = polar plot flag option as above

NCTRS = # of contours desired (max is 50)

Fifth Card

KSKIP, ISURF

KSKIP = last subscript is theta array for plotting (≤KMAX + 1)

ISURF = flag for outer boundary and magnet setting option (1 = set boundary and magnet at $\psi = \pi/2 - \theta$, 0 = read in potentials)

Sixth Card (if ISURF = 0)

PSI (1,K) K = 1, KMAX + 1
PSI (JAMX + 1, K), K = 1, KMAX + 1 } boundary values of potential

Seventh Card

NSRID (J), J=1, JMAX + 1, start K index for each r node used to position magnet

Eighth Card (if ISURF = 0)

PVAL = values of potential at grid points corresponding to magnet surface (i.e., where NSRID(J) = 1)

The input arguments to subroutine POLCONF called by LAPLACE are also given here with a brief description of the function of this subroutine.

The purpose of POLCONF is to produce a polar contour plot of a variable Z(THETA, R). The arguments are:

CALL POLCONF (THETA, NT, R, NR, Z, NZT, NZR, NC, ZMN, ZMX, DLZ, ZC, RMAX, IGRID, ITITLE, NTITLE)

Where:

THETA = table of angles in radians.

NT = number of points in the THETA table to be used. If NT is negative, ZMN will be calculated by POLCONF as the minimum value of Z.

R = table of radii.

NR = number of points in the R table to be used. If NR is negative ZMX will be calculated by POLCONF as the maximum value of Z.

Z = origin of matrix of values of function to be contoured. Z(I,J) should be the value of Z at [THETA (I), R(J)].

NZT = length of a column of Z matrix. If Z is dimensioned (10, 20) then NZT = 10 and NZR = 20.

NZR = length of a row of Z matrix. If NZR is <0, ZC table is computed such that NC is the minimum of NC and (ZMX-ZMN)/DLZ. ZMX and ZMN are made multiples of DLZ.

NC = number of contours to be plotted. If NC 0, ZC table is assumed to be supplied by the user, and ZMX, ZMX and DLZ are not used. The absolute value of NC must be less than, or equal to 50.

ZMN = minimum value of contour to be used in contouring. If NT<0, ZMN will be computed from minimum of Z over contour grid.

ZMX = maximum value of contour to be used in contouring. If NR 0, ZMX will be computed from maximum value of Z over contour grid.

DLZ = interval between contours. If DLZ<0, DLZ will be set to (ZMX-ZMN)/(NC-1).

ZC = table of contour values. If NC>0, ZC table is calculated by POLCONF. ZC storage must be assigned by the user. At least |NC| values must be supplied and the values must be stored in increasing order in ZC. Results are unpredictable if ZC(I+1)<ZC(I).

RMAX = the length of the radius of the grid circle in inches.

INGRID = number of grid lines/interval to be drawn. If IGRID <0, no grid is drawn. If IGRID > 0, then IGRID circles are drawn and radial lines at 30° intervals are drawn.

ITITLE = BCD array containing titling information to be drawn at top of map.

NTITLE = number of characters in ITITLE. If NTITLE < 0 and NC > 0, then ZMN and ZMX are recomputed to be (MOD(DLZ)), and NC is recomputed to be MIN(NC) (ZMX-ZMN)/(DLZ).

The array of points, Z(THETA,R) is systematically contoured by considering rectangles having four adjacent points for vertices. The chosen rectangle is then divided into two triangles by choosing that diagonal which has minimum Z between its end points. (This particular procedure was adopted because it results in shorter interpolation distances in the direction of maximum slope.) Since each triangle represents a plane, the problem is reduced to determining the lines of intersection of the contour planes and the individual triangles. This is accomplished by performing linear interpolation between the vertices of the triangles to locate points where the individual contour lines intersect each side. These end points are then paired and individual segments of contour lines are drawn between them. The subroutine TRIPOL is called by POLCONF.

ANALYTIC PROBLEMS, MAGNET PROBLEMS AND RESULTS

1) Problem 1 is defined below with boundary conditions as shown.

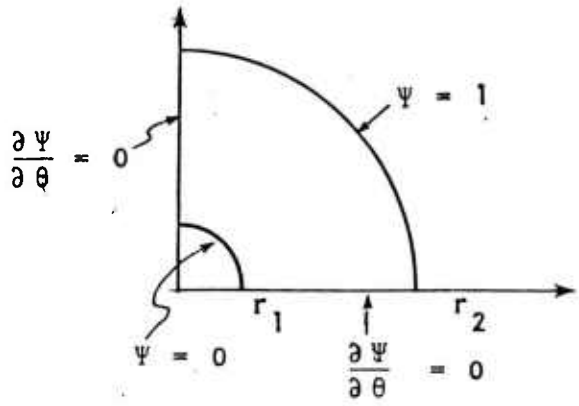

Fig. 2 Problem 1 geometry.

This problem exhibits quarter plane symmetry so Laplace equation reduces to

$$\frac{1}{r}\frac{\partial}{\partial r}\left(r\frac{\partial \psi}{\partial r}\right) = 0$$

The solution to this equation with boundary conditions, as given in Fig. 2, is

$$\psi = \frac{\ell n(r/r_1)}{\ell n(r_2/r_1)}$$

This test problem was run with parameters as given below for both uniform mesh:

```
INPUT JMAX, KMAX, MAXITER, RMIN
JMAX= 40   KMAX= 45   MAXITER= 500   RMIN= 7.620E + 00
INPUT DELR, DELT, GAM, XLAM, SPR
DELR= 3.8100E-01, DELT= 3.4907E-02, GAM= 1.0000E+00, XLAM= 1.0000E+00, SPR= 9.0000E-01
INPUT ERR, JERR, KERR, INTERP
ERR= 1.0000E-04   JERR= 5   KERR= 5
INTERPOLATION PARAMETER IS (1=YES, 0=NO) 1
INPUT PRINT, PLOT FLAGS AND NUMBER OF CONTOURS
IPF= 1  IPTF= 1  NUMBER OF CNTRS 10
INPUT POLAR SKIP FACTOR AND POTENTIAL FLAG OPTION
KSKIP= 1  ISURF= 0
INPUT BOUNDARY VALUES OF PSI
INPUT VALUES FOR NGRID(J), TO JMAX+1
   1   1   1   1   1   1   1   1   1   1   1   1   1   1   1   1   1   1   1   1
   1   1   1   1   1   1   1   1   1   1   1   1   1   1   1   1   1   1   1   1
   1
```

and geometric mesh:

```
INPUT JMAX, KMAX, MAXITER, PMIN
JMAX= 40   KMAX= 44   MAXITER= 500   RMIN= 7.620E+00
INPUT DELR, DELT, GAM, XLAM, SPR
DELR= 2.0000E-01  DELT= 2.0000E-02  GAM= 1.0305E+00  XLAM= 1.0250E+00  SPR= 9.0000E-01
INPUT ERR, JERR, KERR, INTERP
ERR= 1.0000E-04   JERR= 7   KERR= 7
```

```
INTERPOLATION PARAMETER IS (1=YES, 0=NO) 1
INPUT PRINT, PLOT FLAGS AND NUMBER OF CONTOURS
IPF= 1   IPTF= 1   NUMBER OF CNTRS 10
INPUT POLAR SKIP FACTOR AND POTENTIAL FLAG OPTION
KSKIP= 1   ISURF= 0
INPUT BOUNDARY VALUES OF PSI
INPUT VALUES FOR NGRID(J), TO JMAX+1
   1   1   1   1   1   1   1   1   1   1   1   1   1   1   1   1   1   1   1   1
   1   1   1   1   1   1   1   1   1   1   1   1   1   1   1   1   1   1   1   1
   1
```

where the error is calculated from

$$\frac{\psi^{n+1}_{jerr,kerr} - \psi^{n}_{jerr,kerr}}{\psi^{n}_{jerr,kerr}} = \varepsilon \qquad (17)$$

The results were as follows:

$\psi^{exact}_{5,5} = .16596$; $\psi^{code}_{5,5} = 1.641$ (uniform grid)

$\psi^{exact}_{7,7} = .1428$; $\psi^{code}_{7,7} = .1413$ (nonuniform grid)

The non-uniform grid results are more accurate due to the better resolution in the region of interest (7,7). Also the grid points do not coincide, but the absolute r, θ coordinates are very close. Both runs required over 400 iterations and approximately 3 cps of time. Plots of the results are given in Figs. 5a and 5b.

2) Problem 2 is depicted below:

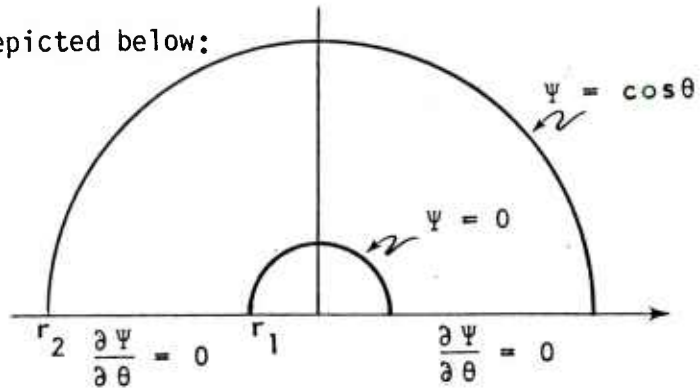

Fig. 3 Problem 2 geometry.

This problem includes half plane symmetry as well as angular dependence of the potential. Using the method of separation of variables to solve the two-dimensional cylindrical Laplacian, the following is obtained.

$$\frac{\partial^2 g}{\partial \theta^2} + \nu^2 g = 0 \qquad g \Rightarrow g(\theta) \qquad (18)$$

$$\frac{1}{r}\frac{\partial}{\partial r}\left(r \frac{\partial f}{\partial r}\right) - \frac{\nu^2}{r^2} f = 0 \qquad f \Rightarrow f(r) \qquad (19)$$

Since g is single valued, ν must be an integer and, because of the outer boundary, $\nu = 1$. Solutions to Eq. (19) are of the form $f(r) = r^{\pm\nu}$. Therefore solutions to Laplace's equation for the potential can be constructed as follows

$$\psi = A(r\cos) + B\left(\frac{\cos}{r}\right) \tag{20}$$

By using the boundary conditions and solving for the constants

$$\psi = \frac{r\cos\theta}{r_2\left(1 - (r_1/r_2)^2\right)} - \frac{r_1^2\cos\theta}{rr_2\left(1 - (r_1/r_2)^2\right)} \tag{21}$$

is obtained.

Running this test problem for two meshes, using the parameters listed below,

```
INPUT JMAX, KMAX, MAXITER, RMIN
JMAX= 40  KMAX= 45   MAXITER= 500  RMIN= 7.620E+00
INPUT DELR, DELT, GAM, XLAM, SPR
DELR= 2.8100E-01, DELT= 6.9810E-02, GAM= 1.0000E+00, XLAM= 1.0000E+00, SPR= 9.0000E-01
INPUT ERR, JERR, KERR, INTERP
ERR= 1.0000E-04   JERR= 5   KERR= 5
INTERPOLATION PARAMETER IS (1=YES, 0=NO) 1
INPUT PRINT, PLOT FLAGS AND NUMBER OF CONTOURS
```

```
IPF= 1   IPTF=1   NUMBER OF CNTRS 20
INPUT POLAR SKIP FACTOR AND POTENTIAL FLAG OPTION
KSKIP= 34  ISURF= 1
INPUT VALUES FOR NGRID(J), TO JMAX+1
   1   1   1   1   1   1   1   1   1   1   1   1   1   1   1   1   1   1   1   1
   1   1   1   1   1   1   1   1   1   1   1   1   1   1   1   1   1   1   1   1
   1
INPUT  JMAX, KMAX, MAXITER, RMIN
JMAX= 40   KMAX= 45   MAXITER= 500   RMIN= 7.620E+00
INPUT DELR, DELT, GAM, XLAM, SPR
DELR= 2.0000E-01, DELT= 2.0000E-02, GAM= 1.0305E+00, XLAM= 1.0494E+00, SPR= 9.0000E-01
INPUT ERR, JERR, KERR, INTERP
ERR= 1.0000E-04   JERR= 7   KERR= 8
INTERPOLATION PARAMETERS IS (1= YES, 0= NO) 1
INPUT PRINT, PLOT FLAGS AND NUMBER OF CONTOURS
IPF= 1   IPTF= 1   NUMBER OF CNTRS 20
INPUT POLAR SKIP FACTOR AND POTENTIAL FLAG OPTION
KSKIP= 34   ISURF= 1
INPUT VALUES FOR NGRID(J), TO JMAX+1
   1   1   1   1   1   1   1   1   1   1   1   1   1   1   1   1   1   1   1   1
   1   1   1   1   1   1   1   1   1   1   1   1   1   1   1   1   1   1   1   1
   1
```

produced the following results:

$\psi_{5,5}^{exact} = .13206$; $\psi_{5,5}^{code} = .13124$ (uniform mesh)

$\psi_{7,8}^{exact} = .11671$; $\psi_{7,8}^{code} = .1158$ (non-uniform mesh)

Again the absolute error is less than 1%. However, in this example, nearly twice as many iterations were required to converge the geometric case as compared to the uniform grid spacing case (245 vs. 490). Plots of this problem are given in Figs. 6a and 6b. An average of these four runs from problems (1) and (2) would indicate a cp time requirement of

$\sim 9 \times 10^{-6}$ sec/node iteration

This means a problem using 100 x 50 grid points, with $\varepsilon = 10^{-4}$, may require 1000 iterations. Thus

$CP_{time} = (9 \times 10^{-6})\ (5 \times 10^{6}) = 45$ c.p.s.

MAGNET PROBLEMS

Two magnet cases were performed. The parameters were taken from Rockwell-supplied data. From these data two runs were constructed. First a simple, constant ray magnet was placed in the mesh. The dimensions are given below:

r_{min} = 7.62 cm Δr_o = .1 cm

r_{max} = 22.73 cm $\Delta\theta_o$ = .02 R

r_{gap} = .315 cm

magnet height at back = 2.905 cm

magnet height at front = 1.014 cm

all other dimensions and boundary conditions are indicated in Fig. 4.

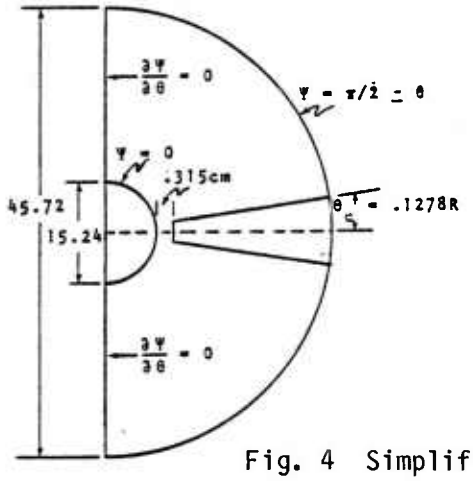

Fig. 4 Simplified magnet geometry.

The actual code input is given below:

```
INPUT JMAX, KMAX, MAITER, RMIN
JMAX= 44   KMAX= 44   MAXITER= 1000   RMIN= 7.620E+00
INPUT DELR, DELT, GAM, XLAM, SPR
DELR= 1.0000E-01, DELT= 2.0000E-02, GAM= 1.0500E+00, XLAM= 1.0250E+00, SPR= 9.0000E-01
INPUT ERR, JERR, KERR, INTERP
ERR= 1.0000E-04   JERR= 2   KERR= 3
INTERPOLATION PARAMETER IS (1 = YES, 0 = NO) 1
```

```
INPUT PRINT, PLOT FLAGS AND NUMBER OF CONTOURS
IPF= 1  IPTF= 1  NUMBER OF CNTRS 20
INPUT POLAR SKIP FACTOR AND POTENTIAL FLAG OPTION
KSKIP= 1   ISURF= 1
INPUT VALUES FOR NGRID(J), TO JMAX+1

   1   1   1   1   1   1   1   1   1   1   1   1   1   1   1   1   1   1   1   1
   1   1   1   1   1   1   1   1   1   1   1   1   1   1   1   1   1   1   1   1
   1   1   1   1   1

INPUT JMAX, KMAX, MAXITER, RMIN
JMAX= 105   KMAX=100   MAXITER= 3000   RMIN= 7.620E+00
INPUT DELR, DELT, GAM, XLAM, SPR
DELR= 1.0000E-02, DELT= 5.0000E=03, GAM= 1.0401E+00, XLAM= 1.0201E+00, SPR= 9.3000E-01
INPUT ERR, JERR, KERR, INTERP
ERR= 1.0000E-04   JERR= 11   KERR= 11
INTERPOLATION PARAMETER IS (1 = YES, 0 = NO) 1
INPUT PRINT, PLOT FLAGS AND NUMBER OF CONTOURS
IPF= 1   IPTF= 1   NUMBER OF CNTRS 20
INPUT POLAR SKIP FACTOR AND POTENTIAL FLAG OPTION
KSKIP= **   ISURF= 1
INPUT VALUES FOR NGRID(J), TO JMAX+1
```

1 1 1 1 1 1 1 1 1 1 1 1 1 1 1 1 1 1 1 1
1 1 21 21 21 21 21 21 21 21 21 21 21 21 21 21 21 21 21 21
21 21 21 21 21 21 21 21 21 21 21 21 21 21 21 21 21 20 20 20
20 20 20 20 20 20 20 20 20 20 20 19 19 19 19 19 19 19 19 19
19 19 19 18 18 18 18 18 18 18 18 18 18 17 17 17 17 17 17 17
17 16 16 16 16 16

For this geometry two runs were actually made. One with and one without the magnet. Since the error check point was in the gap of the magnet and target, the convergence was much faster for the magnet case. Plots of these two cases are given in Figs. 7a and 7b.

The second magnet case performed employed the same boundary conditions as the first case but the magnet was constructed of many separate ray segments. The magnet surface potential was defined two ways, first the potential varied on the surface consistent with the angle i.e.,

$$\psi = \pi/2 - \theta$$

In the second test the magnet surface was an equipotential held at the value $\psi = 1.484$. The dimensions for both are given below:

r_{min} = 7.62 cm Δr_o = .01 cm

r_{max} = 22.85 cm $\Delta\theta_o$ = .0005 R

r_{gap} = .343 cm

magnet height at back = 1.977 cm

magnet height at front = .9683 cm

The actual code input listing is given below.

```
INPUT JMAX, KMAX, MAXITER, RMIN
JMAX= 105   KMAX= 100   MAXITER= 3000   RMIN= 7.620E+00
INPUT DELR, DELT, GAM, XLAM, SPR
DELR= 1.0000E-02, DELT= 5.0000E-03, GAM= 1.0401E+00, XLAM= 1.0201E+00, SPR= 9.3000E-01
INPUT ERR, JERR, KERR, INTERP
ERR= 1.0000E-04   JERR= 11   KERR= 11
INTERPOLATION PARAMETER IS (1=YES, 0=NO) 1
INPUT PRINT, PLOT FLAGS AND NUMBER OF CONTOURS
IPF=1   IPTF= 1   NUMBER OF CNTRS 20
INPUT POLAR SKIP FACTOR AND POTENTIAL FLAG OPTION
KSKIP= **   ISURF= 1
INPUT VALUES FOR NGRID(J), TO JMAX+1
```

1	1	1	1	1	1	1	1	1	1	1	1	1	1	1	1	1	1	1	1
1	21	21	21	21	21	21	21	21	21	21	21	21	21	21	21	21	21	21	21
21	21	21	21	21	21	21	21	21	21	21	21	21	21	21	21	21	20	20	20
20	20	20	20	20	20	20	20	20	20	20	19	19	19	19	19	19	19	19	19
19	19	19	18	18	18	18	18	18	18	18	18	18	17	17	17	17	17	17	17
17	16	16	16	16	16														

The results are presented in Figs. 8a and 8b respectively.

POTENTIAL CONTOURS FOR FIGURES 5a, 5b

IDENTIFICATION	CONTOUR VALUE
A A	0.
B B	.111
C C	.222
D D	.333
E E	.444
F F	.555
G G	.666
H H	.777
I I	.888
J J	1.0

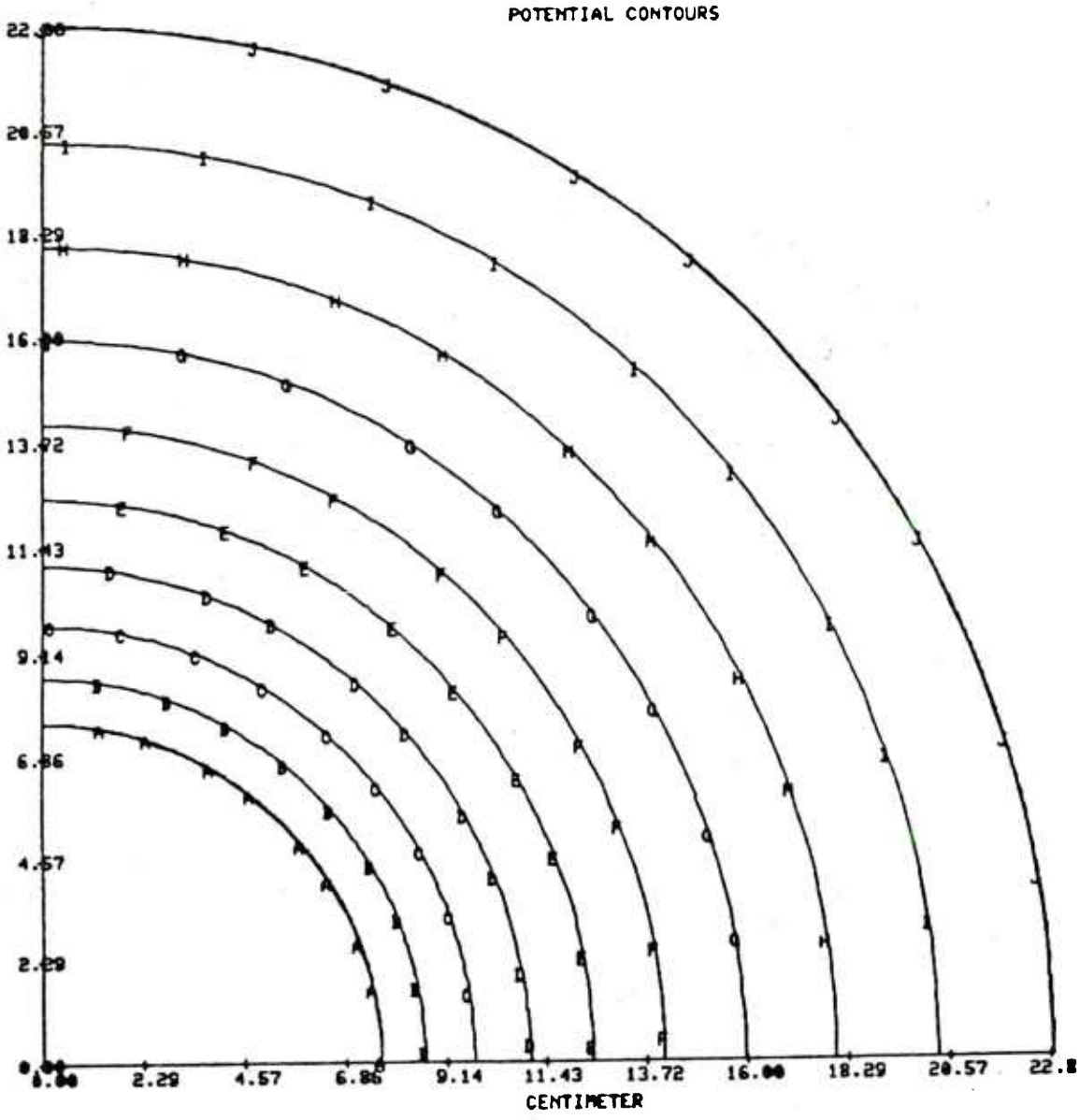

Fig. A-5 Plot of problem 1 with uniform mesh.

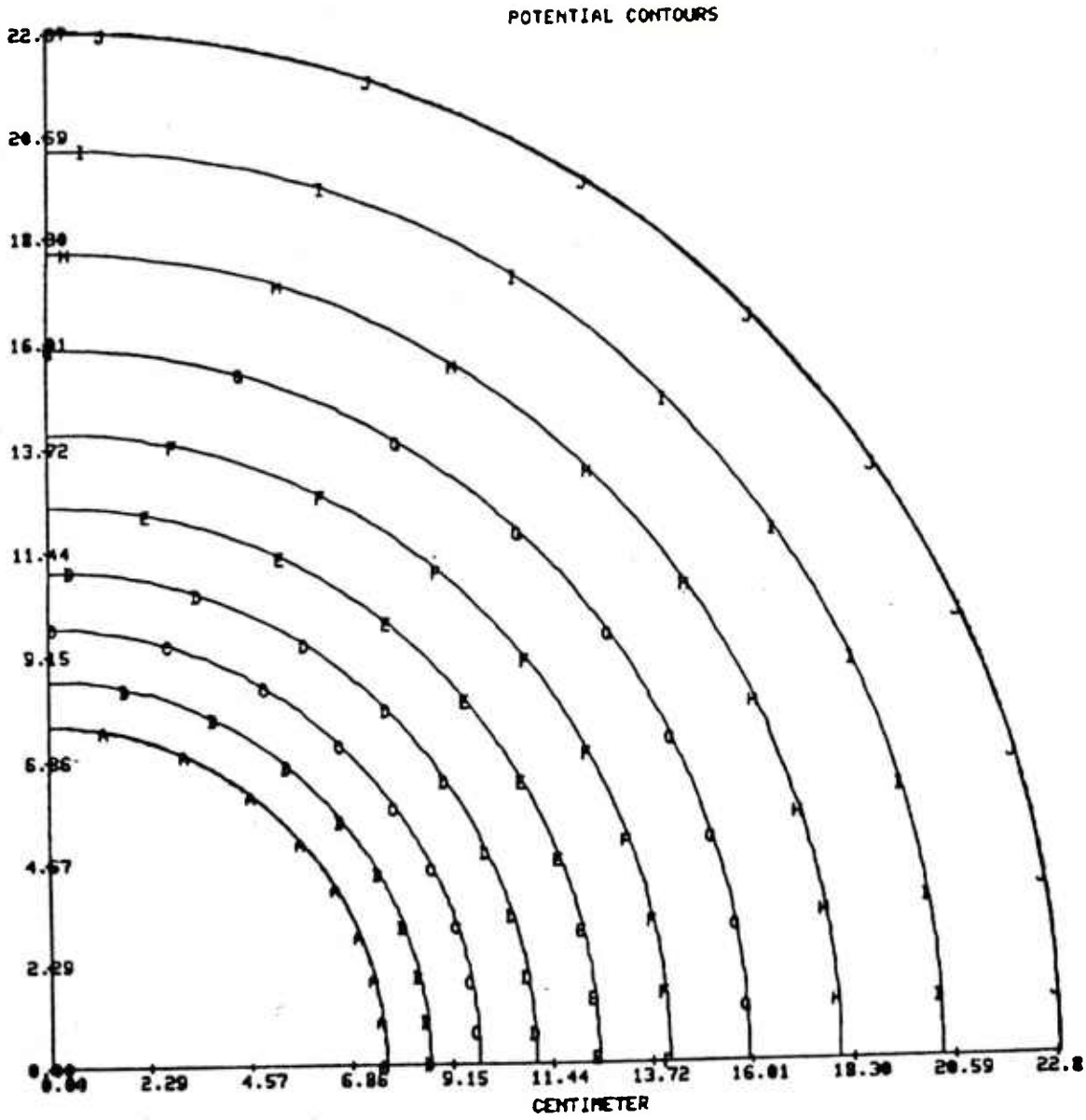

Fig. A-5b Plot of problem 1 with geometric mesh.

POTENTIAL CONTOURS FOR FIGURE 6a

IDENTIFICATION	CONTOUR VALUE
I I	.0233
J J	.1121
K K	.2009
L L	.2897
M M	.3785
N N	.4673
O O	.5561
P P	.6449
Q Q	.7337
R R	.8225
S S	.9113

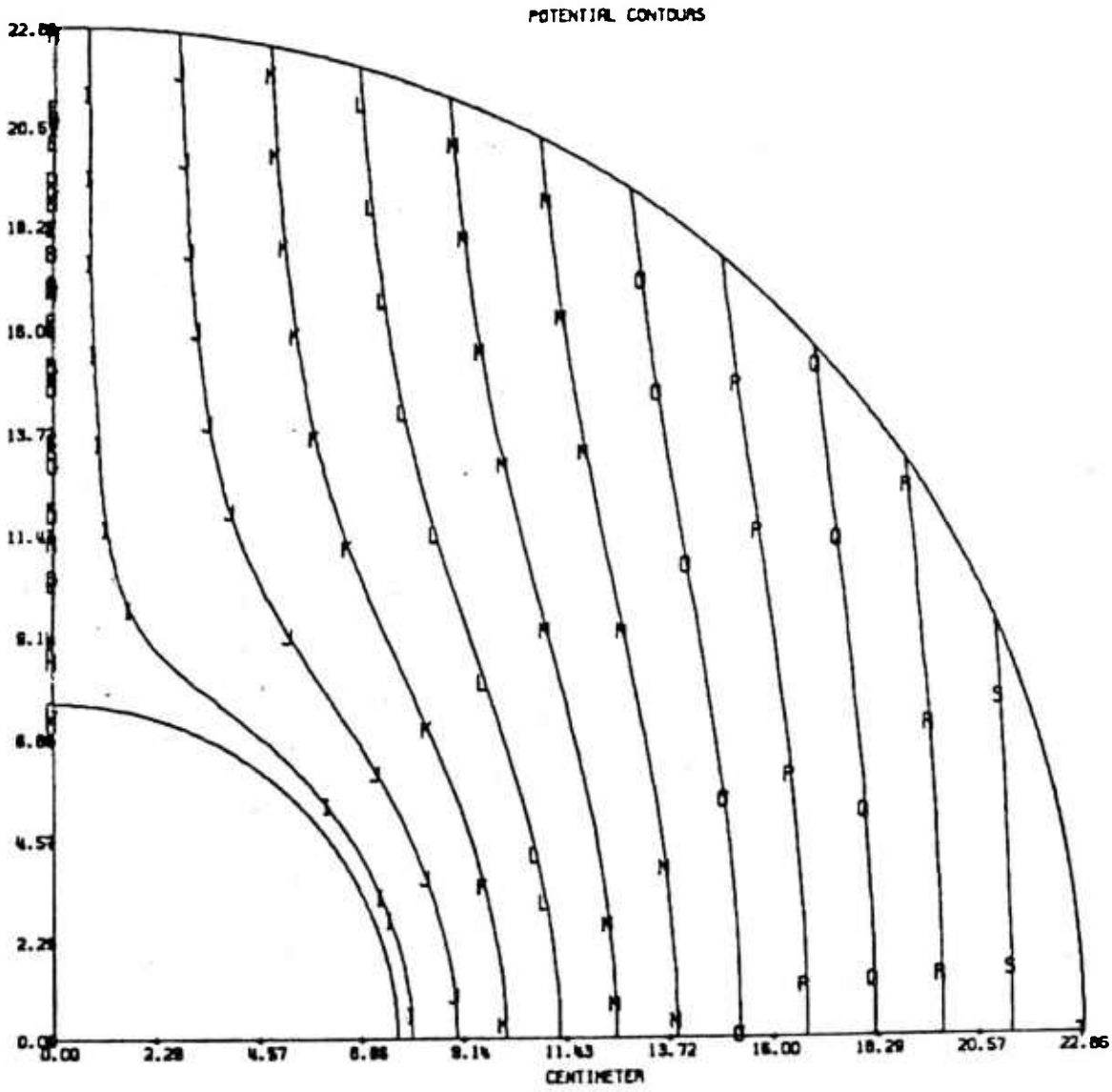

Fig. A-6a Plot of problem 2 with uniform mesh.

POTENTIAL CONTOURS FOR FIGURE 6b

IDENTIFICATION	CONTOUR VALUE
A A	-1.208E-02
B B	4.119E-02
C C	9.446E-02
D D	1.477E-01
E E	2.010E-01
F F	2.543E-01
G G	3.075E-01
H H	3.608E-01
I I	4.141E-01
J J	4.673E-01
K K	5.206E-01
L L	5.739E-01
M M	6.271E-01
N N	6.804E-01
O O	7.337E-01
P P	7.869E-01
Q Q	8.402E-01
R R	8.935E-01
S S	9.4677E-01
T T	1.000E+00

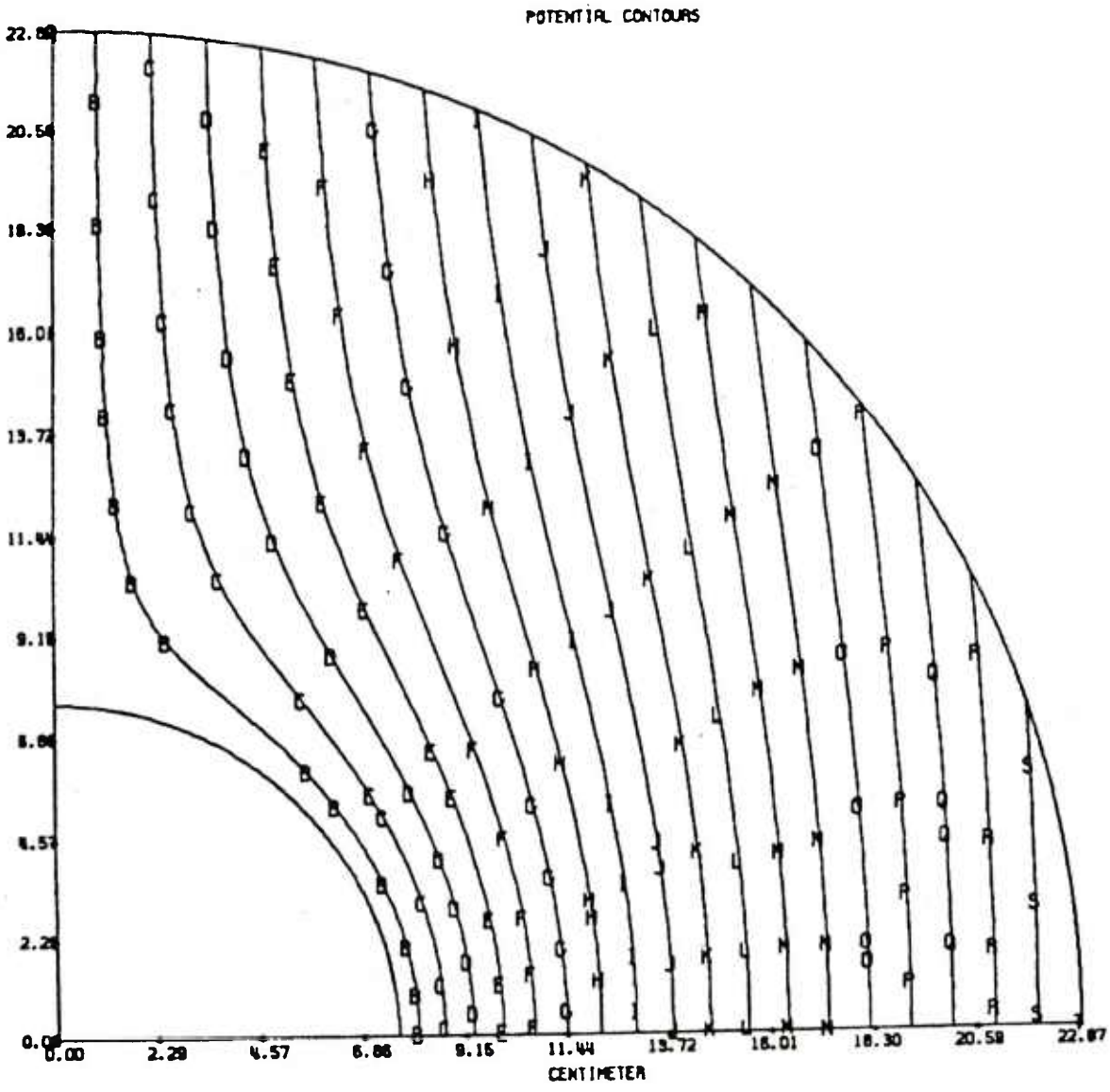

Fig. A-6b Plot of problem 2 with non-uniform mesh (Note different number of contour values).

POTENTIAL CONTOURS FOR FIGURES 7a, 7b

IDENTIFICATION	CONTOUR VALUE
A A	0.
B B	8.267E-02
C C	1.653E-01
D D	2.480E-01
E E	3.307E-01
F F	4.134E-01
G G	4.960E-01
H H	5.787E-01
I I	6.614E-01
J J	7.441E-01
K K	8.267E-01
L L	9.094E-01
M M	9.921E-01
N N	1.075E+00
O O	1.157E+00
P P	1.240E+00
Q Q	1.323E+00
R R	1.405E+00
S S	1.488E+00
T T	1.571E+00

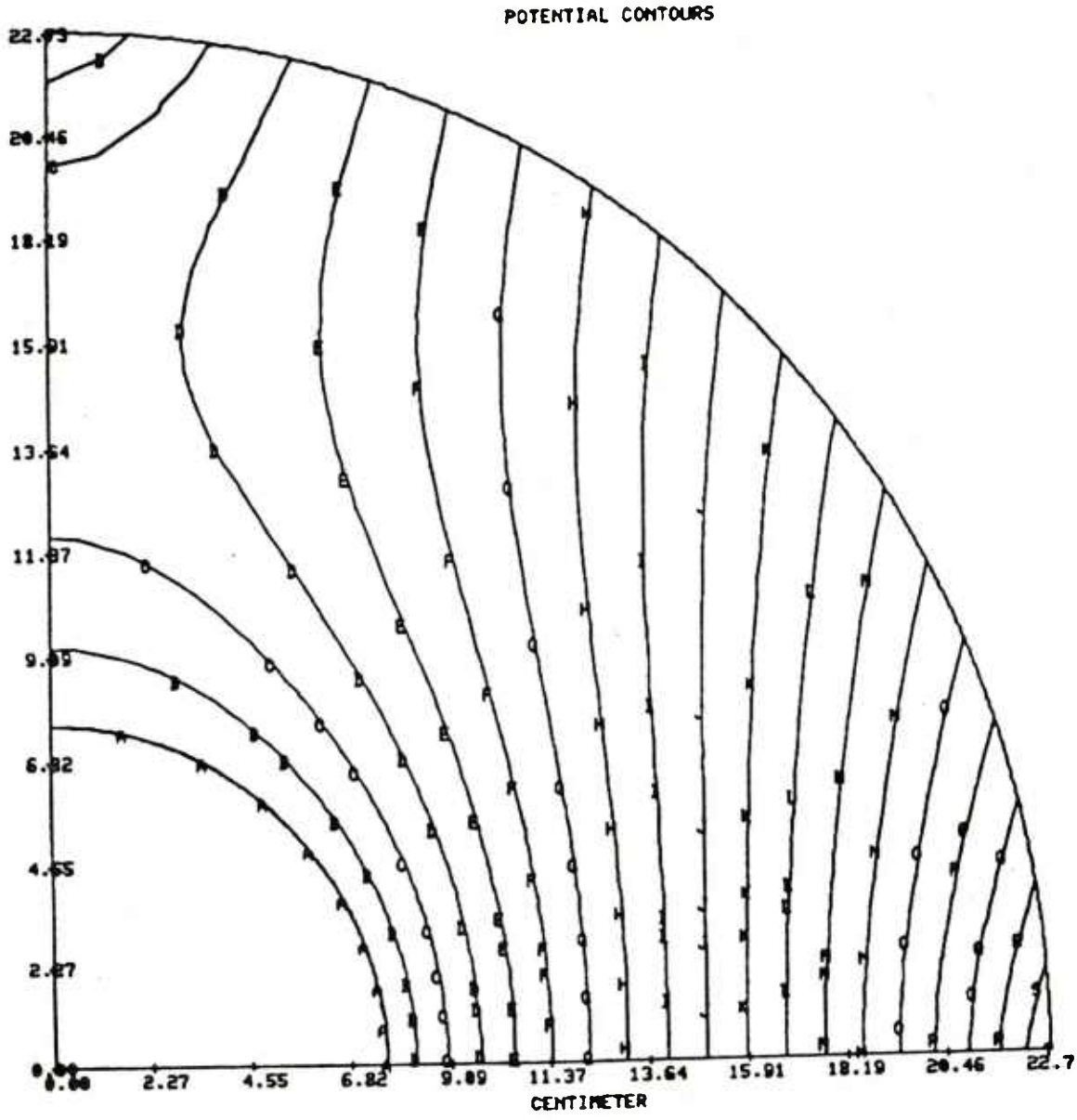

Fig. A-7a Magnet design problem in empty mesh (geometric).

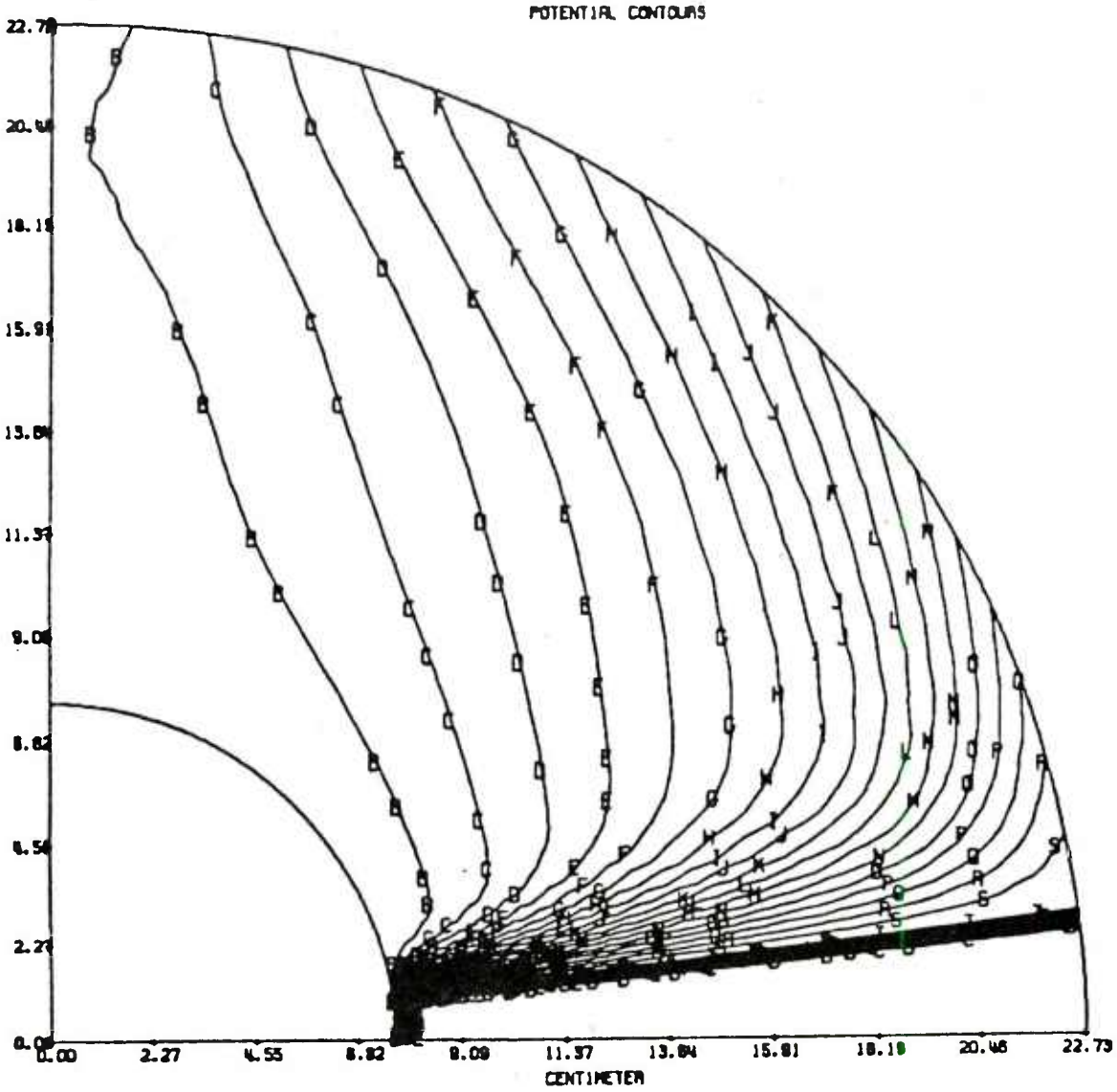

Fig. A-7b Simplified magnet configuration (geometric mesh).

POTENTIAL CONTOURS FOR FIGURES 8a, 8b

IDENTIFICATION	CONTOUR VALUE
A A A A	-3.487E-04
B B B B	7.779E-02
C C C C	1.559E-01
D D D D	2.341E-01
E E E E	3.122E-01
F F F F	3.903E-01
G G G G	4.685E-01
H H H H	5.466E-01
I I I I	6.248E-01
J J J J	7.029E-01
K K K K	7.810E-01
L L L L	8.592E-01
M M M M	9.373E-01
N N N N	1.015E+00
O O O O	1.094E+00
P P P P	1.172E+00
Q Q Q Q	1.250E+00
R R R R	1.328E+00
S S S S	1.406E+00
T T T T	1.484E+00

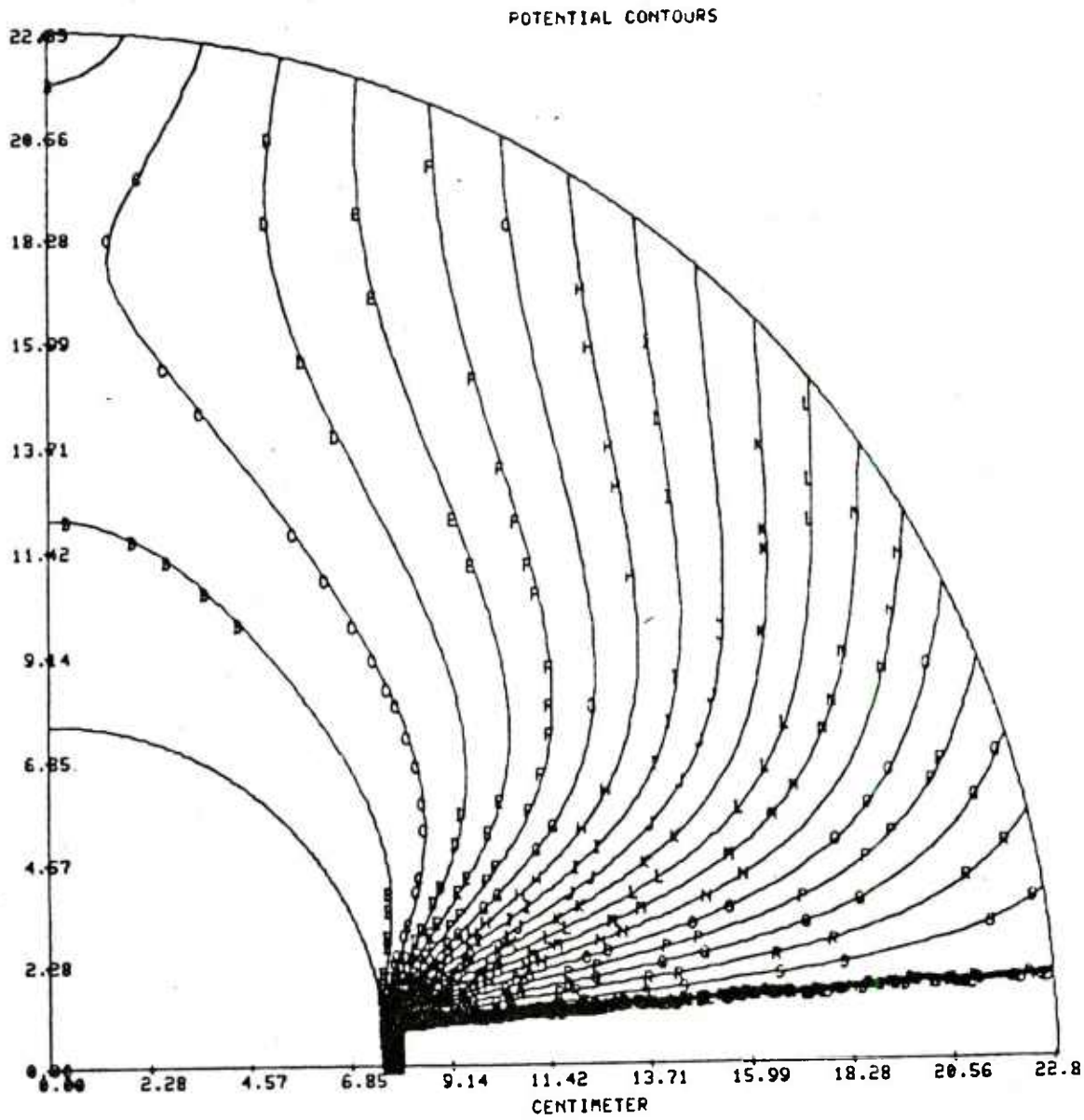

Fig. A-8a Complex magnet geometry non-uniform surface potential.

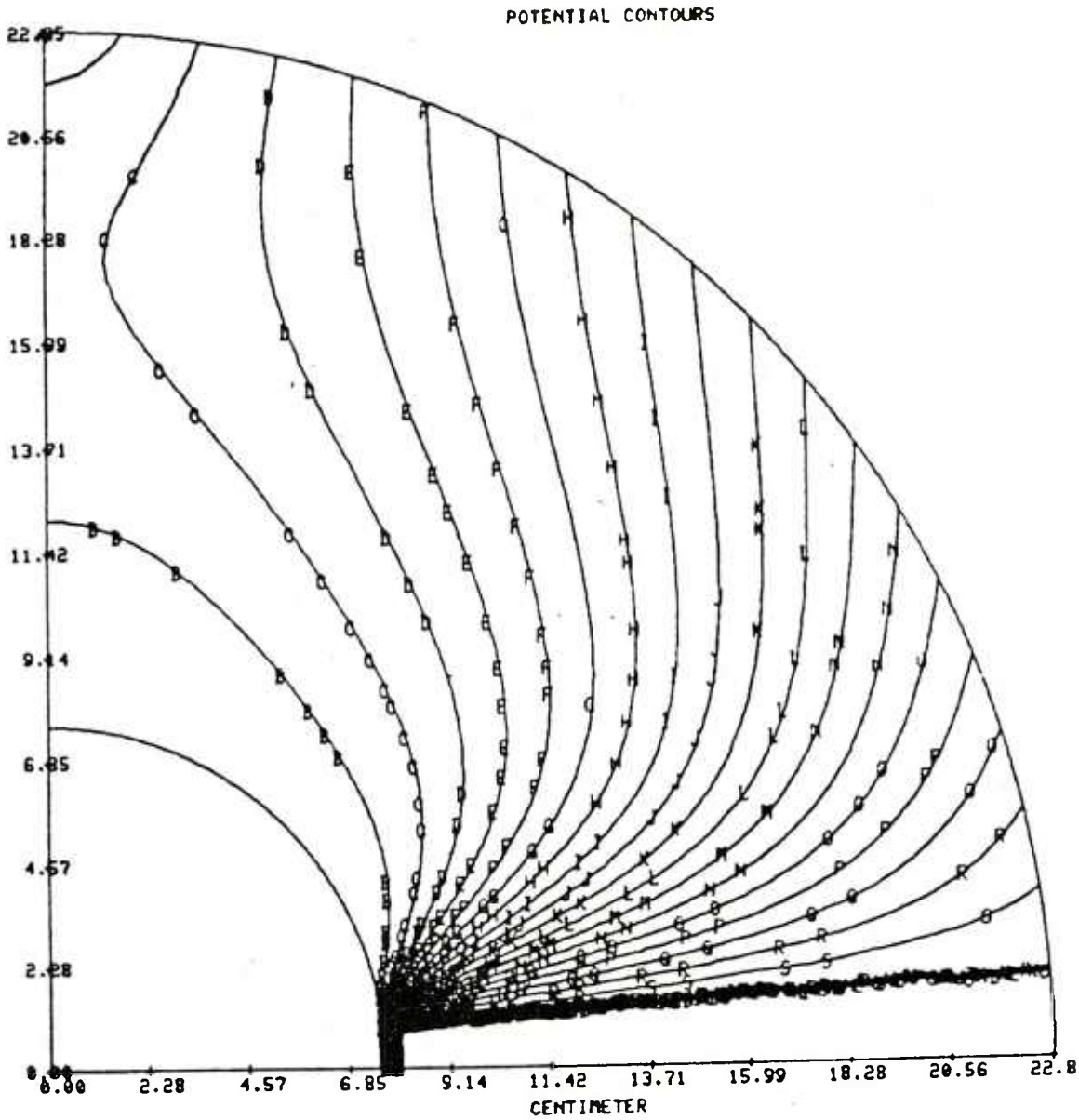

Fig. A-8b Complex magnet geometry uniform surface potential.

APPENDIX B - (Sub 1)

ALTERNATE APPROACH FOR SECOND ORDER NON-UNIFORM MESH

As pointed out in Part 2 of this report, the non-uniform mesh introduces centering errors which cause error in the difference equations proportional to the mesh expansion or contraction rate. Herein an alternate method, which is second order for an exponential mesh regardless of expansion or contraction rate, is proposed. The generalized form of the Laplacian in r-θ coordinates is given by

$$\nabla^2\psi = \frac{1}{h_1 h_2}\left\{\frac{\partial}{\partial u_1}\ \frac{h_2}{h_1}\ \frac{\partial\psi}{\partial u_1} + \frac{\partial}{\partial u_2}\ \frac{h_1}{h_2}\ \frac{\partial\psi}{\partial u_2}\right\} \tag{22}$$

using an exponential form for both meshes

$$r = e^{u1} \Rightarrow dr = e^{u_1}\, du_1 \tag{23}$$

$$\theta = e^{u_2} \Rightarrow d\theta = e^{u_2}\, du_2$$

therefore

$$(ds)^2 = (dr)^2 + r^2(d\theta)^2$$

$$= e^{2u_1}(du_1)^2 + e^{2u_1} e^{2u_2} (du_2)^2 \tag{24}$$

so

$$h_1 = r = e^{u_1}$$

$$h_2 = r\theta = e^{u_1 u_2} \tag{25}$$

By substituting this into Eq. (22) above then

$$\nabla^2\psi = \frac{1}{e^{2u_1 u_2}} \frac{\partial}{\partial u_1} e^{u_2} \frac{\partial\psi}{\partial u_1} + \frac{\partial}{\partial u_2} e^{-u_2} \frac{\partial\psi}{\partial u_2} \tag{26}$$

For the case of Laplace's equation we can drop the constant in Eq. (26) to get

$$\frac{\partial^2\psi}{\partial u_1^2} + e^{-u_2} \frac{\partial}{\partial u_2} e^{-u_2} \frac{\partial\psi}{\partial u_2} = 0$$

or (27)

$$\frac{\partial^2\psi}{\partial u_1^2} + e^{-u_2} \left\{ e^{-u_2} \frac{\partial^2\psi}{\partial u_2^2} - e^{-u_2} \frac{\partial\psi}{\partial u_2} \right\} = 0$$

This can be differenced directly in Δu_1 and Δu_2 of uniform spacing while maintaining second order accuracy in the geometric mesh; as

$$\frac{1}{\Delta u_1^2} \left\{ \psi_{j+1,k} + \psi_{j-1,k} - 2\psi_{j,k} \right\} + \frac{1}{\theta_k \Delta u_2^2}$$

(28)

$$\frac{1}{\theta_{k+1/2}} (\psi_{j,k+1} - \psi_{j,k}) - \frac{1}{\theta_{k-1/2}} (\psi_{j,k} - \psi_{j,k-1})$$

Where the k+1/2 in Eq. (28) now is given by

$$\theta_{k\pm1/2} = e^{u_2 \pm \Delta u2/2}$$

This method will have superior accuracy over Eq. (10) in Part 2, however, the added complexity vs accuracy trade-offs would be warranted only for very nonlinear meshes (e.g. $\lambda \gtrsim 1.1$).

APPENDIX C

This appendix summarizes the physical considerations and calculations made to establish the retarding forces (magnetic drag) exerted on the projectile as the associated mechanical part handing equipment attempts to rapidly rotate the shell in the high magnetic inspection field. This field was of more than academic interest because it limited the spin rate of the hydraulic part handling system to about 40 rpm. This spin speed is satisfactory for present inspection rates (about 40 sec per shell), however faster rotation speed will be required in future higher inspection volume systems.

In order to model this drag process and estimate the magnitude of the force it exerts, consider the geometrical arrangement of a metal plate moving past a magnetic pole as shown in Fig. C-1. If an observer rode on the plate as it traveled under the pole piece, the time-dependent field shown in Fig. C-2 would be measured. Let the dimension L be the distance over which the magnetic field goes from near zero (outside the magnet) to its maximum value of B under the pole piece. It therefore takes a time = L/v for a point on the plate to pass into the field B so it is over this distance or time that the magnetic flux changes from zero to B. It is this region over which eddy currents circulate and dissipate the energy that gives rise to the apparent drag force. Figure C-3 shows this region of the metal plate as if it were a single turn coil in which the eddy currents circulate around the circumference.

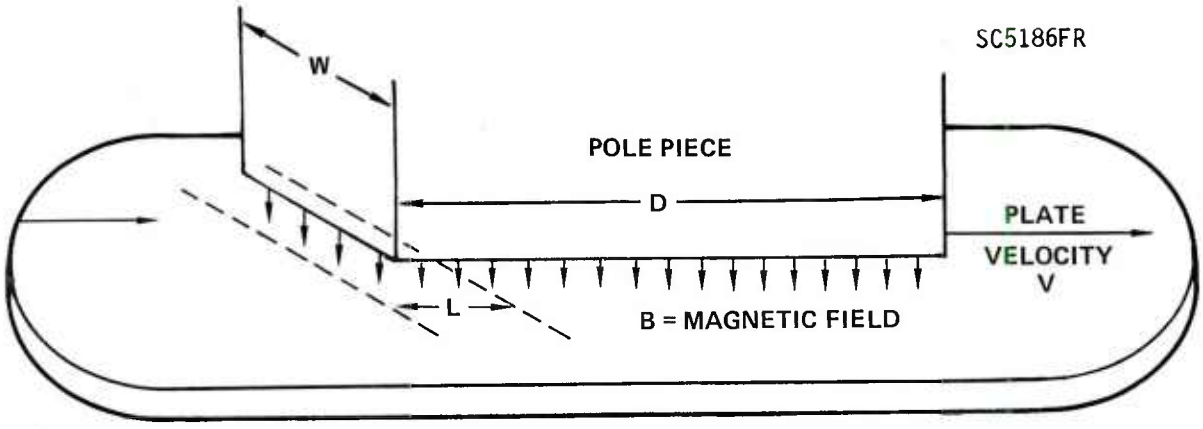

Fig. C-1 Basic configuration of a metal plate moving through the magnetic field of a pole piece.

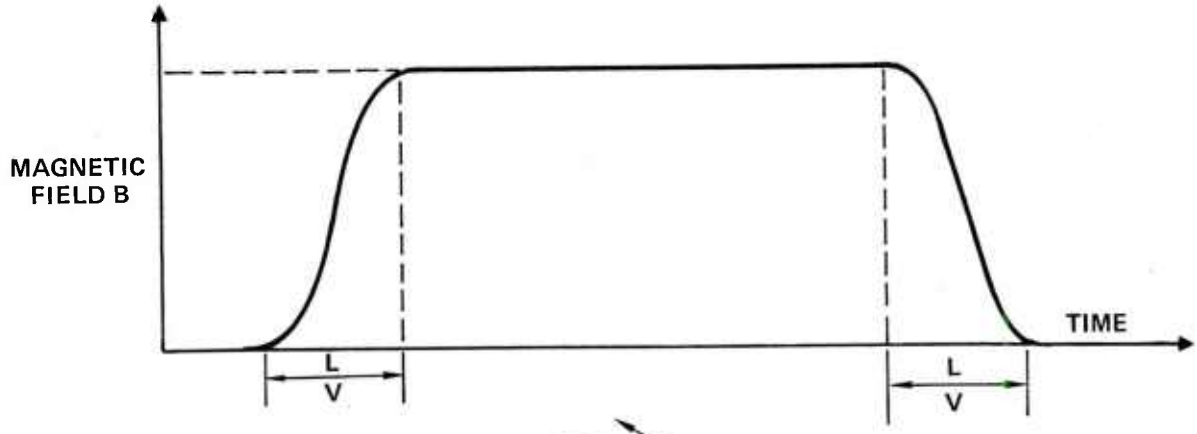

Fig. C-2 Magnetic field variation measured by an observer riding on the moving plate.

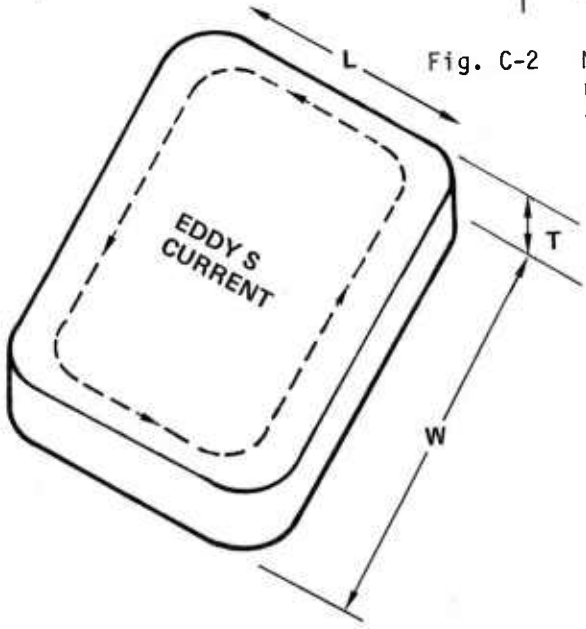

Fig. C-3 Section of the plate in which the eddy currents circulate.

In this type of inspection, the induced electromotive force E is related to the time rate of change of flux ϕ by the relation

$$E(\text{volts}) = \frac{\Delta\phi}{\Delta t} \times 10^{-8} \qquad \text{(C-1)}$$

if ϕ is in gauss cm^2 and t in seconds. From Fig. C-2 $\Delta\phi$ = BxWxL and Δt = L/v since v is the velocity of the plate in cm per sec. Therefore,

$$E = BWv \times 10^{-8} \qquad \text{(C-2)}$$

From the definition of the resistance of a metal loop of length 2(L + W) and a cross-sectional area of LT/2, we have

$$R(\text{ohms}) = \rho \frac{2(L+W)}{LT/2} = \frac{4\rho}{T}\left(1 + \frac{W}{L}\right) \qquad \text{(C-3)}$$

where ρ is the specific resistivity of the metal. Now an emf E in a conductor of resistance R dissipates power at the rate given by

$$P(\text{watts}) = \frac{E^2}{R} \qquad \text{(C-4)}$$

Upon substitution this becomes

$$P = \frac{B^2W^2v^2T}{4\rho(1 + W/L)} \times 10^{-16} \qquad \text{(C-5)}$$

For the usual case, the dimension L will be small compared to W because the flux is confined to the region directly under the pole piece and hence, it jumps up over dimensions small compared to the pole piece dimensions. In this case, $1 + W/L \approx W/L$ and

$$P = \frac{B^2 WLTv^2}{4\rho} \times 10^{-16} \qquad \text{(C-6)}$$

Note that WLT is the volume of material under the edge of the pole piece. Since there will usually be two edges involved in a situation where a plate moves between two pole pieces, the total power dissipated is

$$P_T = \frac{B^2 v^2 (WLT)}{2\rho} \times 10^{-16} \qquad \text{(C-7)}$$

The example of a projectile rotating in our inspection apparatus will have the following parameters; the pole pieces W = 50 cm (20 in) are long, L = 1/2 cm, projectile thickness $T \cong 1$ cm, resistivity $\rho = 10^{-5}$ ohm cm and v = 81 cm/sec (a 155 mm diameter projectile rotating at 100 rpm) yields P_T = 330 watts. The power can be converted to pounds of force by dividing the rotational velocity, ($P = F \times V$), or

$$F(\text{lbs}) = \frac{2.2 \times 10^{-15} \beta^2 V^2 (WLT)}{\rho} \qquad \text{(C-8)}$$

where B is in gauss, V in cm/sec, ρ in ohm cm and WLT in cubic centimeters. Note that the force increases linearly with speed but quadratically with magnetic field. The use of pounds of force for units makes the result convenient for engineering usage.

The dimension T appears in Eq. (C-8) because the flux penetrates the full thickness of the projectile. However, as the speed increases the flux may not penetrate the full thickness. In order to take this dynamic phenomenon into account, the thickness T should be replaced by the electromagnetic skin depth δ because δ describes the depth to which a dynamic magnetic field can penetrate a metal. From classical electromagnetic theory, an electromagnetic wave of frequency ν can be considered to penetrate a metal of resistivity ρ and permeability μ to a depth δ given by

$$\delta = 5 \times 10^3 \sqrt{\frac{\rho}{\mu\nu}} \text{ cm} \qquad \text{(C-9)}$$

To calculate the frequency appropriate to a projectile moving with a velocity V past a magnet with a pole piece length of D, we note that the time over which an observer on the plate would detect a magnetic field would be

$$t = \frac{D}{V} \qquad \text{(C-10)}$$

or more exactly

$$t = \frac{D+2L}{V} \qquad \text{(C-11)}$$

because the magnetic field extends a distance L beyond the edge of the pole piece. This impulse in field would appear as a half cycle of an alternating magnetic field of frequency

$$\nu = \frac{1}{2t} = \frac{V}{2D+4L} \qquad \text{(C-12)}$$

Thus, an effective depth of penetration could be written

$$\delta = 5 \times 10^3 \sqrt{\frac{2\rho(D+2L)}{V\mu}} \text{ cm.} \qquad \text{(C-13)}$$

Using this dimension in place of T in the drag force equation, we obtain

$$F(\text{lbs.}) = 1.56 \times 10^{-11} B^2 WL \sqrt{\frac{V(D+2L)}{\rho\mu}} \qquad \text{(C-14)}$$

which shows that the drag force increases as the square root of the metal speed so long as $\delta<T$. This equation has two serious approximations: one is that we have simply substituted the skin depth parameter δ for the metal thickness which is not exactly correct; and second, when considering ferromagnetic metals, the value of μ is difficult to define because the field inside the metal varies considerably during passage under the pole piece.

In order to determine if Eq. (C-14) can be used to estimate the actual drag force, an experiment was performed in which a 6 inch diameter, iron pipe with a 1/2 inch wall thickness was rotated between the sharply

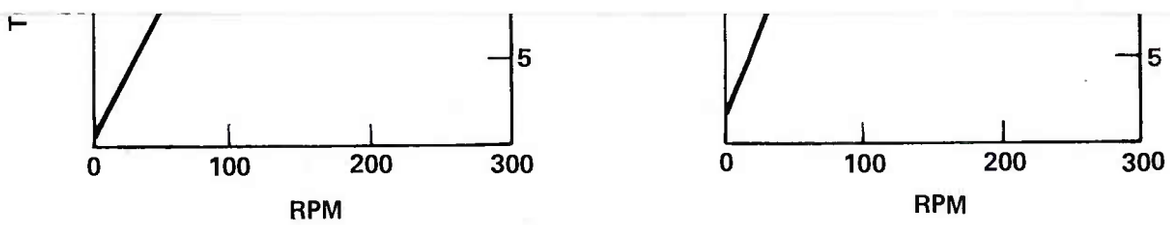

Fig. C-4 Comparison of the drag theory expressed in Eq. (C-14) (solid line) with experimental observations on an iron pipe spun in a magnetic field. The permeability, μ, parameter was chosen to give the best fit at high speeds.

pointed pole pieces of an electromagnet. By using a spring loaded coupling between the drive motor and the pipe, the drag torque on the pipe could be measured as a function of motor speed and magnetic field in the gap between the pole piece and the pipe wall. Figure C-4 shows the results obtained for

APPENDIX D

PROJECTILE INSPECTION STANDARDS

The "standards" that were created in order to test the EMAT inspection techniques were derived from prints supplied by ARRADCOM. The size, (i.e., length and depth) shape and location of the EDM (electrodischarge machined) cuts in the projectiles inner and outer surface were derived from fracture mechanic calculations and tests performed at ARRADCOM.[5] The first set of standards fabricated used penny shaped rounded notches of approximately 0.5" length and 0.020 to 0.030" depth. The EDM work was performed at the Science Center by Murray Mahoney and served to allow a substantial amount of experience to be gained while the hardware and mechanics were being designed and tested. Subsequently, another design for the "flaw standards" was released from ARRADCOM which superseded the previous issue. The notches stipulated as "critical" were bread loaf shaped about 1" long and 0.020" deep. This was the size flaws upon which all final EMAT system tests were conducted.

The location of the 26 (ID and OD) longitudinally oriented flaws are shown schematically in the diagram of Fig. 53. The location of the circumferential simulated flaws is shown in Fig. D-1 (Part No. 9235995) for completeness. These prints of flaws sizes and locations were supplied to a competent EDM job shop (B & W Industries) for manufacture of the required standards. Ultrasonically inspected and certified projectiles were obtained from Norris Industries and sent directly to B & W Industries for fabrica-

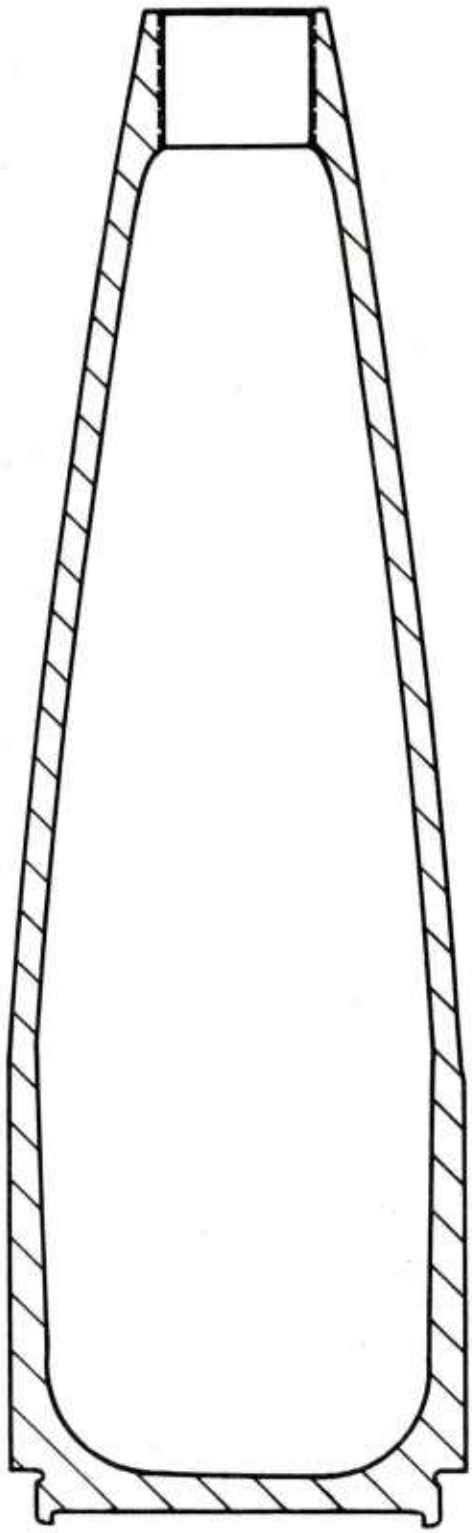

Fig. D-1 Detail print of circumferential flaw standard.

tion. An independent government agency (the local DISCO representative) was at the manufacturing facility to verify the dimensional qualifications of the parts produced.

Due to the high force applied to the projectile during inspection (6000 lbs distributed over the 20.75" length), it was deemed inappropriate to use epoxy to glue the standard projectiles back together. The standard flaw projectiles must be split in two in order to accurately cut the ID flaws specified in the specification drawings. Hence we devised a method of cutting the projectile off its base such that a) the required ID EDM notches could be cut and b) the parts could be rejoined by threading the two parts and screwing them together. This method yielded a very high strength projectile standard that was safe to test and produced "clean" ultrasonic signals. Both the longitudinal and circumferential standards were constructed in this manner. Both of these ultrasonic test standards were shipped to ARRADCOM for further evaluation by the EMAT system.

DISTRIBUTION LIST

Administrator
Defense Technical Information Center
ATTN: Accessions Divisions (2)
Cameron Station
Alexandria, VA 22314

Commander
U.S. Army Armament Research and
Development Command
ATTN: DRDAR-SC, COL Murray G. Swindler
DRDAR-SCP
DRDAR-SCM (10)
DRDAR-SCM-P (25)
DRDAR-TSS (5)
DRDAR-QA
Dover, NJ 07801

Director
Ballistics Research Laboratory
U.S. Army Armament Research and
Development Command
ATTN: DRDAR-TSB-S
Aberdeen Proving Ground, MD 21005

Commander
U.S. Army Materials and Mechanics
Research Center
ATTN: DRXMR, Dr. E. Wright
DRXMR-PT
Watertown, MA 02172

Director
U.S. Army Industrial Base
Engineering Activity (2)
ATTN: DRXIB-MT
Rock Island, IL 61201

Commander
U.S. Army Armament Research and
Development Command
Weapons Systems Concepts Team
ATTN: DRDAR-ACW
APG, Edgewood Area, MD 21010

Commander/Director
Chemical Systems Laboratory
U.S. Army Armament Research and
Development Command
ATTN: DRDAR-CLJ-L
APG, Edgewood Area, MD 21010

Chief
Benet Weapons Laboratory, LCWSL
U.S. Army Armament Research and
Development Command
ATTN: DRDAR-LCB-TL
Watervliet, NY 12189

Commander
U.S. Army Armament Materiel
Readiness Command
ATTN: DRSAR-LEP-L
Rock Island, IL 61299

Director
U.S. Army Materiel Systems
Analysis Activity
ATTN: DRXSY-MP
Aberdeen Proving Ground, MD 21005

Project Manager
Production Base Modernization
ATTN: DRCPM-PBM-MA
Dover, NJ 07801

Project Manager
Cannon Artillery Weapons Systems/
Semi-Active Laser Guided Projectiles
ATTN: DRCPM-CAWS
Dover, NJ 07801